UNIVERSIDADE ESTADUAL PAULISTA
Faculdade de Ciências e Tecnologia
Câmpus de Presidente Prudente

LUIZ HENRIQUE DA SILVA ROTTA

# Estimation of Submerged Aquatic Vegetation Height and Distribution in Nova Avanhandava Reservoir (São Paulo State, Brazil) Using Bio-Optical Modeling

Presidente Prudente

2015

UNIVERSIDADE ESTADUAL PAULISTA
Faculdade de Ciências e Tecnologia
Câmpus de Presidente Prudente

LUIZ HENRIQUE DA SILVA ROTTA

# Estimation of Submerged Aquatic Vegetation Height and Distribution in Nova Avanhandava Reservoir (São Paulo State, Brazil) Using Bio-Optical Modeling

Thesis for Doctoral Defense Presented to the Post Graduate Program in Cartographic Sciences, Faculty of Science and Technology – São Paulo State University.

Research Line: Cartography, GIS and Spatial Analysis.

Advisor: Prof. Dr. Nilton Nobuhiro Imai

Co-Advisor: Prof. Dr. Enner Herenio Alcantara

Presidente Prudente

2015

Rotta, Luiz Henrique da Silva.
R76e Estimation of Submerged Aquatic Vegetation Height and Distribution in Nova Avanhandava Reservoir (São Paulo State, Brazil) Using Bio-Optical Modeling / Luiz Henrique da Silva Rotta. - Presidente Prudente : [s.n], 2015
124 f. : il.

Orientador: Nilton Nobuhiro Imai
Coorientador: Enner Herenio de Alcântara
Tese (doutorado) - Universidade Estadual Paulista, Faculdade de Ciências e Tecnologia
Inclui bibliografia

1. Sensoriamento remoto. 2. Modelo bio-óptico. 3. Vegetação aquática submersa. 4. Cartografia. I. Rotta, Luiz Henrique da Silva Rotta. II. Nilton Nobuhiro, Imai. III. Alcântara, Enner Herenio de. Universidade Estadual Paulista. Faculdade de Ciências e Tecnologia. III. Título.

UNIVERSIDADE ESTADUAL PAULISTA
"JÚLIO DE MESQUITA FILHO"
Campus de Presidente Prudente

**BANCA EXAMINADORA**

Prof. Dr. NILTON NOBUHIRO IMAI
(Orientador)

Prof. Dr. ANTONIO MARIA GARCIA TOMMASELLI
(UNESP/FCT)

Profa. Dra. LIGIA FLAVIA ANTUNES BATISTA
(UTFPR)

Prof. Dr. DEEPAK RANJAN MISHRA
(University of Georgia)

Prof. Dr. ARCILAN TREVENZOLI ASSIREU
(UNIFEI)

LUIS HENRIQUE DA SILVA ROTTA

Presidente Prudente (SP), 11 de março de 2015.

Resultado: APROVADO

Faculdade de Ciências e Tecnologia
Seção Técnica de Pós-Graduação
Rua Roberto Simonsen, 305 CEP 19060-900 Presidente Prudente SP
Tel 18 3229-5318 fax 18 3223-4519 posgrad@fct.unesp.br

*A Deus.*

*À minha esposa, pela cumplicidade, apoio e amor.*

*Aos meus pais e família por todo carinho e suporte.*

*.*

# AGRADECIMENTOS

Quero expressar meus sinceros agradecimentos a todas as pessoas que contribuíram para a realização desta pesquisa, cada qual a seu modo. Agradeço em especial:

A Deus, em primeiro lugar, pelas graças concedidas.

À Simone, esposa dedicada e maravilhosa, pela amizade, carinho, conselhos, compreensão e todo o imenso amor proporcionado todos os dias, sem o qual seria impossível desenvolver esta pesquisa.

Aos meus pais, Luiz e Iza, por todo carinho e amor. Aos meus irmãos, Mone e João e também a toda família, tios, primos e sobrinhos sempre presentes.

À minha sogra e sogro, Lucy e Colemar, pelo acolhimento e carinho, e ao Lucas, irmão e amigo, sempre disposto a ajudar.

Ao meu orientador, Imai, professor e amigo, pela confiança, ensinamentos e liberdade no desenvolvimento da tese.

Ao Enner, não somente orientador, mas também um amigo, sempre disposto a conversar, ensinar e resolver os problemas que surgiram ao longo da pesquisa.

Ao Deepak Mishra, pela amizade, ensinamentos, e orientação durante o período do doutorado sanduíche realizado na "University of Georgia", fundamentais para os resultados obtidos. Ao departamento de geografia da UGA, pela recepção no meu doutorado em Athens – GA, Estados Unidos.

Aos professores do departamento de Cartografia, por compartilharem seus conhecimentos e experiências.

Aos membros da banca de qualificação e de defesa, que contribuíram com sugestões expressivas.

Aos amigos que me ajudaram muito nos trabalhos de campo, essencial para o andamento da pesquisa, Ricardo, Ulisses, Rejane, Lino, Renato e em especial à Fer e Thanan. Nesse sentido agradeço ao Prof. Cláudio do INPE por ter cedido equipamentos necessários para o levantamento de dados em campo.

Aos amigos do "SRGeoAMA", pelas discussões científicas e momentos de descontração e aos amigos do convívio da sala da pós, pelas amizades, festas, cafezinho e outros momentos.

Ao Conselho Nacional de Desenvolvimento Científico (CNPq) pela bolsa cedida e pelos recursos dos projetos de pesquisa Universal: CNPq 472131/2012-5 e CNPq 482605/2013-8, assim como dos projetos FAPESP: 2013/09045-7 e 2012/19821-1. Agradeço também ao CNPq pela bolsa sanduíche, por meio do projeto CNPq 400881/2013-6.

À UNESP e ao Programa de Pós-Graduação em Ciências Cartográficas, pela estrutura e auxílio nos trabalhos de campo e participação em eventos científicos.

Agradeço a todos que não mencionei e que contribuíram direta ou indiretamente para o desenvolvimento do trabalho.

*“A tarefa não é tanto ver aquilo que ninguém viu, mas pensar o que ninguém ainda pensou sobre aquilo que todo mundo vê.”*

*(Arthur Schopenhauer)*

# RESUMO

Modelos semi-analíticos vêm sendo desenvolvidos para remover a influência da coluna da água e, com isso, recuperar a resposta do substrato em corpos águas, com o intuito de estudar alvos submersos. Porém, a maioria desses modelos foram elaborados para águas oceânicas e costeiras, ou seja, ainda são limitados os estudos sobre a recuperação da resposta do substrato a partir de sensoriamento remoto em ambientes aquáticos continentais devido à complexidade desses ambientes, pois apresentam altas concentrações de constituintes suspensos e dissolvidos da água, o que dificulta a detecção do sinal do substrato. Os objetivos do trabalho foram: avaliar a disponibilidade de radiação subaquática na coluna de água e o total de sólidos suspensos (TSS) no Reservatório de Nova Avanhandava, para analisar sua influência no desenvolvimento da VAS (Vegetação Aquática Submersa); recuperar a resposta do substrato e gerar modelos bio-ópticos para estimar a altura e posição da vegetação aquática submersa no reservatório de Nova Avanhandava; e finalmente utilizar e avaliar o desempenho dos modelos bio-ópticos por meio de imagem multiespectral (SPOT-6). Dados hiperespectrais foram coletados com o radiômetro RAMSES – TriOS. Constatou-se que os estudos sobre disponibilidade de radiação subaquática medida por meio da atenuação vertical da irradiância descendente na coluna de água pode auxiliar na compreensão do comportamento da VAS em reservatórios tropicais e, portanto, contribuir para a sua gestão. A imagem de satélite, adquirida em 9 de julho de 2013, foi corrigida atmosfericamente por método empírico. Os dados de profundidade e altura da VAS foram coletados por ecobatímetro. Com isso, foi possível recuperar a reflectância do substrato por meio de modelos disponíveis na literatura. Posteriormente, modelos para estimar a altura da VAS foram calibrados por meio do índice GRVI (*Green Red Vegetation Index*) e *Slope* com as bandas da região do verde e do vermelho. Os modelos com melhores ajustes foram aplicados na imagem multiespectral para estimar a altura da VAS em toda área de estudo e, assim, avaliar seu desempenho. O uso do GRVI, na calibração do modelo para estimar a altura da VAS, se mostrou mais adequado ($R^2$ = 0.74 e RMSE = 0.40 m) quando utilizados dados de campo. Porém, ao se utilizar dados da imagem, a calibração dos modelos foi mais pertinente com o uso do Slope entre as bandas do verde e vermelho, com $R^2$ entre 0.47 e 0.63 e RMSE entre 0.54

e 0.66. Os modelos calibrados foram aplicados na imagem SPOT-6 e obteve-se uma exatidão global de 53% e índice kappa de 0.34 para o modelo baseado no GRVI. O modelo utilizado para estimar a presença e ausência de VAS foi altamente eficaz, com uma exatidão global de 90% e kappa de 0.7. Assim, pela complexidade em se estudar alvos submersos em água interiores, os resultados trouxeram contribuições relevantes. Finalmente, observou-se que estudos sobre a disponibilidade de radiação subaquática por meio da atenuação vertical da radiação na coluna de água pode ajudar a compreender o comportamento da VAS em reservatórios tropicais e, portanto, contribuir para sua gestão.

**Palavras-Chave**: Sensoriamento remoto, modelo bio-óptico, vegetação aquática submersa, reflectância do substrato, coeficiente de atenuação difusa, *Egeria spp*.

## ABSTRACT

Semi-analytical models have been developed to remove the water column influence and then retrieve the bottom reflectance in water bodies in order to study submerged targets. However, the majority of these models were elaborated for oceanic and coastal waters, in other words, there are still limited studies about the retrieval of the bottom response from remote sensing in continental aquatic environments. The reason for that is the complexity of those environments as they present high concentrations of dissolved and suspended constituents, which make it difficult to detect the bottom signal. The objectives of this thesis were: to assess the availability of sub-aquatic radiation in the water column and the total suspended solids concentration (TSS) in the Nova Avanhandava reservoir in order to analyze their influence on the SAV (Submerged Aquatic Vegetation) development; to recover the bottom albedo and generate bio-optical models to estimate the aquatic submerged vegetation height and position in the Nova Avanhandava reservoir; and finally, to use and assess the bio-optical models performance by using multi-spectral imagery (SPOT-6). Hyperspectral data were collected by using the radiometer RAMSES – TriOS. It was found that studies on subaquatic radiation availability measured by the vertical attenuation of downwelling irradiance in the water column can aid in understanding SAV behaviour in tropical reservoirs and, therefore, contribute to its management. SPOT-6 image, acquired on July the 9th of 2013, was atmospherically corrected by the empirical line method. The SAV depth and height data were collected by using the echosounder. Thus, it was possible to recover the bottom reflectance by using the models available on literature. After, models to estimate the SAV height were calibrated through GRVI index and Slope with the green and red regions of the electromagnetic spectrum. The models with better adjustments were applied on the multispectral image to estimate the SAV height all along the study area and their performance was assessed. The GRVI usage, when calibrating the model to estimate the SAV height, presented better results ($R^2$ = 0.74 and RMSE = 0.40 m) when used on the field data. However, when using the image data, the models calibration was more relevant with the usage of Slope between the green and red bands, presenting a $R^2$ between 0.47 and 0.63 and a RMSE between 0.54 and 0.66. The calibrated models were used on the SPOT-6 image to obtain the SAV height map. The model based on the GRVI presented a global accuracy of 53% and a kappa index of 0.34. The model calibrated to estimate the occurrence and absence of SAV was highly effective, presenting a global accuracy of 90% and a kappa of 0.7. Thus, considering the complexity involved in studying submerged targets into freshwater, the results made relevant contributions. Finally, it was noted that studies about the sub-aquatic radiation availability through vertical attenuation of the water column radiation can help to understand the SAV behavior in tropical reservoirs and therefore, can be used for their management.

**Keywords**: Remote sensing, bio-optical model, submerged aquatic vegetation (SAV), bottom reflectance, diffuse attenuation coefficient, *Egeria spp*.

## LIST OF FIGURES

## LIST OF TABLES

## LIST OF ABBREVIATIONS AND ACRONYMS

$\{D_d\}$ – Vertically averaged downwelling distribution function

*a* – Absorption coefficient

AC-S – In-situ spectrophotometer for absorption and attenuation coefficients

AOP – Apparent Optical Properties

ASCII - American Standard Code for Information Interchange

$b_b$ – Backscattering coefficient

$B_{de}$ – Total dry weight of epiphytic materials

$B_e$ – Epiphyte biomass

*C*: pixel-independent constant

DIE03 – Model to retrieve the bottom as described in Dierssen et al. (2003)

DN – Digital Number

$D_u^B$ – The path-elongation factors for photons scattered by the bottom

$D_u^C$ – The path-elongation factors for photons scattered by the water column

$E_d$ – Downwelling irradiance

$E_d\,PAR$ – Integration of the $E_d$ between 400 nm and 700 nm

$E_d\,PAR$ ($Z_{EZ}$) – Downwelling irradiance of PAR at the euphotic zone depth limit $Z_{EZ}$ – Euphotic zone depth limit

$E_s$ – Incident surface irradiance

$E_u/E_d$ – Irradiance reflectance

$F_i$ – Spectral immersion coefficient

FLAASH – Fast Line-of-sight Atmospheric Analysis of Spectral Hypercubes

FSS – Fixed Suspended Solids

GPS - Global Positioning System

GRVI – Green-Red Vegetation Index

H – Depth

HydroScat – Backscattering Sensor

INMET (Instituto Nacional de Meteorologia) – National Institute of Meteorology

IOP – Inherent Optical Properties

*K* – *A*ttenuation coefficient

$K_d$ – Vertical diffuse attenuation coefficient of downwelling irradiance ($E_d$)

$K_d^{\,P}$ – Diffuse attenuation coefficient as in Palandro et al. (2008)

$K_e$ – Biomass-specific epiphytic light attenuation coefficient

$K_{Lu}$ – Vertical diffuse attenuation coefficient of upwelling radiance ($L_u$)

$K_u^B$ – Vertical average diffuse coefficient of attenuation for upwelling irradiance of the bottom

$K_u^C$ – Vertical average diffuse coefficient of attenuation for upwelling irradiance of the water column scattering

LEGAL (Linguagem Espacial para Geoprocessamento Algébrico) – Spacial Language for Algebric Geoprocessing

$L_p$ – Radiance from reference panel

$L_u$ – Upwelling radiance

MODTRAN – MODerate spectral resolution atmospheric TRANsmittance algorithm and computer model

$n$ – Refractive index of water relative to air (1.33)

NDVI – Normalized Difference Vegetation Index

NF – Normalization factor

OLI - Operational Land Imager

PAL08 – Model to retrieve the bottom as described in Palandro et al. (2008)

PAR – Photosynthetically Active Radiation

PLL – Percent Light at the Leaf

PLW – Percent Light through the Water

$Q$ – *R*atio of upwelling irradiance and upwelling radiance ($E_u/L_u$)

$Q_b$ – *R*atio of upwelling irradiance and upwelling radiance ($E_u/L_u$)

$R^2$ – coefficient of determination

$R^b$ – Irradiance reflectance of the bottom

$R^{dp}$ – Irradiance reflectance of deep water

$R_{rs}$ – *A*bove-water remote sensing reflectance

$r_{rs}$ – Remote sensing reflectance just below the water surface

$R_{rs}^b$ – Remote sensing reflectance above surface from the bottom

$r_{rs}^b$ – Remote sensing reflectance just below the water surface from the bottom

$R_{rs}^c$ – Remote sensing reflectance above surface from water column

$r_{rs}^c$ – Remote sensing reflectance just below the water surface from water column

$r_{rs}^{dp}$ – Remote sensing reflectance just below the water surface for optically deep water

SAV – Submerged Aquatic Vegetation

SPOT (*Satellite Pour l'Observation de la Terre)* – Satellite for observation of Earth

SPRING (Sistema de Processamento de Informações Geográficas) – Geographic Information Processing System

$S_{us}$ – Subsurface upwelling signal

$S_{us}^{B}$ – Upwelling signal above the bottom.

$S_{us}^{dp}$ – Signal in deep water

*t* – *T*ransmittance at air-water interface (0.98)

TSS – Total Suspended Solids

UGRHI (Unidades de Gerenciamento de Recursos Hídricos) – Water Resources Management Unit

VSS – Volatile Suspended Solids

Z – Depth

$\theta_{\vartheta}$ – Subsurface sensor viewing angle from nadir

$\theta_{\omega}$ – Subsurface solar zenith angle

$\rho$ – Bottom albedo

$\rho_{p}$ – Stands for the reflectance of reference panel

CONTENTS

# 1. INTRODUCTION

Nearly 90% of the area flooded by dams in Brazil is a consequence of the hydrologic installations established in the last 40 years in the South Western, Centre Western and Southern regions (ARAÚJO-LIMA et al., 1995). Several dams were constructed throughout Brazil for electrical power generation following its industrial and socio-economic development, which yielded many artificial lake ecosystems (ESTEVES, 2011). Reservoirs and natural lakes differ in significant ways; however, there are many functional similarities between these ecosystems (WETZEL, 2001). The processes and functions that are common to reservoirs and lakes include internal mixing, gas exchange across air-water interface, redox reactions, nutrient uptake, predator-prey interactions, and primary production. The main primary producers in reservoirs are the same as in rivers and lakes and primarily include phytoplankton, photoautotrophic bacteria, periphytic algae, and macrophytes (both rooted, floating, emerged and submerged) (TUNDISI and TUNDISI, 2008).

Macrophytes are important in the biodiversity-support functioning of freshwater systems: it is vital for many animal communities (such as aquatic invertebrates, fish and aquatic birds), change the water and sediment physic-chemistry, influence the nutrient cycling, can be food for invertebrates and vertebrates, and change the spatial structure of the waterscape by increasing habitat complexity (THOMAZ et al., 2008). Submerged macrophytes occupy key interfaces in aquatic ecosystems, so they have major effects on productivity and biogeochemical cycles in fresh water (CARPENDER and LODGE, 1986). *Egeria densa* and *Egeria najas* are among the primary species of submerged macrophytes found in Brazilian reservoirs (THOMAZ and BINI, 1998; CAVENAGHI et al., 2003; MARCONDES et al., 2003; BINI and THOMAZ, 2005).

Several factors impact primary productivity of the aquatic macrophytes, such as temperature, radiation availability, stream velocity, water level variation, nutrient concentration, competition, and inorganic carbon (CAFFREY et al., 2007; CAMARGO et al., 2003; BIUDES and CAMARGO, 2008). However, radiation availability is the primary limiting factor for submerged aquatic macrophytes (SCHWARZ et al., 2002; HAVENS, 2003; TAVECHIO and THOMAZ, 2003; THOMAZ, 2006; RODRIGUES and THOMAZ, 2010; KIRK, 2011). When traversing the water column, the radiation changes primarily due to the concentration of materials both in solution and suspension (ESTEVES, 2011). Most of these materials in the water column absorb and scatter radiation and are referred to as “optically active constituents”. Studies on five Tietê River reservoirs in Brazil showed that suspended solids have a great effect on light transmission through the water column and, thus, determine the development of submerged aquatic vegetation (SAV) (CAVENAGHI et al., 2003). Therefore, it is important assess the spatial distribution of suspended solid concentration and, after that, its influence on radiation availability and SAV productivity.

It is known the importance of radiation availability for growth and maintenance of submerged aquatic vegetation, but studies are needed to explain in detail the relationship between SAV and radiation. Thus, the use of optical parameters in this analysis may contribute significantly to understand better the SAV behavior in Brazilian reservoirs. Further, it is necessary to know the spatial distribution of submerged macrophyte to aid in water body management. Thus, different techniques to map this vegetation have been used (WATANABE et al., 2013; VAHTMÄE and KUTSER, 2013). In addition of SAV mapping, the photosynthetically active radiation behaviour along the water column should be studied to assess subaquatic radiation availability.

The constituents dissolved and suspended in the water column, named “optically active”, cause the radiation, when penetrating into the water, to be absorbed and scattered. According to Kirk (2011), the absorption and scattering properties of light in aquatic environment, in any wave length, are specified in terms of absorption coefficient, scattering coefficient and volume scattering function. They are the Inherent Optical Properties - IOP, for and their magnitude depends only on the aquatic environment and not on the geometrical structure of the light field.

Empirical models are widely used in the inference of optically active components on water bodies through remote sensing. Rotta et al. (2009) used multispectral images and in situ measurements to generate a regression model to infer the spatial distribution of suspended solids in the floodplain of upper Paraná River. Ferreira et al. (2009), through empirically generated model, performed the spatial inference of pigments in suspension through multispectral images. Rudorff et al. (2007) compared the performance of empirical algorithms to estimate the concentration of chlorophyll-*a* by remote sensing data and in situ measurements.

Analytical or semi-analytical models incorporate, besides the Inherent Optical Properties, the Apparent Optical Properties. Apparent Optical Properties (AOP) are dependent on both the environment and the directional structure of the ambient light field. The semi-analytical model can provide response of the optically active components and the bottom. Also, it is possible to detect the submersed macrophytes in water bodies of water, as this vegetation has been causing many problems in reservoirs.

In the reservoirs built until nowadays, either for storing water or for hydropower production, water quality is already sufficiently compromised since the filling, i.e. the eutrophication level is sufficient to support significant growth of submergsed macrophytes, floating and marginal (PITELLI, 2006).

Marcondes et al. (2003) in their study, showed that in the rainy period, the increase of the reservoir flow causes the fragmentation of submerged aquatic plants and leads this vegetation to be dragged by the reservoir toward the hydroelectric plant, hampering navigation, fishing, capture and leisure. Those plants generally accumulate in the guardrails of the water intake of generating units causing clogging of the grids and, consequently, decrease the uptake of water and this causes turbines' power oscillation. The greater pressure on the grids may inflict deformation or breakage of them, making it necessary to interrupt the operation of the generating unit to replace the damaged grids.

In fact, the remote sensing studies developed to estimate optically active components in Brazil still focus on empirical approach. However, the parameterization of semi-analytical models and their adaptation in albedo estimation models in optically shallow water reservoirs of São Paulo power plants would be a valuable contribution, allowing the mapping of SAV.

## 1.1 Motivation

The importance of radiation availability is known for growth and maintenance of submerged aquatic vegetation, but studies are needed to explain in detail the relationship between SAV and radiation. Thus, the use of optical parameters in this analysis may contribute significantly to understand better the SAV behavior in Brazilian reservoirs. Further, it is necessary to know the spatial distribution of submerged macrophyte to aid in water body management. Different techniques to detect this vegetation have been used (WATANABE et al., 2013; VAHTMÄE and KUTSER, 2013). In addition of SAV mapping, the photosynthetically active radiation behavior along the water column must be studied to assess subaquatic radiation availability.

The calculation of the spatial distribution of SAV is a costly task currently, when performed with data from field surveys. The procedures involved in such calculation require long time and therefore the mapping of SAV is impracticable, especially in large reservoirs. However, this alternative is very common, because it allows the researcher to create the inventory and also identify the vegetation (POMPÊO and MOSCHINI-CARLOS, 2003). Another option is based on calculations with sonars that produce bathymetry, density and height data of the SAV (VALLEY and DRAKE, 2005). However, those hydroacoustic techniques demand long time if conducted with few boats.

An alternative for detecting SAV is the use of remote sensing data. According Dekker et al. (2001), if the water column is sufficiently transparent and the bottom is at a depth where enough quantity reaches the bottom and it is reflected back out of the water body, so, it is possible to produce maps of macrophytes, macro-algae, shoals, coral reefs etc. (DEKKER et al., 2001).The spectral response to of the bottom in optically shallow water at the ocean shore was estimated by Lee et al. (2007). This approach allows the mapping of corals based on hyperspectral images. Other studies show that inverse models based on the Radiative Transfer Theory in water bodies can be adapted to estimate the response of the bottom or even to estimate the height of the water column (GIARDINO et al., 2012; BRANDO et al. 2009; ALBERT and MOBLEY, 2003; DEKKER et al., 2001; LEE et al., 1998, 1999 and 2001).

Multispectral images have been used to study benthic habitats. Mishra et al. (2006) used Quickbird multispectral data to benthic habitat mapping in tropical marine environments. Mumby et al. (2004) indicated the possibility to study reef geomorphology, location of shallow reefal areas, reef community (<5 classes), bathymetry and coastal land use by Landsat and SPOT images.

There are some methods to retrieve the bottom response from reflectance (e.g., LEE et al., 1994; MARITORENA et al., 1994; LEE et al., 1999; LEE AND CARDER, 2002) which presented suitable results and could be tested to the Nova Avanhandava Reservoir. Palandro et al. (2008) used $K_d$ to remove water-column attenuation effect from $R_{rs}$, obtaining the remote sensing reflectance of the bottom ($R_{rs}^b$). Dierssen et al. (2003) presented a method derived of Beer's Law to retrieve the irradiance reflectance ($E_u/E_d$) of the bottom ($R^b$). After retrieving the response of the bottom it is possible to extract information such as localization and height of the SAV in the studied reservoir.

### 1.2. Hypothesis

This study is based on the hypothesis that from multispectral data and based on the radiative transference theory in the water column it is possible to retrieve the bottom reflectance by remote sensing, to identify and estimate the height of the submerged aquatic vegetation present in the reservoir.

### 1.3 Objectives

The objectives of the study are:

- To assess the subaquatic radiation availability in the water column and the total suspended solid (TSS) concentration in the Nova Avanhandava Reservoir and analyze its influence on SAV initiation and development;
- To retrieve the bottom response and generate bio-optical models to estimate the height and the position of submerged aquatic vegetation in the Nova Avanhandava reservoir;
- To use and evaluate the performance of bio-optical models of the generation of maps of the distribution and SAV height through multispectral image – SPOT-6.

### 1.4 Structure of thesis

This thesis consists of six chapters and three appendices. Chapter 1 holds the introduction and Chapter 2 the review on the relevant issues of the study. The characterization of the study area is done on Chapter 3. The Chapter 4 brings materials and methods and Chapter 5 the results and discussion. Finally, the conclusions are presented on Chapter 6.

# 2. REVIEW

## 2.1 Aquatic vegetation

Aquatic plants can be grouped into three main assemblages: Emergent – rooted at the bottom and projecting out of the water for part of their length; Floating – which wholly or in part float on the water surface; and Submerged – they are continuously submerged (WETCH, 1952). They also can be divided in: rooted submerged – plants that grow completely submerged and are rooted into the sediment; free-floating – plants that float on or under the water surface; emergent – plants rooted in the sediment with foliage extending into the air; and floating-leaved – plants rooted in the sediment with leaves floating on the water surface. Epiphytes (plants growing over other aquatic macrophytes) and amphibious (plants that live most of their life in saturated soils, but not necessarily in water) are additional life forms that have been proposed (THOMAZ et al., 2008).

In Brazil, the submerged aquatic vegetation (SAV) with the highest expression in power generation reservoirs and rural dams are *Egeria densa* and *Egeria najas*. Among the damage caused by excessive growth of this plant is the favoring for disease vectors breeding. The marketing of *E. densa* e *E. najas* as ornamental plant for aquariums made possible its spread to various parts of the world (MARTINS et al., 2003).

Thomaz (2006) found that in a chain of the Tietê River reservoirs, the highest occurrences of submerged plants were found in reservoir downstream of Três Irmãos - the last reservoir of the series. But the predominance of floating macrophytes occurred in Barra Bonita, the first of the series in middle Tietê River. Considering the reservoirs individually (research mainly developed in Itaipu and Rosana reservoirs in the Paraná and Paranapanema rivers, respectively) some factors that explained the distribution of aquatic vegetation were level of water, nutrients, underwater radiation, fetch (way to assess the effects of wind ) and slope.

Furthermore, Thomaz (2006) found that underwater radiation has been an extremely important variable to explain the submerged plants distribution patterns within the same reservoir. Study in Rosana Reservoir showed that the different distribution of *E. densa* and *E. najas* can be associated with that factor, since the former species predominates in the lake region, while the latter, in the intermediate region. This trend was also observed in the Itaipu reservoir, where the probability of *E. najas* is higher in places with less water transparency in comparison to *E. densa*.

## 2.2 The relationship between SAV and radiation availability

The hyperspectral downwelling irradiance data can be used to compute the vertical attenuation coefficient ($K_d$) and euphotic zone depth. These parameters can analyze the influence of radiation availability on SAV incidence and development. In addition, two optical parameters which act as proxy to radiation availability in SAV habitats can be computed: (1) Percent Light through the Water (PLW) and (2) Percent Light at the Leaf (PLL). PLW is a measure of the light transmitted through the water column to the depth of SAV growth, and PLL considers the additional light attenuation by epiphytic materials (KEMP et al., 2004).

PLW is calculated as an exponential relationship to depth of SAV growth (*Z*) and attenuation coefficient ($K_d$) (Equation (1)). PLL (Equation (2)) is calculated using PLW and variables derived from numerical and empirical relationships, *Be*, epiphyte biomass and *Ke*, biomass-specific epiphytic light attenuation coefficient (KEMP et al. 2000).

$$PLW = 100 \cdot e^{-Kd \cdot Z} \tag{1}$$

$$PLL = PLW \cdot e^{-Ke \cdot Be} \tag{2}$$

$$K_e = 0.07 + 0.32 \cdot (B_e / B_{de})^{-0.88} \tag{3}$$

where, $B_{de}$ is the total dry weight of epiphytic materials. A significant relationship ($r^2$ = 0.85) was observed among $B_{de}$, $B_e$ and TSS in a set of studies in experimental ponds (TWILLEY et al., 1985):

$$B_{de} = 0.107 \cdot TSS + 0.832 \cdot B_e \tag{4}$$

## 2.3 Optical properties of water

The water color is a complex optical characteristic and it is influenced by the absorption processes, scattering and emission by the water column and reflectance by the bottom (DEKKER et al., 2001).

According to Kirk (2011), radiation, when penetrating into the water, may be absorbed or scattered. The absorption or scattering properties of light in the aquatic environment, at any wave length, are specified in terms of absorption coefficient, spread coefficient and volumetric spread function. They are the Inherent Optical Properties – IOPs, for their magnitude depends solely on the aquatic environment and not on the geometrical structure of the light field. The two fundamental Inherent Optical Properties - coefficient of absorption and scattering - can be defined in terms of the behavior of a parallel beam of light incident on a thin layer of the medium.

Apparent Optical Properties – AOP, are dependent both on the medium and on the directional structure of the ambient light field. An ideal AOP changes slightly with external environmental changes, but, it modifies a water body to another sufficiently, which makes it useful in the characterization of different optical properties of two water bodies. Unlike the IOP, the AOP cannot be measured in water samples as they depend on the distribution of environmental radiance found in the water body (MOBLEY, 1994).

For the mapping of the bottom, the relationship between the optical properties and the concentration of the particles of the water column should be known as well as the optical properties of the bottom. If the inherent optical properties of the optically active components are sufficiently well characterized, their contributions for the color of the water column can be discriminated and their content quantified. Due to the fact that the radiation reflected by the water depends on the quality and the specific optical properties of one or more constituents of the water, its color carries spectral information on the concentration of some parameters of water quality and possibly of the bottom (DEKKER et al., 2001).

For the retrieval of different constituents of the water and the bottom cover, using the signaling of hyperspectral remote sensing, there is a group of inversion methods available. It ranges from the frequently used, although less precise regression methods, up to the inversion models based on physical principles or inversion methods. If the water column is sufficiently transparent and the bottom is at a depth where enough quantity reaches the bottom and it is reflected back out of the water body, so, it is possible to produce maps of macrophytes, macro-algae, shoals, coral reefs etc. (DEKKER et al., 2001).

### 2.3.1 Diffuse attenuation coefficient

Cloud cover variability can cause variations in incident surface irradiance, $E_s$ *(z, λ)*. So, it is strongly recommended that all scans be normalized to a specific scan (Mueller, 2003). The normalization factor $NF\ (z, \lambda)$ for each scan can be calculated as:

$$\boldsymbol{NF\ (z,\lambda)} = \frac{\boldsymbol{E_s[t(0^-),\lambda]}}{\boldsymbol{E_s[t(z),\lambda]}} \tag{5}$$

where,

$E_s[t(0^-),\lambda]$: is the downwelling irradiance measured at the first scan at time $t(0^-)$ on the boat.

$E_s[t(z),\lambda]$: is the downwelling irradiance measured at time t(z) on the boat.

A normalization factor greater than 1 indicate lower irradiance, as clouds shadow, and values less than 1 indicate brighter conditions (MISHRA et al., 2005). To normalize the spectral data and eliminate the noise due to change in illumination, the Equation (6) can be used for the downwelling irradiance and Equation (7) for upwelling radiance.

$$E'_d(z,\lambda) = E_d(z,\lambda)NF(z,\lambda) \tag{6}$$

$$L'_u(z,\lambda) = L_u(z,\lambda)NF(z,\lambda) \tag{7}$$

Diffuse attenuation coefficient is the parameter that controls the propagation of light through water. Characterizing the water column, $K_d$ is important because it can quantify the presence of light in different depths and determine the euphotic zone (MISHRA et al., 2005). Vertical diffuse attenuation coefficient ($K_d$) can be defined as the exponential decrease in ambient irradiance as a function of depth (KIRK, 2011).

Radiances and Irradiances decrease exponentially with depth, therefore the downwelling irradiance $E_d$ (z, λ) is (MOBLEY, 1994):

$$E_d(z;\lambda) = E_d(0^-;\lambda)e^{-K_d(z;\lambda)z} \tag{8}$$

Isolating the variable $K_d$ yields the following:

$$K_d = \frac{\ln E_d(0) - \ln E_d(z)}{Z} \tag{9}$$

The same way of Equation (8), it is possible to calculate the attenuation coefficient of upwelling radiance $L_u$ (z; λ) (MUELLER et al., 2003):

$$L_u(z;\lambda) = L_u(0^-;\lambda)e^{-K_{Lu}(z;\lambda)z} \tag{10}$$

The $K_d$ also can be calculated using the inherent optical properties of the water. The $K_d$ can be simply expressed as function of the absorption (*a*) and backscattering coefficients ($b_b$) (SATHYENDRANATH et al., 1989; MOBLEY, 1994; LEE et al., 2005):

$$K_d = \frac{a+b_b}{\cos(\theta_w)} \tag{11}$$

where,

$\theta_w$ is the solar zenith angle just below the surface.

Palandro et al. (2008) calculated the $K_d$ of a water body using only the spectral images from satellite and the depth. This diffusion attenuation coefficient will be described as $K_d{}^P$.

$$\boldsymbol{R_{rs}(Z) = C * e^{-2*K_d{}^P*Z}} \tag{12}$$

where,

$K_d{}^P$: diffuse attenuation coefficient in Palandro's methodology;

$R_{rs}(z)$: above-water remote sensing reflectance for a pixel with bottom depth Z;
$C$: pixel-independent constant.

Photosynthetically Active Radiation (PAR) comprehends the spectrum range of solar radiation from 400 nm to 700 nm. So, The $E_d$ *PAR* can be calculated integrating the $E_d$ between 400 nm and 700 nm. Based on Equation (8), $E_d$ *PAR* can be obtained:

$$E_d PAR(z) = E_d PAR(0^-) e^{-K_d PAR(z) Z} \tag{13}$$

The illuminated portion of the water column, the euphotic zone, can vary from a few centimeters to tens of meters. Euphotic zone is the region in a body of water with sufficient PAR to sustain photosynthesis (KIRK, 2011).The euphotic zone lower limit is typically the depth where the photosynthetically active radiation corresponds to 1% of the subsurface radiation ($E_d PAR(0^-)$) (ESTEVES, 2011) as indicated below:

$$E_d PAR(Z_{EZ}) = 0.01 E_d PAR(0^-) \tag{14}$$

where,
$E_d PAR(Z_{EZ})$ is the downwelling irradiance of PAR at the euphotic zone depth limit ($Z_{EZ}$).

Equations (13) and (14) yield the following:

$$0.01 E_d PAR(0^-) = E_d PAR(0^-)^{-K_d PAR(Z_{EZ}).Z_{EZ}} \tag{15}$$

where,
$K_d$ *PAR* is the downwelling diffuse attenuation coefficient of PAR light in the water column.

Solving Equation (15) yields the following:

$$K_d (PAR) \cdot Z_{EZ} = 4.6\,. \tag{16}$$

## 2.4 Remote sensing reflectance

Dall'Olmo and Gitelson (2005) and Gitelson et al. (2008) showed a suitable approach to calculate the remote sensing reflectance above-water ($R_{rs}$):

$$R_{rs}(\lambda) = \frac{L_u(\lambda)}{E_d(\lambda)}\frac{t}{n^2}F_i \tag{17}$$

where,
$L_u(\lambda)$: is the upwelling radiance at nadir just below-surface.
$E_d(\lambda)$: is the downwelling irradiance.
$t$: is the transmittance at air-water interface (0.98).
$n$: is the refractive index of water relative to air (1.33).
$F_i$: is the spectral immersion coefficient

### 2.4.1 Retrieving bottom reflectance

The water color can be used to determine quantitatively the water constituent concentration and the bottom coverage. To accomplish that, it is necessary to know the specific optical properties of the water constituents and of the bottom, and to model the radiative transference through the water and the atmosphere as being a function of these constituents, comparing the signal modeled with the measured signal (DEKKER et al. ,2001).

For Kirk (2011), after setting the properties of the light field and the optical properties of the environment, it is necessary to check if it is possible to reach a relation between them, using mainly theoretical foundations.

The subsurface upwelling signal ($S_{US}$) can be approximated as being the sum of the water and the bottom contributions (LEE et al., 1998):

$$S_{US} \approx {S_{US}}^{dp}[1 - \exp(-2KH)] + {S_{US}}^{B}\exp(-2KH) \tag{18}$$

Where $S_{US}$ can mean the subsurface upwelling radiance, subsurface radiant reflectance (or subsurface irradiance ratio) or remote sensing reflectance of subsurface. $S_{US}{}^{dp}$ is the signal in deep water and the $S_{US}{}^{B}$ is the upwelling signal above the bottom. *H* is the depth and *K* is the attenuation coefficient.

A more general equation for the remote sensing reflectance ($R_{rs}$), defined by the ratio between the upwelling radiance and the downwelling irradiance, is (Lee et al., 1998):

$$R_{rs} \approx r_{rs}{}^{dp}\{1 - A_0 \exp[-(K_d + K_u{}^{C})\, H\} + A_1\rho \times \exp[-\left(K_d + K_u{}^{B}\right)H] \tag{19}$$

Where $r_{rs}{}^{dp}$ is the remote sensing reflectance for optically deep waters. $K_d$ is the vertical average diffuse coefficient of attenuation for downwelling irradiance, $K_u{}^{C}$ is the vertical average diffuse coefficient of attenuation for upwelling irradiance of the water column scattering and $K_u{}^{B}$ is the vertical average diffuse coefficient of attenuation for upwelling irradiance of the bottom. $\rho$ is the bottom irradiant reflectance assumed to be a Lambertian reflector.

Many models are able to retrieve the bottom response by using the radiative transference theory in the water-column. The reflectance measured on aquatic system can the defined as the sum of the reflectance from the column and the reflectance from the bottom (MARITORENA et al., 1994; LEE et al., 1998; LEE et al., 1999; LEE and CARDER, 2002). Therefore, the bottom reflectance can be obtained by the calculation of the reflectance from the water column.

$$r_{rs} = r_{rs}{}^{c} + r_{rs}{}^{b} \tag{20}$$

where,
$r_{rs}$: remote sensing reflectance just below the water surface;
$r_{rs}{}^{c}$: remote sensing reflectance from water column;
$r_{rs}{}^{b}$: remote sensing reflectance from the bottom.

According Lee et al. (1994), the remote sensing reflectance above surface from water column, $R_{rs}{}^{c}$ can be calculated as:

$$R_{rs}{}^{c} \approx \frac{0.176}{a}\frac{b_b}{Q}\left[1 - exp[-3\{D_d\}kH]\right] \tag{21}$$

$$k \equiv a + b_b \tag{22}$$

where,

$a$: absorption coefficient;

$b_b$: backscattering coefficient;

$Q$: ratio of upwelling irradiance and upwelling radiance;

{$D_d$}: vertically averaged downwelling distribution function;

H: depth.

Maritorena et al. (1994) calculated the irradiance reflectance from the bottom ($R^b$) using irradiance reflectance ($E_u/E_d$) of deep water ($R^{dp}$) and bottom albedo ($A$), besides $K_d$ and depth.

$$R^b = R^{dp} + (A - R^{dp})exp(-2K_d H) \tag{23}$$

The Equation (23) shows the expression for remote sensing reflectance ($r_{rs}$) in terms of remote sensing reflectance from the column ($r_{rs}^{c}$) and the remote sensing reflectance from the bottom ($r_{rs}^{b}$) (LEE et al. (1999) and LEE and CARDER (2002)

$$r_{rs} \approx {r_{rs}}^{c} + {r_{rs}}^{b} \approx {r_{rs}}^{dp}\left(1 - exp\left\{-\left[\frac{1}{\cos(\theta_\omega)} + \frac{{D_u}^{c}}{\cos(\theta_\vartheta)}\right]kH\right\}\right) + \frac{1}{\pi}\rho\, exp\left\{-\left[\frac{1}{\cos(\theta_\omega)} + \frac{{D_u}^{b}}{\cos(\theta_\vartheta)}\right]kH\right\} \tag{24}$$

where,

$r_{rs}^{dp}$: remote-sensing reflectance of optically deep waters;

$\theta_\omega$: subsurface solar zenith angle;

$\theta_\vartheta$: subsurface sensor viewing angle from nadir;

$\rho$: bottom albedo;

$D_u^C$: the path-elongation factors for photons scattered by the water column

$D_u^B$: the path-elongation factors for photons scattered by the bottom.

Palandro et al. (2008) used $K_d$ to remove water-column attenuation effect from $R_{rs,}$ thus obtaining the remote sensing reflectance of the bottom ($R_{rs}^{b}$).

$$R_{rs}{}^{b} = \frac{R_{rs}}{0.54} exp(-2K_d Z) \tag{25}$$

where,

$K_d$: attenuation coefficient of downwelling irradiance ($m^{-1}$).

$Z$: depth (m).

Dierssen et al. (2003) suggested a method that is a derivation of Beer's Law for retrieving the irradiance reflectance ($E_u/E_d$) of the bottom ($R^b$ ).

$$R^b = \frac{R_{rs} Q_b}{t} \frac{exp(-K_{Lu} Z)}{exp(-K_d Z)} \tag{26}$$

where,

$Q_b$: ratio Eu/Lu at the bottom interface and was assumed to be π.

$K_{Lu}$: attenuation coefficient of upwelling radiance ($m^{-1}$).

$t$: transmittance of upwelling radiance and downwelling irradiance across the air–water interface and was assumed as 0.54 (MOBLEY, 1994).

Some index may be used on bottom reflectance to extract additional information about the submerged targets of interest. The Normalized Difference Vegetation Index (NDVI), which is a normalized ratio of red and near-infrared reflectance, has been used in many vegetation studies. However, the near-infrared is not efficient to study water bodies. An alternative index to study the vegetation has been used the Green-Red Vegetation Index (GRVI) (FALKOWSKI et al., 2005; MOTOHKA et al., 2010). Slope between the wavelength in green band (560 nm) and red band (660 nm) also was used successfully in papers to study water bodies (DASH et al., 2011).

$$\boldsymbol{GRVI} = \frac{\boldsymbol{R_{rs}[Green_{(560\ nm)}] - R_{rs}[Red_{(660\ nm)}]}}{\boldsymbol{R_{rs}[Green_{(560\ nm)}] + R_{rs}[Red_{(660\ nm)}]}} \tag{27}$$

$$\boldsymbol{Slope}\ \{\boldsymbol{R_{rs}[Green_{(560\ nm)}] : R_{rs}[Red_{(660\ nm)}]}\} = \frac{\boldsymbol{R_{rs}[Green_{(560\ nm)}] - R_{rs}[Red_{(660\ nm)}]}}{\boldsymbol{660-560}} \tag{28}$$

# 3. STUDY SITE

Figure 1 – Location of the Nova Avanhandava Reservoir in (a) Brazil and (b) São Paulo state. A true colour satellite image acquired by Landsat OLI sensor (2013-07-04) shows the reservoir and the surrounding land cover (c). The red rectangle indicates the actual research site (Bonito River).

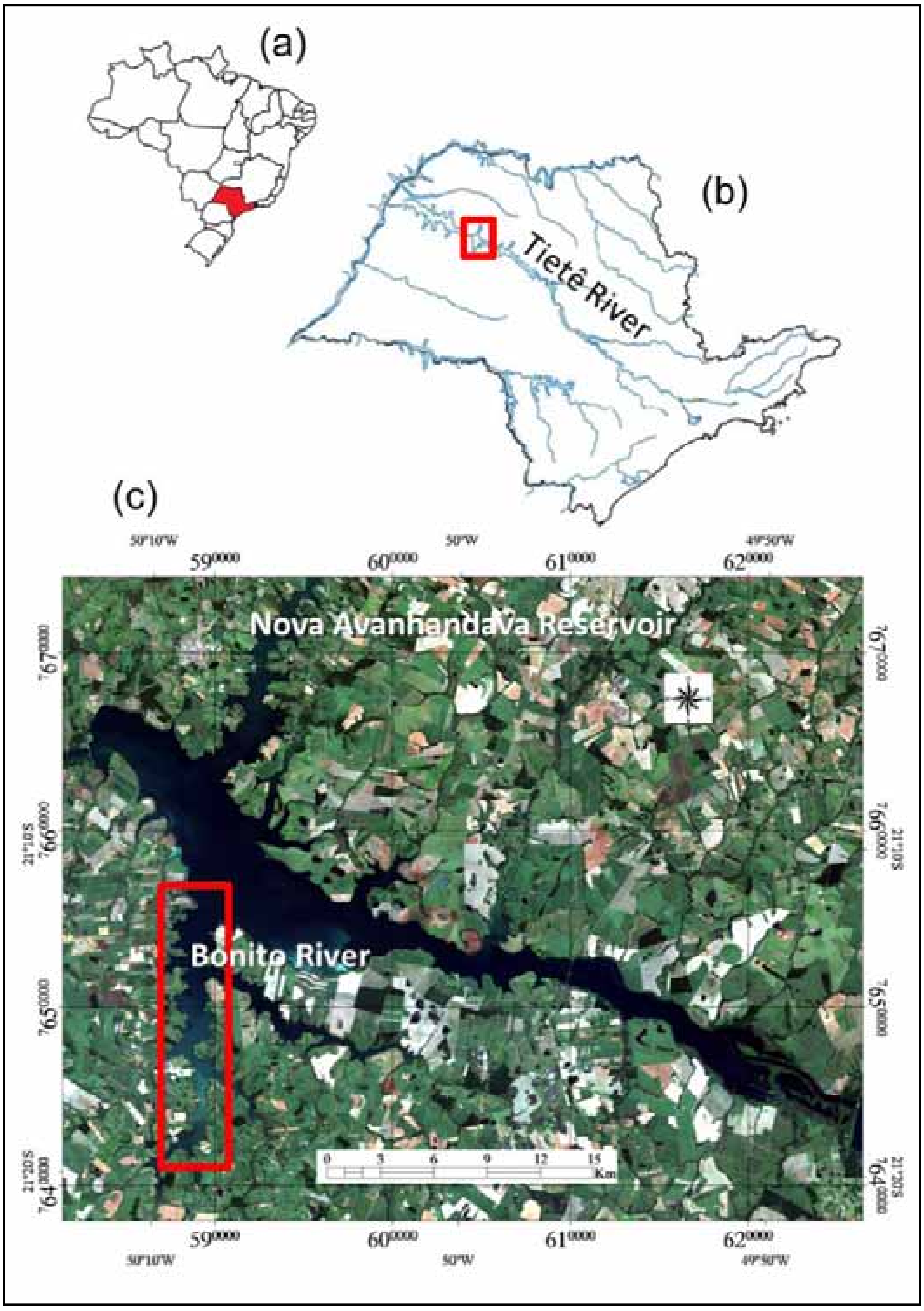

This study was performed in the Bonito River, which is a tributary of the Tietê River and part of the Nova Avanhandava Reservoir (Table 1) in the Brazilian state of São Paulo. The Tietê River is fully located in São Paulo (Figure 1). It is approximately 1,100 Km long. Its source is on the Serra do Mar (Sea Ridge) escarpments, 22 km inland, and its mouth is at the Paraná River where the São Paulo state borders Mato Grosso do Sul (SSRH/CRHi, 2011).

Table 1 – Primary characteristics of the Nova Avanhandava Reservoir.

| Nova Avanhandava Reservoir | |
|---|---|
| First Year of Operation | 1982 |
| Location | Tietê River, Rod. SP 461, km 44, Buritama - SP |
| Area | 210 km² |
| Volume | $2830 \times 10^6$ m³ |
| Dam Length | 2038 m |
| Level Difference | 29.7 m |
| Maximum Useful Height | 358 m |
| Minimum Useful Height | 356 m |

Adapted from AES Tietê (2013).

Nova Avanhandava Reservoir presents low level variability in both upstream and downstream. Figure 2 shows upstream level variability and Figure 3 shows downstream level variability of Nova Avanhandava Reservoir between January 2010 and December 2012. The level variation was less than 1 meter at upstream and round 3 meters at downstream.

The Nova Avanhandava Reservoir is in the 19th Water Resources Management Unit, Lower Tietê (Unidades de Gerenciamento de Recursos Hídricos 19 – Baixo Tiête/UGRHI 19 – BT), along with the Três Irmãos Reservoir (Table 1). The UGRHI 19 – BT has a 15,588 km² drainage area. The region’s economy is primarily based on agriculture and cattle farming, but sugar-cane cultivation has expanded recently, and agroindustry is the most significant segment of the local industry. Of the total area, 874 km² include vegetated areas (5.5% of the UGRHI area), and the primary formations are semi-deciduous forests and tree/shrub vegetation in floodplains (SSRH/CRHi, 2011). The geological units in the UGHRI 19 – BT area are primarily sandy clastic sediment and basaltic igneous rocks in the São Bento Group (Paraná Basin Mesozoic); sedimentary rock in the Bauru Group (from the Bauru Basin, Upper Cretaceous); sediment from the Itaqueri Formation and correlated deposits (from the São Carlos and Santana mountain ranges) from the Cretaceous and Cenozoic eras; alluvial deposits associated with the drainage network; and colluvia and eluvia (CBH-BT, 2009).

Figure 2 – Upstream level of Nova Avanhandava Reservoir between January 2010 and December 2012.

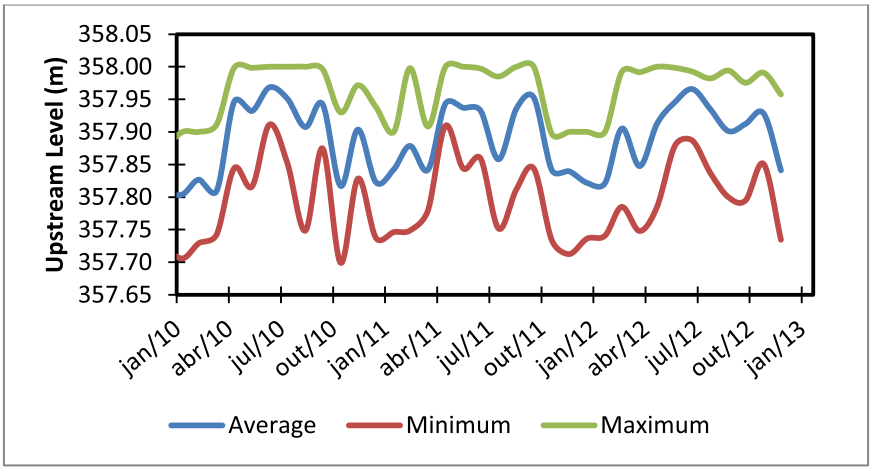


Adapted from AES Tietê (2013).

Figure 3 – Downstream level of Nova Avanhandava Reservoir between January 2010 and December 2012.

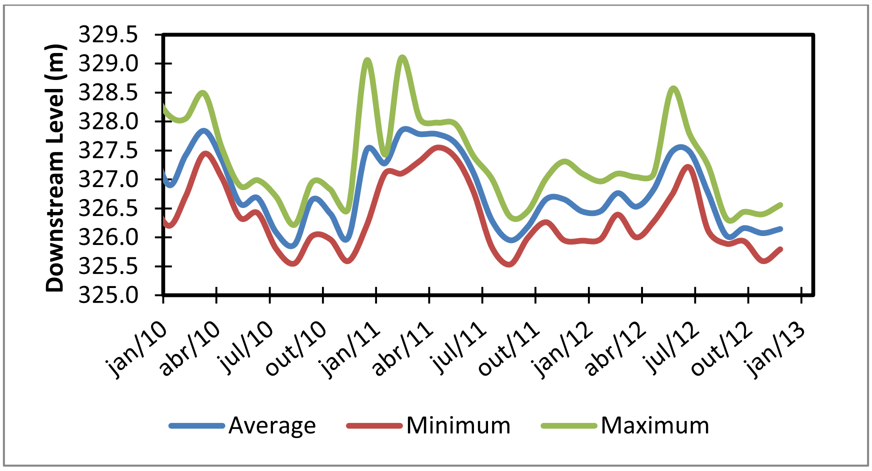


Adapted from AES Tietê (2013).

The Lower Tietê Basin geomorphology is characterized by a smooth relief with dissected plateaus that include rolling and gentle hills as well as sedimentary landforms with alluvial plains and river terraces. The Lower Tietê UGRHI is influenced by the continental tropical and Antarctic polar air masses. The rainfall pattern is typically tropical with a rainy season from October to April, a dry season from May to September and annual precipitation that varies between 1,000 and 1,300 mm. The minimum temperatures during the coldest month (July) range between 14°C and 22°C. Summer is hot and humid with strong rains, and the temperatures oscillate between 24°C and 30°C (CBH-BT/CETEC, 1999).

The closest weather station from the study field is located in José Bonifácio - SP, 50 km from the Bonito River. This station is controlled by the National Institute of Meteorology (Instituto Nacional de Meteorologia -INMET) and its activities started in September of 2007. The station has the following coordinates: latitude -21.085675°, longitude -49.920388°, altitude 408 m (http://www.inmet.gov.br/). Monthly average of temperature, global radiation, relative humidity, wind speed and precipitation between June 2010 and June 2013 are show in Figure 4 and Figure 5 .

Figure 4 – Average temperature and global radiation monthly in José Bonifácio meteorological station.

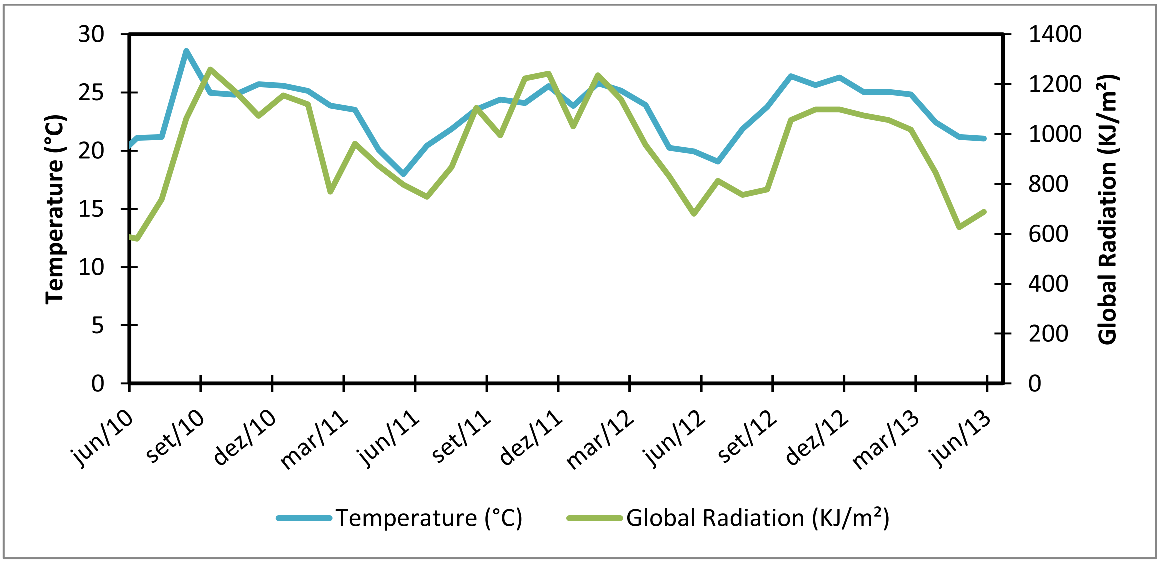


Adapted from <http://www.inmet.gov.br/>.

Figure 5 – Average relative humidity and wind speed and precipitation monthly in José Bonifácio meteorological station.

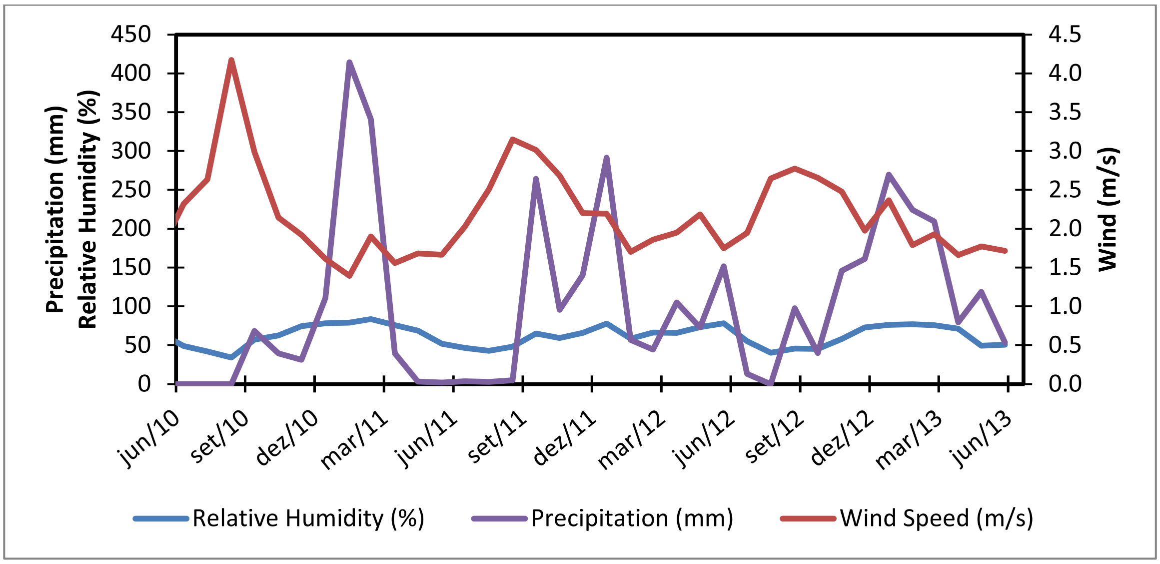


Adapted from <http://www.inmet.gov.br/>.

The temperature curve follows the global radiation, presenting lower values between May and August and higher values between October and February. During winter times, it was noted low precipitation and low relative humidity, presenting minimum values when close to August. The average wind speed did not present a high variability but it was noted higher values in September.

Effluent discharged in Tietê River upstream by São Paulo city causes high nutrients and suspended solids concentration. However, reservoirs chain help in the nutrients depuration and suspended solids decantation. Thus, Nova Avanhandava reservoir presents low nutrients concentration in the water and high transparency (RODGHER, et al., 2005). This characteristic supports the SAV development.

Study conducted in 2001/2002 showed that macrophytes of greater importance in Nova Avanhandava Reservoir are: Egeria densa and Egeria najas (submerged), Typha angustifolia and Cyperus difformis (emergent), and Eichhornia crassipes and Eichhornia azurea (floating) (CAVENAGHI et al., 2003).

Figure 6 shows the specie *Egeria spp*. found in Bonito River, Nova Avanhandava Reservoir, in October, 2012. These species are predominant in the whole Bonito River.

Figure 6 – Submerse aquatic vegetation (*Egeria spp*.) found in the reservoir of Nova Avanhandava-SP in October 2012.

# 4. MATERIAL AND METHOD

## 4.1 First field campaign

In September 2012, it was done a preliminary data collection to have a better understanding of the area study and the target (Submerged Aquatic Vegetation). With this dataset, it was developed a procedure to assess the subaquatic radiation availability in the water column and the total suspended solid concentration (TSS) in the Nova Avanhandava Reservoir and analyze its influence on SAV initiation and development.

Four sampling stations (P01, P02, P03 and P04) were considered for both spectroradiometer measurements and water sampling for analytical determination of the TSS. Based on the four sampling stations, the river was split into four regions (blue circles in Figure 7) to assess the relationship between water quality parameters and SAV behaviour. The shorter distance between the sampling points was 3 km. Therefore, the radius for the regions studied was approximately 1.5 km to not have overlap among these regions. During the field trip, we collected data on SAV habitats in each region using sonar equipment, which was mounted under a boat that followed the red paths indicated in Figure 7. Field data collected for this research included TSS, SAV height, water depth, and optical measurements such as downwelling irradiance ($E_d$).

Figure 7 – Sampling stations (black dots), the hydroacustic data collection transects (dotted red line), and four regions (blue) used in analysis are shown inside the Bonito River (black outline).

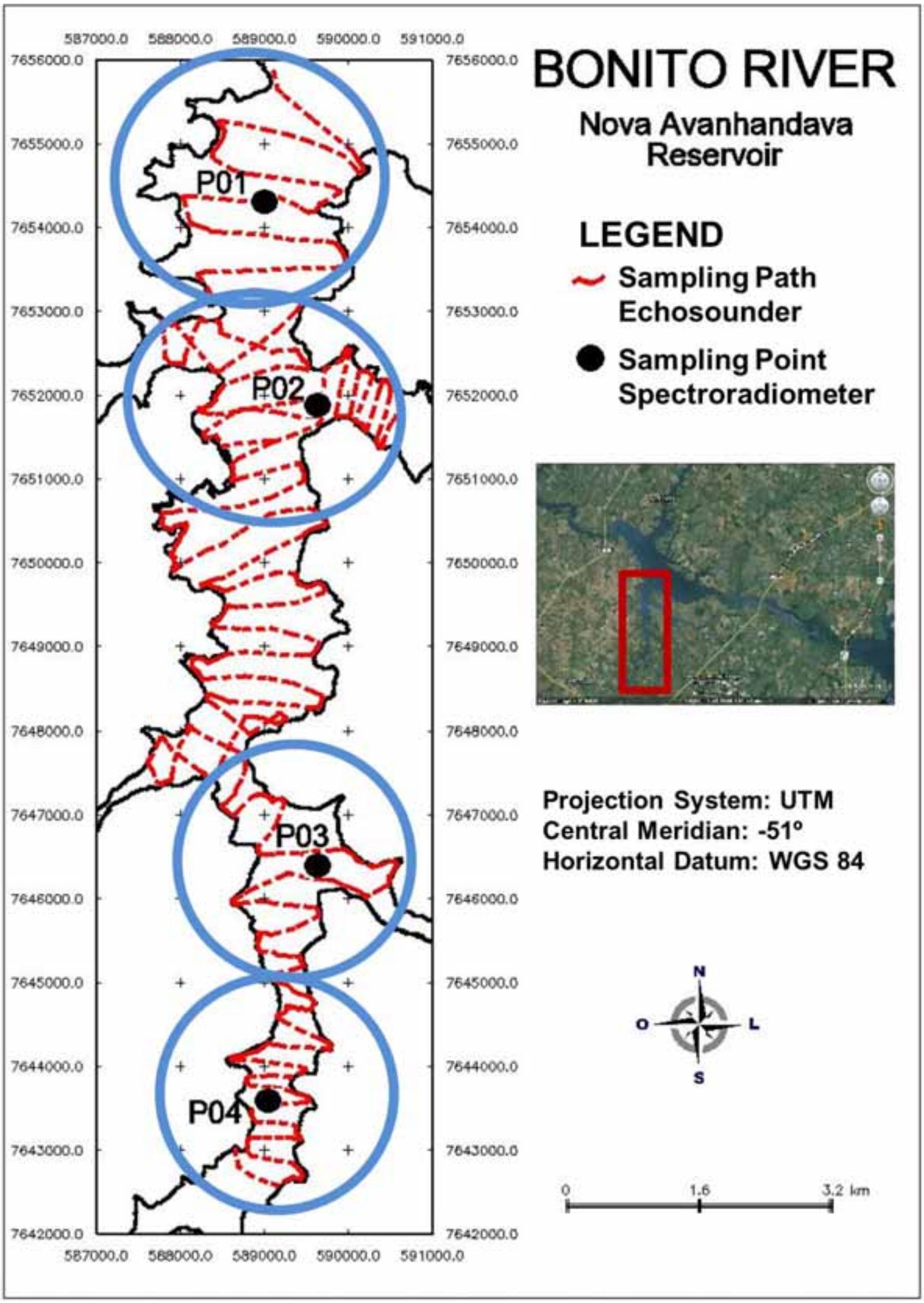

### 4.1.1 Suspended Solids Measurement

The suspended solids were characterized using the method described in Clesceri et al. (1998). At each sampling station, two litres of water were collected and filtered through fiberglass (type GF/F); the filters were dried in an oven at 105°C and then combusted in a muffle furnace at 550°C. The weights were measured using a precision scale, to derive the following concentration measurements, fixed suspended solids (FSS) which represent the concentration of inorganic solids in suspension; volatile suspended solids (VSS) which represent the concentration of organic solids in suspension; and total suspended solids (TSS) which is the sum of the two above fractions.

### 4.1.2 Hyperspectral downwelling irradiance

Hyperspectral downwelling irradiance ($E_d$) data were collected in September 18th and 19th using the TriOS/RAMSES optical sensor (Company site: http://www.trios.de). $E_d$ data is essential in estimating water column attenuation and radiation availability at the top of canopy (MISHRA et al., 2005). Hyperspectral $E_d$ data were collected above the water surface (0+) (Figure 8 (a)), just below the surface (0-) (Figure 8 (b)), and at various depth intervals (1 m, 2 m, 3 m, 5 m and 7 m) in the water column at the four sampling stations.

Figure 8 – TriOS optical sensor deployment for $E_d$ measurements above water (a) and below water (b).

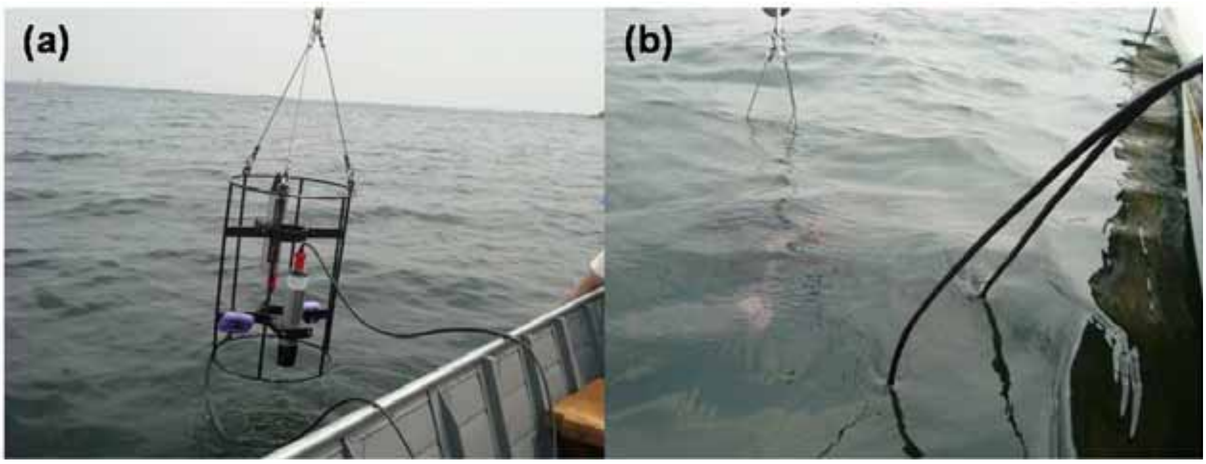

The normalization of the downwelling irradiance should be done because of variations in incident surface irradiance. The normalization is done based on $E_s$ (Equation (5)). $E_s$ is the incident surface irradiance measured on the boat. In this field campaign (June 2012) we did not have $E_s$ data, so, it was necessary to calculate the $E_s$ from $L_p$ measured on the reference panel. This procedure is described in Li et al. (2013).

$$E_s = \frac{\pi L_p}{\rho_p} \tag{29}$$

where,
$L_p$: radiance from reference panel;
$\rho_p$: stands for the reflectance of reference panel.

After calculate the $E_s$ and the Normalization Factor (Equation (5)), the $E_d$ was normalized (Equation (6)).

#### 4.1.2.1 Diffuse attenuation coefficient ($K_d$)

The normalized spectral $E_d$ was used to calculate the $E_d$ *PAR*. PAR (Photosynthetically Active Radiation) comprehend the spectrum range of solar radiation from 400 nm to 700 nm. So, the spectral $E_d$ was integrated between 400 nm and 700 nm to obtain $E_d$ *PAR.* Then, the $K_d$ *PAR* was calculated based on $E_d$ *PAR* (Equation (13)). Finally, the euphotic zone depth ($Z_{EZ}$) was calculated (Equation (16)).

### 4.1.3 Echosounder data

To assess the influence of vertical attenuation of $E_d$ and TSS on SAV behaviour, depth, SAV height, and precise position were also collected through hydroacoustic measurements. Depth and SAV height were collected in October, between 3$^{rd}$ and 5$^{th}$, using the scientific digital sonar BioSonics DT-X (Echosounder) (Company site: http://www.biosonicsinc.com/). Acoustic data recorded in numerous transects corresponded to a total length of 72 km (red dashed lines in Figure 7). The

DT-X Echosounder included a surface unit with a dedicated processor for operation, which generated the electrical signal and controlled the transducer. The transducer was connected to the surface unit by a cable and converted the electrical signal from the surface unit into an acoustic pulse and the pulse's echo into electric signal (BIOSONICS, 2004). An external communication device (notebook) connected via an ethernet interface was used to load the system operating parameters as well as display and store the data received from the echosounder. A GPS was connected to the surface unit and provided position information for the acoustic data (Figure 9).

Figure 9 – Components of the DT-X Echosounder deployed to acquire depth and SAV heigh data along numerous transects.

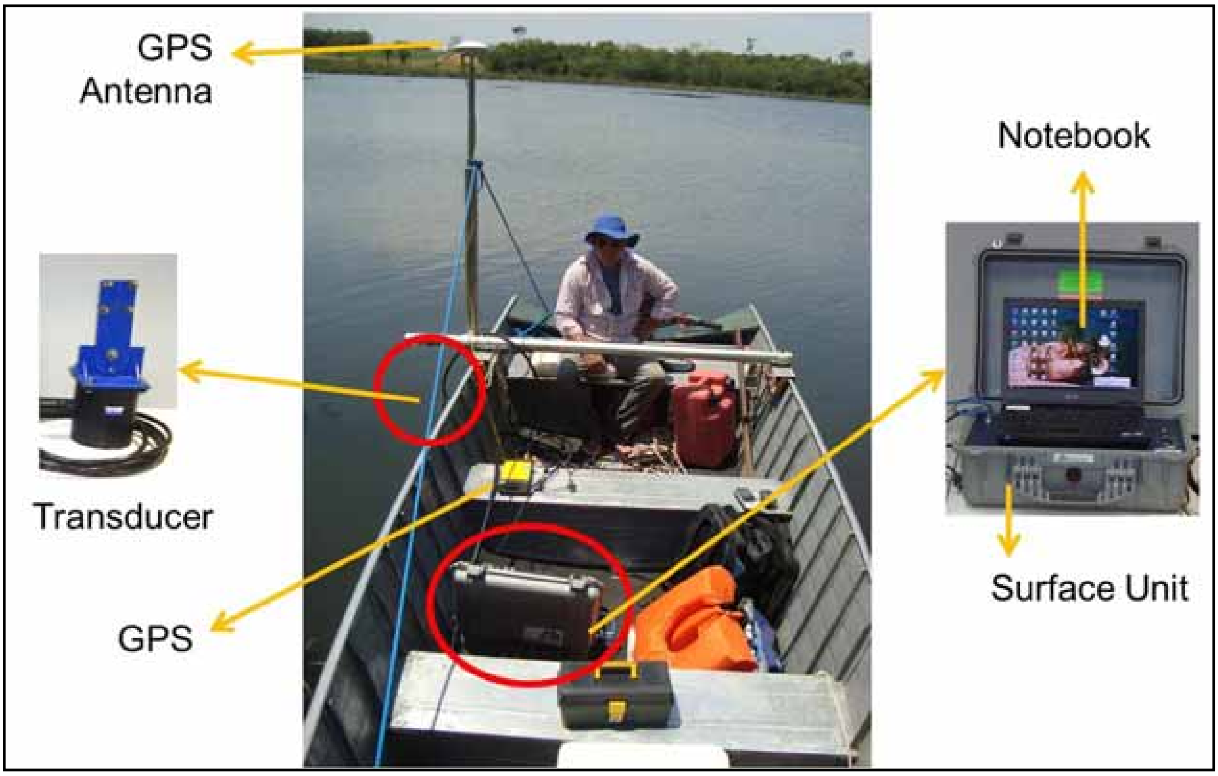


The echosounder transducer was vertically positioned at 0.5 m deep on one side of the boat, and the GPS antenna was positioned at the opposite end on the same pole. The data collected using the echosounder was visualised in real time via the notebook and stored in separate files for each river transect. The system was controlled using the *Visual Acquisition* software (Biosonics), which displays an echogram that describes the submerged relief depth and presence or absence of submerged aquatic macrophytes. The sensor emits 10 acoustic pulses every 2 seconds. After processing through *EcoSAV*, each set of 10 pulses yields a line in an ASCII file that contains the day, time of day, position (Lat, Long), depth (m), coverage (%), and mean height for the submerged vegetation (BIOSONICS, 2008). Rotta et al. (2012) used this equipment and software for submerged aquatic vegetation mapping.

#### 4.1.3.1 SAV Height Interpolation

The SAV height distribution collected by biosonics echosounder was used to produce a map. The interpolation method used was ordinary kriging. Ordinary kriging is used to estimate a value at a point of a region for which a variogram is known, using data in neighborhood of the estimation location (GOOVAERTS, 1997, WACKERNAGEL, 2003). Kriging extracts information from the semivariogram to find optimal weights that it associates with the samples to estimate the value at a given point (LANDIM, 1998). In ordinary kriging, the global mean value is not required for input as compared simple kriging (BAILEY and GATRELL, 1995). First, four semivariograms were generated in distinct directions, 0º, 45º, 90º, and 135º to analyze variability in each direction. Because the semivariograms displayed similar behaviour, the phenomenon was considered isotropic (i.e., same variability for each direction). Figure 10 shows the omnidirectional (isotropic) semivariogram used to interpolate the SAV height data. The semivariogram function was modelled to describe spatial variation and thus, estimate or predict values at points that were not sampled or in large blocks through kriging (WEBSTER and OLIVER, 2007).

Using the fitted model, a numerical matrix representing the SAV heights was generated. Finally, this matrix was sliced into eight thematic classes including no occurrence, 0 – 0.5 m, 0.5 – 1.0 m, 1.0 – 1.5 m, 1.5 – 2.0 m, 2.0 – 2.5 m, 2.5 – 3.0 m and > 3.0 m.

Figure 10 – Isotropic semivariogram for the SAV height data. A quadratic model was fitted to the data with nugget, sill, and range values at 0.2, 0.5 and 380, respectively. The fitted model is represented by the blue line.

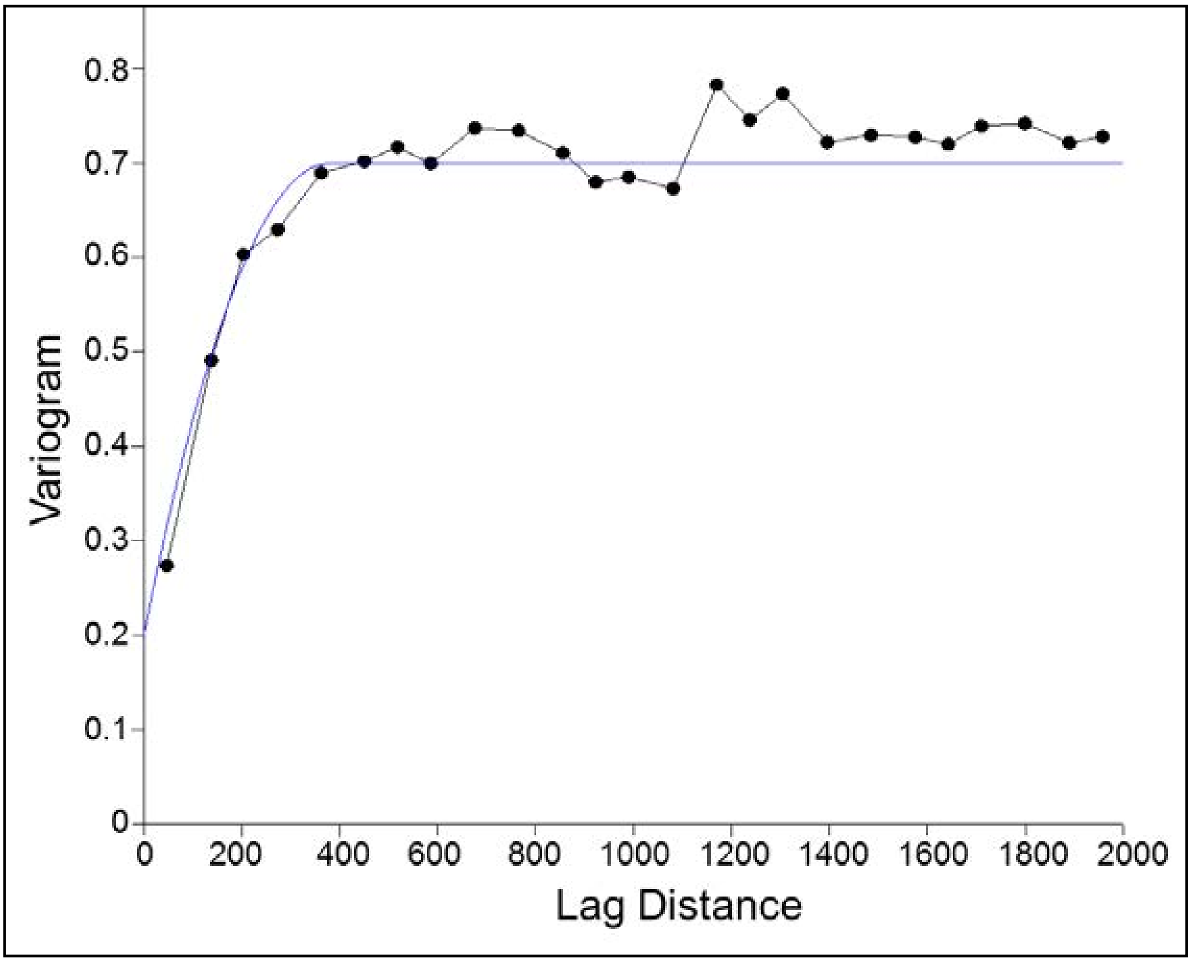


### 4.1.4 The relationship between SAV and radiation availability

The hyperspectral downwelling irradiance data was used to compute vertical attenuation coefficient values up to 7m depth to calculate the diffuse attenuation coefficients $K_{d,}$ and euphotic zone depths for each sampling station. The SAV heights and depths were determined using echosounder measurements. The depth data were split at 1m interval ranging from 0 to 10 m to analyze the descriptive statistics of SAV height. Boxplots with SAV height data at each depth were generated. Based on the data collected using the echosounder, we generated a dispersion plot for the SAV heights as function of depth in each region. Using that information, we observed and analyzed the influence of radiation availability on SAV incidence and development.

In addition, two optical parameters which act as proxy to radiation availability in SAV habitats were computed. These two parameters are: (1) Percentage Light through the Water (PLW) and (2) Percentage Light at the Leaf (PLL). PLW (Equation (1)) is a measure of the light transmitted through the water column to the depth of SAV growth, and PLL (Equation (2)) considers the additional light attenuation by epiphytic materials (KEMP et al., 2004).

### 4.2 Second field campaign

Several models were developed to retrieve the spectral response of the bottom of water bodies; however their suitability to estimate the spectral albedo in Brazilian reservoirs is not well known. Therefore, based on second dataset collected on June/July 2013 in Nova Avanhandava Reservoir, some bio-optical models were evaluated to retrieve the bottom reflectance and estimate the SAV height in study area. The better models were chosen to be evaluated and applied on satellite multispectral image, SPOT-6, to estimate SAV height. In this sense it was needed to apply an atmospheric correction to the image. With the red and green bands corrected atmospherically it was calculated the GRVI and Slope.

A survey in the studied area (Bonito River) was done to gather information about the apparent optical properties (AOP) and inherent optical properties (IOP) of the water between June 28$^{th}$ and 30$^{th}$, 2013. Twenty sampling points were selected: eight points were located in places with the SAV presence (P03, P05, P09, P11, P13, P15, P17 e P20) and twelve points in places without the presence of SAV (P01, P02, P04, P06, P08, P10, P12, P14, P16, P18 e P19) (Figure 11). Furthermore, on the July 4th and 5th, a survey was done using the echosounder in order to gather the SAV height and position and the water body depth information. (Figure 11, yellow lines). The Table 2 shows the depth for each sample station.

Figure 11 – Sampling stations with SAV (Green dots) and without SAV (Red dots) and hydroacoustic data collection transects (Yellow line).

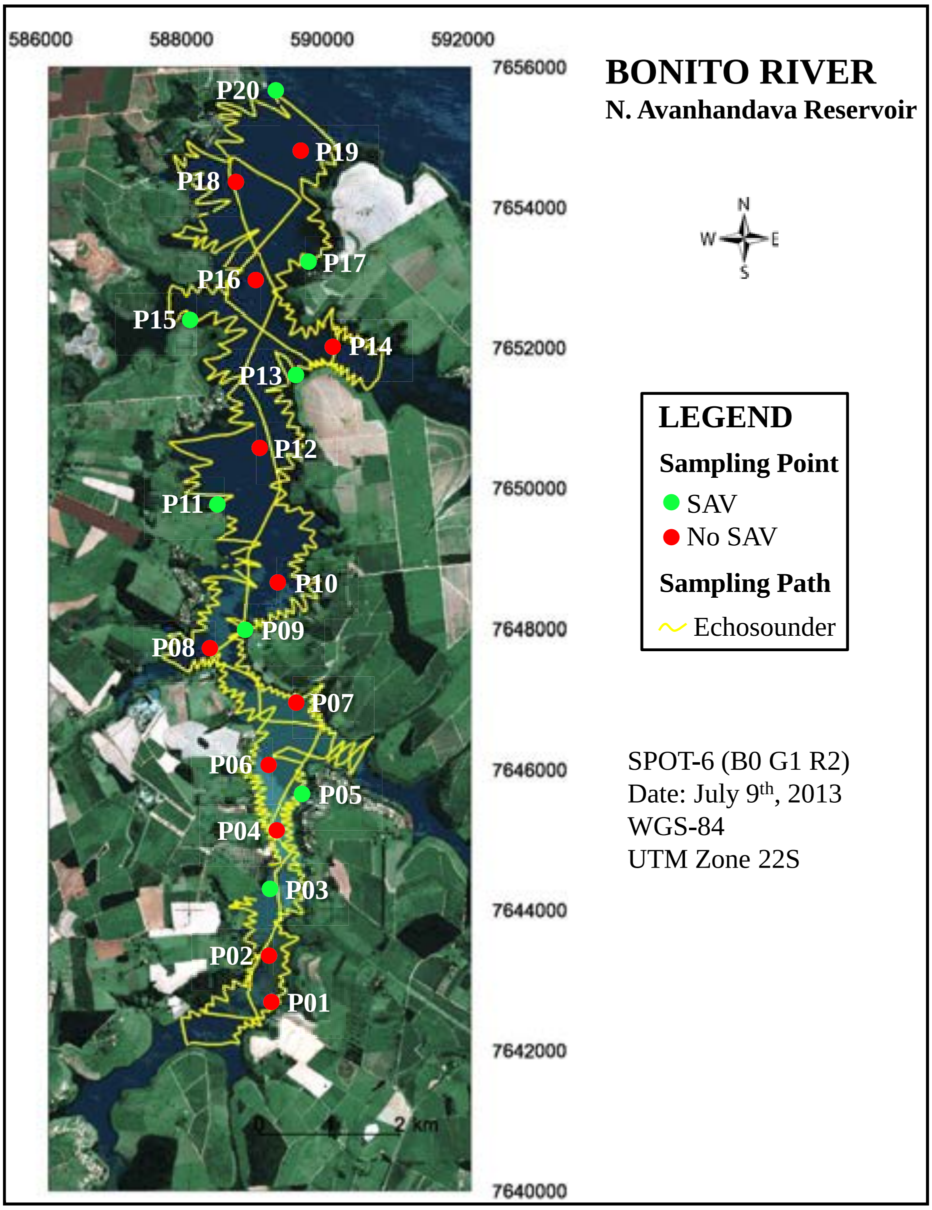


Table 2 – Depth for each sample station

| Sampling Station | Depth (m) | Sampling Station | Depth (m) |
|---|---|---|---|
| P01 | 8.2 | P11 | 3.8 |
| P02 | 13.4 | P12 | 22.0 |
| P03 | 5.3 | P13 | 3.8 |
| P04 | 12.8 | P14 | 20.8 |
| P05 | 5.8 | P15 | 2.8 |
| P06 | 11.8 | P16 | 20.6 |
| P07 | 9.5 | P17 | 4.0 |
| P08 | 16.8 | P18 | 20.0 |
| P09 | 2.8 | P19 | 22.7 |
| P10 | 17.0 | P20 | 1.4 |

### 4.2.1 Apparent optical proprieties

A vertical profile of downwelling irradiance ($E_d$) and upwelling radiance ($L_u$) was acquired using the spectral sensors RAMSES/TriOs through the water at 1.0 meter depth interval. An additional sensor was used to measure the global solar irradiance ($E_s$) on the boat (Figure 12).

Figure 12 – Radiometers (RAMSES/TriOS) used to obtain hyperspectral data.

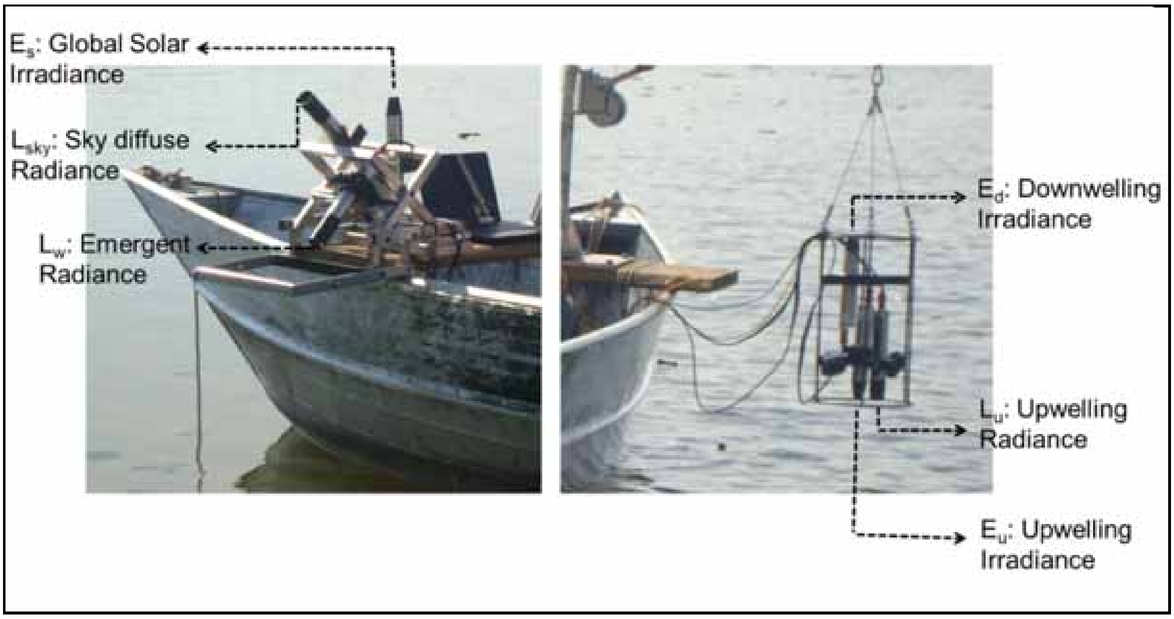


Figure 13 – Hyperspectral data collection using TriOS sensor.

### 4.2.2 Inherent optical proprieties

Measures of absorption, attenuation and backscattering coefficients were done in 20 sampling points as showed in Figure 11. In order to measure the absorption and attenuation coefficients the AC-S (Figure 14) was used. The AC-S sensor measures absorption and attenuation coefficients at depths up to 500 meters. The sensor has a 4 nm resolution between the 400 and 730 nm band lengths. In more than 80 different bands, the coefficient values provide a spectral signature capable of providing information related to chlorophyll-*a*, visibility, etc. (WET Labs, 2009).

Figure 14 – The AC-S measuring the absorption and attenuation coefficient.

The backscatter coefficient measurements were done by using the HidroScat sensor (Figure 15). The HydroScat-6P is a multispectral sensor that measures the water backscatter and water fluorescence. The sensor has six independent channels, each one being sensible to a different wave length, which are: 420, 442, 470, 510, 590 and 700 nm. The band width is 40 nm for the wave length of 700 nm and 10 nm for the remaining. The HydroScat-6P operates in temperatures between 0 and 30°C and at depths up to 300 meters on standard mode. Each backscatter sensor channel has its own optics, both the source and the receptor. The source produces a beam on the water and the detector collects the light portion that is scattered out of this beam. The generated light beam from a LED, chosen according to the desired wave length, goes through a lens to adjust its divergence and then through a prism. The receptor is composed by other identical prism, a filter that determines the exact wave length interval measurement, and a lens that focuses the received light beams to a silicon detector. The HydroScat geometry results in centered measurements in a scattering angle of 140° (HOBI Labs, 2010).

Figure 15 – Backscattering coefficient measured by HydroScat equipment.

### 4.2.3 Echosounder data

Depth and SAV height data were collected in July 4th and 5th, 2013 using the scientific digital sonar BioSonics DT-X (Echosounder). Echosounder data recorded in numerous transects is showed in Figure 11– yellow lines. It is possible to find SAV in whole reservoir and *E. densa* and *E. najas* are the main submerged vegetation in Bonito River.

Depth data was used in models for retrieve the bottom remote sensing reflectance. SAV height data were used to calibrate and validate the models for estimation of SAV height and distribution in Nova Avanhandava Reservoir.

Figure 16 – Submerged aquatic vegetation of Bonito River – Nova Avanhandava Reservoir.

The depth data was interpolated by ordinary kriging. Four semivariograms were generated in distinct directions, 0º, 45º, 90º, and 135º to analyze variability in each direction. Because the semivariograms displayed similar behavior, it was used an omnidirectional semivariogram to interpolate the depth data (Figure 17).

Figure 17 – Isotropic semivariogram for depth data. A spherical model was fitted to the data with nugget, sill, and range values at 0, 27 and 480, respectively. The fitted model is represented by the blue line.

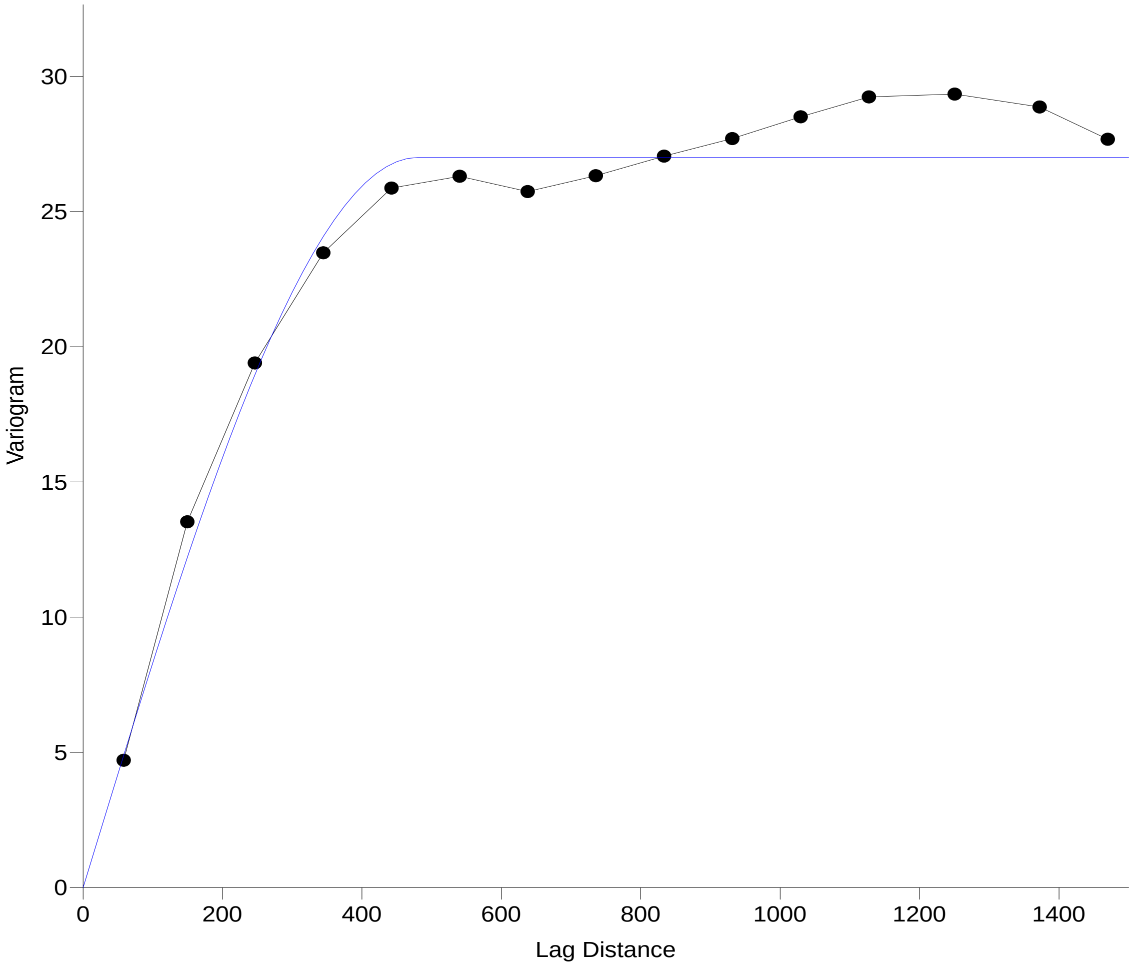


Using the fitted model, a numerical matrix representing the depth of the river was generated with the same SPOT-6 image pixel size (i.e. 6.7 m). This numerical matrix data was used in the models to retrieve the bottom reflectance. In addition, the numerical matrix was classified into eleven thematic classes: 0 – 1 m, 1 – 2 m, 2 – 3 m, 3 – 4 m, 4 – 5 m, 5 – 6 m, 6 – 7 m, 7 – 8 m, 8 – 9 m, 9 – 10 m and >10 m. Finally, descriptive statistic and histogram were performed in SAV height data to analyze its behavior.

### 4.2.4 Diffuse attenuation coefficient

Cloud cover variability can cause variations in incident surface irradiance, $E_s\ (z,\ \lambda)$. So, it was done the normalization of the scans (Equation (5)). The wavelengths 450 nm (Blue), 550 nm (Green) and 650 nm (Red) were selected to show an example on how the sky conditions changed during the measurements (

Figure 18). A normalization factor greater than 1 indicate lower irradiance, as clouds shadow, and values less than 1 indicate brighter conditions (MISHRA et al., 2005).

Figure 18 – Normalization factor at each scan in P13 showing the variation of illumination conditions.

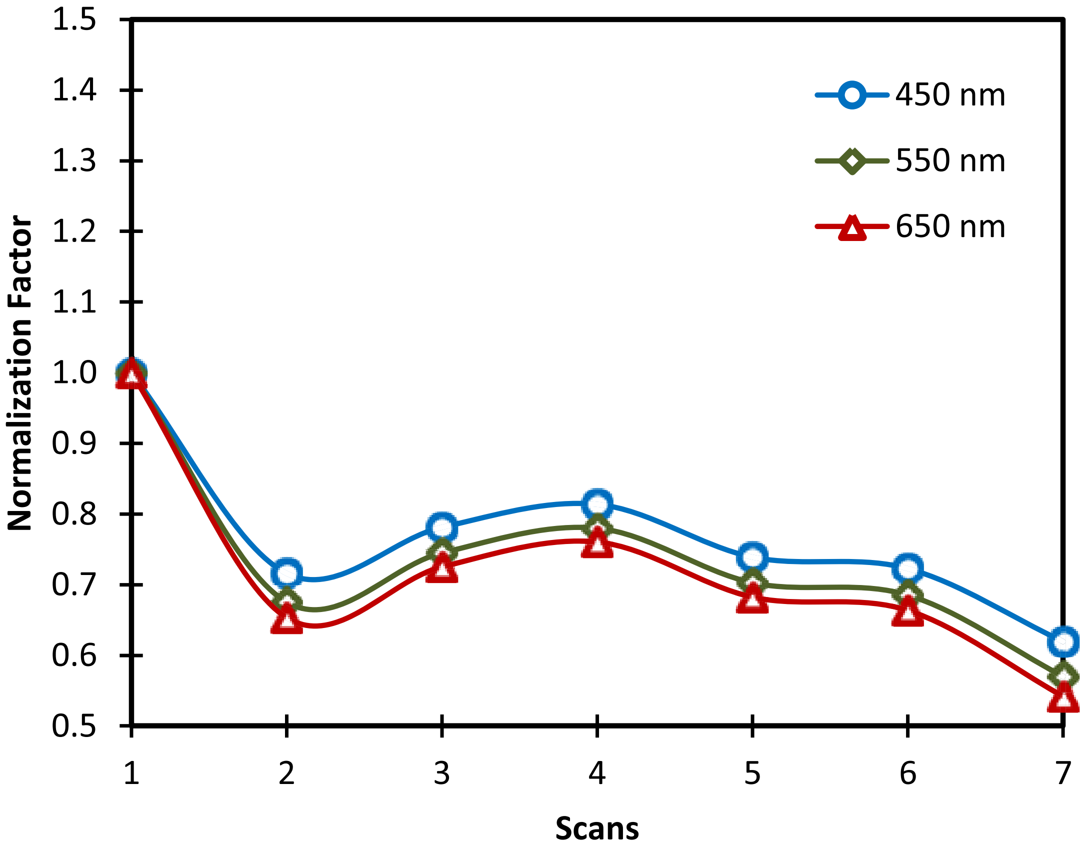


To normalize the spectral data and eliminate the noise due to change in illumination, the Equation (6) was used for the downwelling irradiance and the Equation (7) for upwelling radiance. Figure 19 shows the difference between the radiometric data before and after the normalization for point P13.

Scan 1 and Scan 2 before normalization (Figure 19 (a) and (c)) present similar values both for $E_d$ and $L_u$. This shouldn't have happened because the scans were acquired in different depths, so it means there was change in the illumination conditions. Those variations were corrected with the normalization (Figure 19 (b) and (d)).

Figure 19 – Downwelling irradiance before (a) and after (b) normalization and upwelling radiance before (c) and after (d) normalization in P13

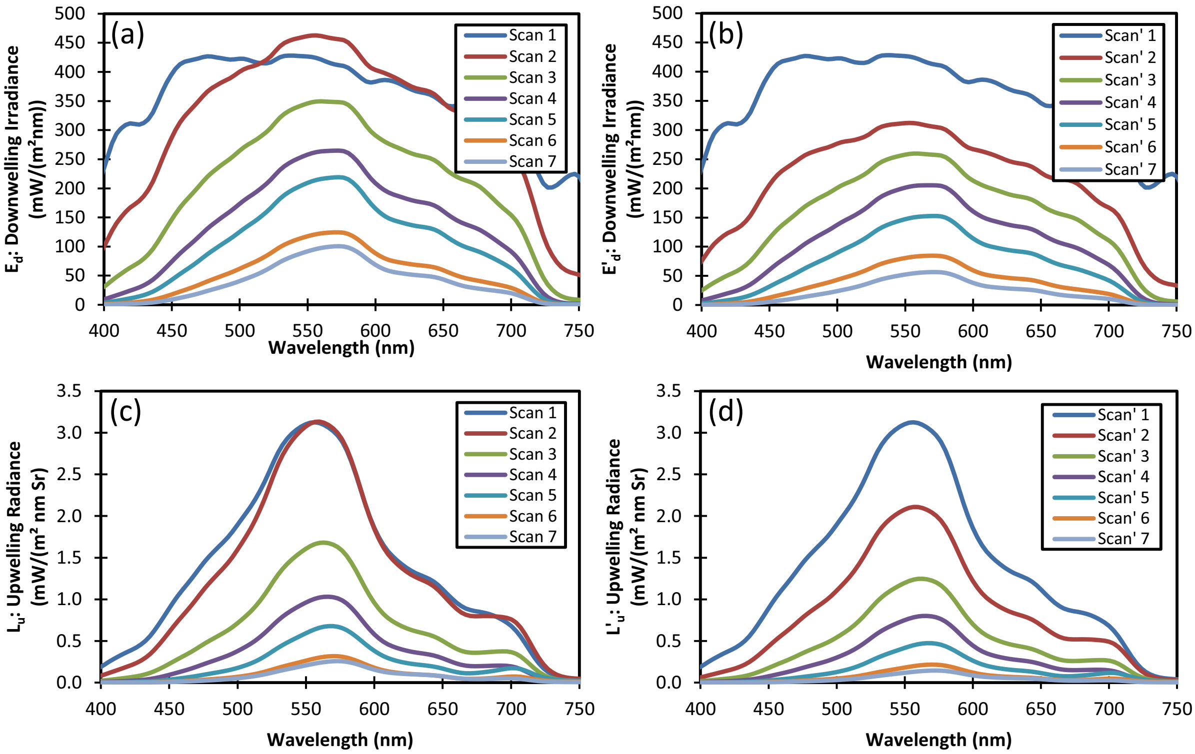


After the normalization procedure, the diffuse attenuation coefficients were calculated. Equation (6) was used to calculate $K_d$ and Equation (8) was used to calculate $K_{Lu}$.

The $K_d$ also was calculated using the inherent optical properties (IOPs) of the water using the Equation (9). Figure 20 shows the difference between diffuse attenuation coefficient using $a$ and $b_b$ (Equation (9)) and using $E_d$ (Equation (6)). Both values were similar, so it is possible to use any methodology to obtain $K_d$. The only significant difference was in 700 nm that is not important for our work. Therefore, we chose to use the $K_d$ ($E_d$).

Figure 20 – Diffuse attenuation coefficient based on attenuation and backscattering coefficients ($K_d$ ($a$, $b_b$)) and based on downwelling irradiance ($K_d$ ($E_d$)).

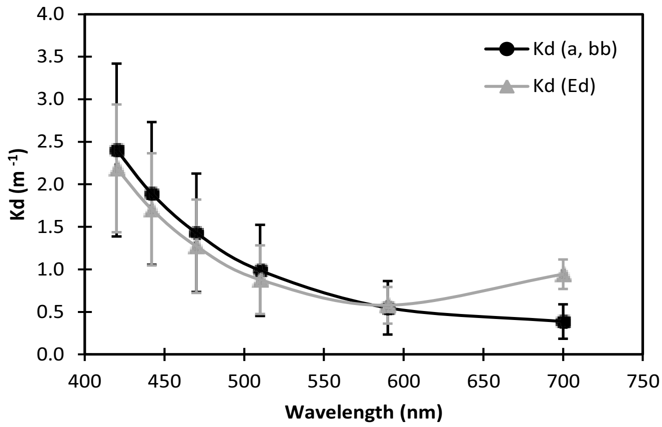


The $K_d$ proposed by Palandro et al. (2008) was also calculated (Equation (10)). This methodology uses the remote sensing reflectance of satellite images and depth to estimate the $K_d$. In this study, this diffuse attenuation coefficient is described as $K_d{}^P$. This coefficient was also used in the retrieval models of the bottom.

### 4.2.5 In situ remote sensing reflectance

Based on in situ data, remote sensing reflectance above-water ($R_{rs}$) was calculated according Dall'Olmo and Gitelson (2005) and Gitelson et al. (2008) (Equation (17)). Multispectral bands of Landsat 8 and SPOT6 were simulated from remote sensing reflectance. The relative spectral response of OLI/Landsat 8 (GSFC/NASA, 2014; BARSI et al.,2014) and SPOT 6 (ASTRIUM, 2013) were used to simulate the bands of each sensor.

Figure 21 – Relative spectral response of OLI/Landsat 8 (a) and SPOT 6 (b).

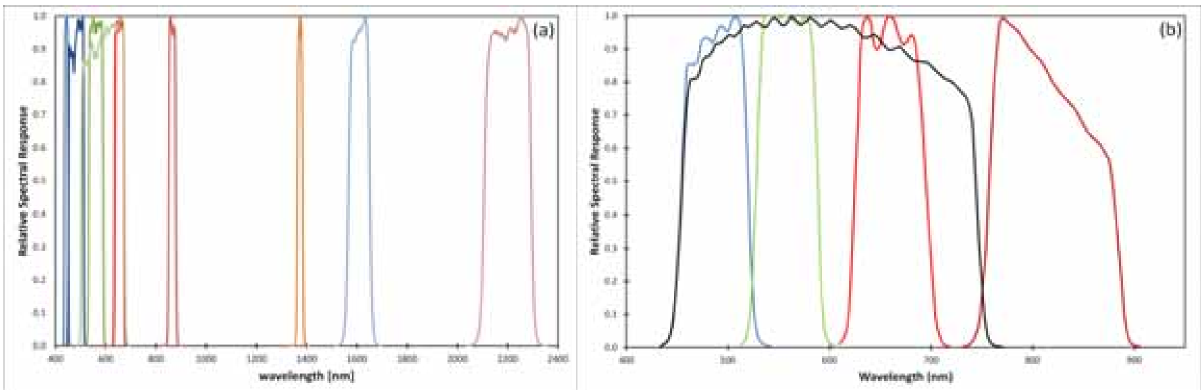

The Landsat series of satellites provides the longest temporal record of space-based surface observations. The first Landsat satellite was launched in 1972. The series was continued with Landsat 8 launched February 11th 2013 from Vandenburg Air Force Base, California (ROY et al., 2014).

The Landsat 8 has two sensors: Operational Land Imager (OLI) and the Thermal Infrared Sensor (TIRS) (IRONS et al., 2012). An addition band centered at 443 nm (Coastal band) and 12-bits radiometric resolution are improved features of OLI compared with prior Landsat sensors. The better data quality of that sensor allows expanding existing applications of Landsat imagery in aquatic sciences, such as retrieval of Chlorophyll-a, total suspended solids and benthic mapping (PAHLEVAN et al., 2014).

MUMBY et al. (2004) indicated the possibility to study reef geomorphology, location of shallow reef areas, reef community (<5 classes), Bathymetry and coastal land use by Landsat and SPOT images. SPOT 6 and SPOT 7 are designed to extend SPOT 5's success to the 1.5 m product family. These instruments acquire images in mode panchromatic and multispectral (4 bands) with pixel size of 1.5 m and 6 m, respectively (ASTRIUM, 2013).

Table 3 – Multispectral bands of OLI/Landsat 8 and SPOT 6.

| | **OLI/Landsat 8** | **SPOT 6** |
|---|---|---|
| Coastal | 430 – 450 nm | |
| Blue | 450 – 510 nm | 455 – 525 nm |
| Green | 530 – 590 nm | 530 – 590 nm |
| Red | 640 – 670 nm | 625 – 695 nm |
| Near-Infrared | 850 – 880 nm | 760 – 890 nm |
| SWIR | 1570 – 1650 nm | |
| SWIR | 2110 – 2290 nm | |
| Cirrus | 1360 – 1380 nm | |

### 4.2.6 Satellite data

The SPOT-6 image was used due to the high spatial resolution; despite its low spectral resolution. The Table 4 shows the main characteristics of SPOT-6 image acquired on Nova Avanhandava Reservoir.

Table 4 – SPOT-6 image characteristics.

| | |
|---|---|
| Acquisition date | 2013-07-09 |
| Acquisition time | 13:08:43.5 |
| Number of spectral bands | 4 (B0 B1 B2 B3) |
| Across angle | -6.60018867713° |
| Along angle | 19.1336359344° |
| Coordinate Reference System | WGS-84 |
| Resampling Distance | 6.70651 |

#### 4.2.6.1 Atmospheric correction

FLAASH (Fast Line-of-sight Atmospheric Analysis of Spectral Hypercubes) is an atmospheric correction tool based on MODTRAN4 (MODerate spectral resolution atmospheric TRANsmittance algorithm and computer model) (ADLER-GOLDEN et al., 1999). Users have limited control over the choice and setting of input parameters in FLAASH. This program is simple to execute, but the user have to be able to specify appropriate input parameters that characterize the atmospheric conditions and illumination/viewing geometry at the time of image acquisition. Default values based on theoretical estimates and information from the literature are used as input parameters when actual measurements are not available (MOSES et al., 2012).

FLAASH was tested to SPOT image atmospheric correction, but we did not have success, probably, because of the lack of appropriate parameters to characterize the atmospheric conditions at the time of image acquisition. It was obtained several negative pixels, so the work was not able to proceed. Similar problem was reported by Moses et al. (2012) that inserted different types of aerosols trying to minimize the negative values obtained with the atmospheric correction using FLAASH. When he compared to reflectance spectra measured in situ, the reflectance features were distorted in the FLAASH-derived reflectance spectra, especially in the red and NIR regions. Therefore, it was decided to use the empirical line method to correct atmospherically the SPOT image.

The main characteristic of empirical line method is to establish a linear regression equation between the ground target and the corresponding pixel of remote sensing image. The empirical line method assumes that there are targets with different reflectance characteristics covering a wide range of reflectance recorded by the bands of the sensor. The reflectance of each target is measured by a field spectrometer and the radiance of that target is measured by a satellite sensor. A regression equation is developed for each waveband. Illumination and atmospheric effects are corrected by this method. The remotely sensed data produce images in reflectance units (SMITH and MILTON, 1999; KARPOUZLI and MALTHUS, 2003; GUO and ZENG, 2012).

Remote sensing reflectance measured at 10 sampling points in the field (P01, P03, P04, P07, P09, P12, P13, P16, P18 and P20; Figure 11) was used to adjust the regression to perform atmospheric correction using empirical line method. The remote sensing reflectance of the others 10 sampling points (P02, P05, P06, P08, P10, P11, P14, P15, P17 and P19; Figure 11) was used to validate the regression. The atmospheric correction was performed only for the bands B1 (Green) and B2 (Red) because those were the bands used for the SAV height estimation models.

### 4.2.7 Bottom reflectance

We tested methods to retrieve the bottom reflectance from remote sensing reflectance (LEE et al., 1994; MARITORENA et al., 1994; LEE et al., 1999; LEE and CARDER, 2002); however those models did not present satisfactory results. Therefore, it was analyzed two different methods for retrieving the bottom reflectance from remote sensing reflectance above the interface air-water ($R_{rs}$). The first method was proposed by Palandro et al. (2008), and $K_d$ is used to remove water-column attenuation effect from $R_{rs,}$ thus obtaining the remote sensing reflectance of the bottom ($R_{rs}^{b}$) (Equation (25)). In this case, it is assumed that the downwelling and upwelling attenuation coefficients are the same, so $2*K_d$ was used in the equation. The second method is a derivation of Beer's Law for retrieving the irradiance reflectance ($E_u/E_d$) of the bottom ($R^b$ ) suggested by Dierssen et al. (2003) (Equation (26)).

The model used to retrieve the bottom by Equation (25) (Palandro et al., 2008) was named in this work as **PAL08** and the model used to retrieve the bottom by Equation (26) (Dierssen et al., 2003) was named as **DIE03**.

### 4.2.8 Model calibration and validation for estimation of SAV height

It is difficult to use the NDVI in water bodies, due to the near-infrared is not efficient in those environments. Therefore, it was used the Green-Red Vegetation Index (GRVI), describe in Equation (27). The Slope was also used between the wavelengths corresponding to the green (560 nm) and the red (660 nm) bands (Equation (28)). This slope has been used by researches to study water bodies (DASH et al., 2011).

Therefore, the retrieved bottom by **PAL08** and **DIE03** were converted into two indexes: GRVI and Slope. The models used to estimate the SAV height were calibrated using the GRVI, or the Slope, with the SAV height measured by the echosounder. Two groups of models were calculated: (a) Based on in situ data; and (b) Based on satellite image.

(a) <u>Models based on in situ data:</u> Eight available points with SAV (Figure 11) were used to make the calibration with the field data.

(b) <u>Models based on satellite image</u>: For the models based on the satellite image calibration, twenty points scattered along the studied area were used.

The validations of the models were made based on the SPOT-6 image with 100 randomized points. Hence, it was just possible to make the validation in models that used the satellite image or simulated SPOT-6 data for the calibration.

### 4.2.9 SAV height mapping using SPOT-6 image

The bottom reflectance of the SPOT-6 image was retrieved using the following procedures: (a) model **DIE03** using $K_d$ and $K_{Lu}$; (b) model **DIE03** using $K_d^{\,P}$ and $K_{Lu}$ ; (c) model **PAL08** using $K_d$; and (d) model **PAL08** using $K_d^{\,P}$. So, we obtained four bottom reflectance images for Green and Red bands. The equations to retrieve the bottom reflectance were applied on the multispectral images through LEGAL (**L**inguagem **E**spacial para **G**eoprocessamento **Al**gébrico)/(Spacial Language for Algebric Geoprocessing), a language for consulting and special manipulation available in the geoprocessing software SPRING (http://www.dpi.inpe.br/spring/). After retrieval of the bottom reflectance for B1 (Green) and B2 (Red) bands of SPOT-6, the GRVI (Equation (27)) index and the Slope (Equation (28)) of those bands were calculated.

Five models based on the coefficient of determination ($R^2$) and RMSE were selected to be applied on SPOT-6 image for the estimation of SAV height in the study area. The characteristics of each model are presented in the Table 5.

Table 5 – Main characteristics of each model used on the mapping of SAV.

| | | **Bottom retrieved by:** | | **Diffuse attenuation coefficient used in bottom model** | | | **Index** | |
|---|---|---|---|---|---|---|---|---|
| | | **PAL08** | **DIE03** | $K_d$ | $K_d^{\,P}$ | $K_{Lu}$ | **GRVI** | **Slope** |
| **SAV Mapping** | **Model 1** | | x | x | | x | x | |
| | **Model 2** | x | | x | | | | x |
| | **Model 3** | x | | | x | | | x |
| | **Model 4** | | x | x | | x | | x |
| | **Model 5** | | x | | x | x | | x |

Model 1: $\boldsymbol{SAV = 0.6642\ ln(GRVI) + 1.7147}$ (30)

Model 2: $\boldsymbol{SAV = 0.2037\ ln(Slope) + 4.0353}$ (31)

Model 3: $\boldsymbol{SAV = 0.7366\ ln(Slope) + 8.8652}$ (32)

Model 4: $\boldsymbol{SAV = 0.6996\ ln(Slope) + 7.9125}$ (33)

Model 5: $\boldsymbol{SAV = 0.2738\ ln(Slope) + 4.2202}$ (34)

A mask was developed and applied in each model to differentiate regions with the occurrence of SAV from regions without the occurrence. This mask was built based on the Slope between bands Green and Red retrieved by **DIE03** using $K_d$ and $K_{Lu}$ derived from the field data ($E_d$ and $L_u$). Slope with value up to 0.00002 were associated to “SAV” class and values higher than 0.00002 to “No SAV” class.

The models were applied in LEGAL/SPRING having as result a numerical matrix keeping the spatial resolution of the used image (6.7 m). This numerical grid was classified in the following thematic classes: No SAV, 0.0 – 0.5 m, 0.5 – 1.0 m, 1.0 – 1.5 m and >1.5 m.

#### 4.2.9.1 SAV height map validation

To carry out the validation of maps generated, height information of the SAV available in the echosounder was used. 160 points were randomly selected to each class, in a total of 800 points of validation. Cross-tabulation between the observed points (Echosounder) and the calculated points (SAV Map) were made. Thus, the confusion matrix was calculated, which made it possible to calculate overall accuracy (Equation (35)) and the Kappa index - K (Equation (36)) of the SAV mapping.

The kappa coefficient of agreement or just Kappa (COHEN, 1960) is a discrete multivariate technique of use in accuracy assessment (CONGALTON, 1991). Remote sensing classification accuracy has traditionally been expressed by the overall accuracy percentage computed from the sum of the diagonal elements of the confusion matrix. Overall accuracy can give misleading and contradictory results, while the Kappa is shown to be a more discerning statistical tool for assessing the classification accuracy of different classifiers (FITZGERALD and LEES, 1994). Kappa has been used successfully on accuracy assessment of remotely sensed products (FITZGERALD and LEES, 1994; STEHMAN, 1997). To aid in the interpretation, the strength of agreement for various ranges of Kappa value was suggested by Landis and Koch (1977).

$$Overall\ Accuracy = \frac{\sum_{i=1}^{r} X_{ii}}{N} \tag{35}$$

$$\widehat{K} = \frac{N\sum_{i=1}^{r} X_{ii} - \sum_{i=1}^{r}(X_{i+} * X_{+i})}{N^2 - \sum_{i=1}^{r}(X_{i+} * X_{+i})} \tag{36}$$

where,

$N$: total number of observations;

$r$: number of rows in the matrix;

$X_{ii}$: number of observations in row $i$ and column $i$;

$X_{i+}$: marginal totals of row $i$;

$X_{+i}$: marginal totals of column $i$.

# 5. RESULTS AND DISCUSSION

The results and discussion were divided in three sections to reach the main objectives.

## 5.1 Relationship between radiation availability and submerged aquatic vegetation characteristics

This section is related to the following objective: To assess the subaquatic radiation availability in the water column and the total suspended solid concentration (TSS) in the Nova Avanhandava Reservoir and analyze its influence on SAV initiation and development. The results in this section are based on the first field campaign data.

### 5.1.1 Suspended solids

The suspended solids concentrations were measured at four sampling locations and the values are shown in Table 6. TSS and variability between sampling locations was low for the study area and the range was 0.95 mg/l. As expected, the sampling point located at the narrower portion of the reservoir showed the highest TSS level compared to the sampling points at the broader end, mainly because of water speed.

Table 6 – Suspended solids concentration and depths at the sampling locations. TSS: total suspended solids, FSS: fixed suspended solids, and VSS: volatile suspended solids.

| Point | TSS (mg/l) | FSS (mg/l) | VSS (mg/l) | Depth (m) |
|---|---|---|---|---|
| **P01** | 0.76 | 0.02 | 0.74 | 19 |
| **P02** | 0.75 | 0.00 | 0.75 | 14 |
| **P03** | 1.30 | 0.85 | 0.45 | 6 |
| **P04** | 1.71 | 0.94 | 0.77 | 13 |

The VSS (organic fraction) concentration values were similar for points P01, P02 and P04 and slightly lower at P03. Analysing the fixed suspended solids (inorganic fraction) yielded significant values only at points upstream P03 and P04.

### 5.1.2 SAV height statistics

The Table 7 shows descriptive statistics for the SAV height as function of depth for P01, P02, P03 and P04. The regions surrounding the upstream points (P03 and P04) in the river did not yield SAV height readings at 9-10 m depths. Overall, the data indicated a greater SAV development in deeper regions, such as at P01 and P02 compared to P03 and P04. The maximum SAV height observed at P01 region was greater (4.65m) followed by the P02 region (3.65m), while the maximum value for the P03 and P04 regions was approximately 2m. Boxplots for the SAV height variability relative to depth at each sample region are shown in Figure 22. Similar trends can be observed at P01 where the variability in SAV height (min, max, range, and average) was maximum followed by P02. The regions P03 and P04 had similar variability with overall SAV height below 2m. Moreover, SAV was observed at depths up to 10m at P01 and P02, 9m at P03 and 8m at P04.

Descriptive statistics for the submerged vegetation distribution (Table 7) with the suspended solid concentration at each point (Table 6) show that the largest mean SAV heights were at points P01 and P02, where the TSS values were lowest, and at greater depths than for points P03 and P04.

At the two points further downstream with TSS values at approximately 0.75 mg/l, the largest mean SAV height was 2.29 m in the 7-8 m depth range for P01 and 1.86 m in the 6-7 m depth range for P02.

At P03, where the TSS value was 1.3 mg/l, the largest mean SAV height value was 1.18 m between 3 and 4 meters deep, while at P04, where the TSS concentration value was greatest (1.71 mg/l), the greatest mean SAV height was 0.96 m in the 2-4 m depth range.

Table 7 – Descriptive statistics for the SAV heights at different depths and sampling stations. N is the number of readings acquired from the echosounder transects, Freq. is the frequency for N at each depth, SD is the standard deviation, Min, Median, and Max are the minimum, median, and maximum values for each dataset, and Q1 and Q3 are the first and third quartiles, respectively.

| | Depth (m) | N | Freq. | Mean (m) | SD (m) | Min (m) | Q1 (m) | Median (m) | Q3 (m) | Max (m) |
|---|---|---|---|---|---|---|---|---|---|---|
| **P01** | 0-1 | 5 | 0.5% | 0.10 | 0.11 | 0.00 | 0.00 | 0.11 | 0.19 | 0.26 |
| | 1-2 | 113 | 11.1% | 0.79 | 0.33 | 0.00 | 0.73 | 0.90 | 0.97 | 1.27 |
| | 2-3 | 144 | 14.2% | 1.40 | 0.28 | 0.85 | 1.17 | 1.43 | 1.57 | 2.13 |
| | 3-4 | 137 | 13.5% | 1.70 | 0.42 | 0.14 | 1.39 | 1.69 | 1.97 | 2.86 |
| | 4-5 | 142 | 14.0% | 1.98 | 0.49 | 1.02 | 1.61 | 1.96 | 2.29 | 3.37 |
| | 5-6 | 122 | 12.0% | 2.11 | 0.54 | 0.32 | 1.72 | 2.06 | 2.46 | 3.90 |
| | 6-7 | 108 | 10.7% | 2.15 | 0.91 | 0.19 | 1.77 | 2.18 | 2.59 | 4.46 |
| | 7-8 | 123 | 12.1% | 2.29 | 1.03 | 0.21 | 1.66 | 2.34 | 3.04 | 4.65 |
| | 8-9 | 89 | 8.8% | 1.24 | 0.81 | 0.19 | 0.56 | 1.09 | 1.80 | 3.91 |
| | 9-10 | 31 | 3.1% | 0.72 | 0.54 | 0.29 | 0.41 | 0.52 | 0.69 | 2.43 |
| **P02** | 0-1 | 1 | 0.0% | 0.00 | - | 0.00 | - | 0.00 | - | 0.00 |
| | 1-2 | 191 | 9.4% | 0.85 | 0.19 | 0.42 | 0.71 | 0.86 | 0.96 | 1.36 |
| | 2-3 | 347 | 17.0% | 1.27 | 0.33 | 0.58 | 1.01 | 1.23 | 1.47 | 2.25 |
| | 3-4 | 283 | 13.9% | 1.55 | 0.47 | 0.17 | 1.22 | 1.54 | 1.87 | 2.80 |
| | 4-5 | 216 | 10.6% | 1.74 | 0.58 | 0.23 | 1.46 | 1.71 | 1.95 | 3.46 |
| | 5-6 | 230 | 11.3% | 1.84 | 0.37 | 0.48 | 1.61 | 1.82 | 2.02 | 3.65 |
| | 6-7 | 214 | 10.5% | 1.86 | 0.44 | 0.20 | 1.68 | 1.93 | 2.14 | 2.70 |
| | 7-8 | 273 | 13.4% | 1.30 | 0.72 | 0.15 | 0.66 | 1.33 | 1.89 | 3.09 |
| | 8-9 | 201 | 9.9% | 0.49 | 0.31 | 0.20 | 0.32 | 0.39 | 0.58 | 2.51 |
| | 9-10 | 80 | 3.9% | 0.40 | 0.26 | 0.17 | 0.28 | 0.37 | 0.44 | 0.76 |
| **P03** | 0-1 | 8 | 0.6% | 0.07 | 0.06 | 0.00 | 0.00 | 0.11 | 0.13 | 0.13 |
| | 1-2 | 234 | 18.3% | 0.83 | 0.16 | 0.40 | 0.70 | 0.84 | 0.94 | 1.25 |
| | 2-3 | 241 | 18.8% | 1.09 | 0.18 | 0.25 | 1.01 | 1.09 | 1.20 | 1.53 |
| | 3-4 | 159 | 12.4% | 1.18 | 0.29 | 0.16 | 1.08 | 1.22 | 1.33 | 1.94 |
| | 4-5 | 148 | 11.5% | 1.12 | 0.41 | 0.21 | 0.94 | 1.20 | 1.41 | 1.86 |
| | 5-6 | 151 | 11.8% | 0.98 | 0.48 | 0.13 | 0.49 | 1.09 | 1.36 | 1.87 |
| | 6-7 | 212 | 16.5% | 0.56 | 0.38 | 0.17 | 0.28 | 0.37 | 0.79 | 1.76 |
| | 7-8 | 94 | 7.3% | 0.29 | 0.15 | 0.16 | 0.21 | 0.25 | 0.34 | 1.30 |
| | 8-9 | 35 | 2.7% | 0.33 | 0.21 | 0.17 | 0.20 | 0.24 | 0.37 | 1.04 |
| | 9-10 | - | - | - | - | - | - | - | - | - |
| **P04** | 0-1 | 11 | 1.2% | 0.12 | 0.13 | 0.00 | 0.00 | 0.11 | 0.24 | 0.36 |
| | 1-2 | 141 | 14.9% | 0.85 | 0.24 | 0.00 | 0.73 | 0.89 | 1.00 | 1.26 |
| | 2-3 | 200 | 21.1% | 0.96 | 0.19 | 0.35 | 0.84 | 0.96 | 1.07 | 1.44 |
| | 3-4 | 155 | 16.4% | 0.96 | 0.30 | 0.14 | 0.80 | 0.95 | 1.16 | 1.72 |
| | 4-5 | 163 | 17.2% | 0.73 | 0.41 | 0.13 | 0.36 | 0.67 | 1.02 | 1.75 |
| | 5-6 | 119 | 12.6% | 0.50 | 0.32 | 0.15 | 0.28 | 0.42 | 0.58 | 1.67 |
| | 6-7 | 95 | 10.0% | 0.35 | 0.23 | 0.16 | 0.24 | 0.29 | 0.33 | 1.45 |
| | 7-8 | 62 | 6.6% | 0.52 | 0.45 | 0.19 | 0.24 | 0.30 | 0.58 | 1.92 |
| | 8-9 | - | - | - | - | - | - | - | - | - |
| | 9-10 | - | - | - | - | - | - | - | - | - |

The data suggests that the total suspended solid concentration directly impacts the available underwater radiation and, consequently, SAV development and distribution (i.e., the level of available subaquatic energy decreases as the suspended solid concentration and mean SAV height increase; thus, more vegetation develops in shallower regions where radiation is sufficient).

Figure 22 – Boxplots for the SAV heights relative to the depths for P01 (a), P02 (b), P03 (c) and P04 (d).

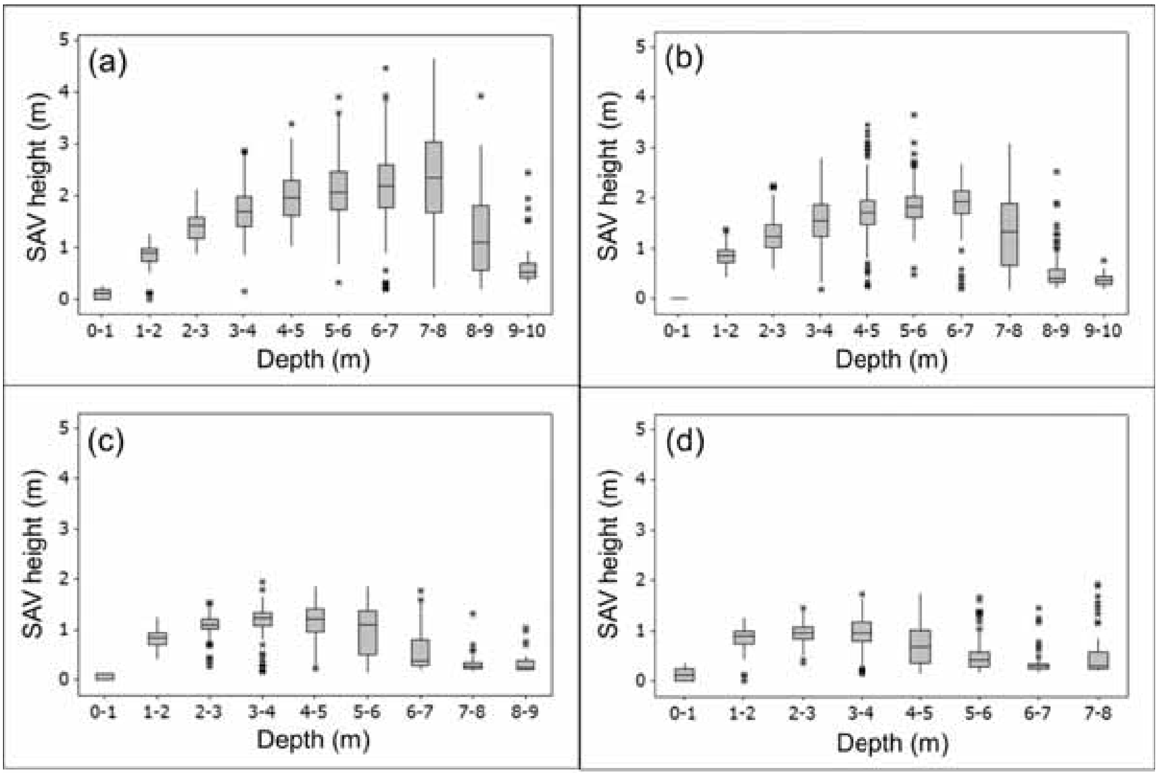


The greatest SAV height values in the P01 region were observed at depths between 6 and 8 m and extended up to 4.5 m. SAV was observed at depths up to slightly over 9.5 m. Furthermore, the boxplots in Figure 22 show that the SAV height varied most between 7 and 8 m deep. The greatest medium height was observed in the same depth range.

The P01 and P02 boxplots show the greatest SAV height variation between 7 and 8 m deep. Further, the greatest average SAV height was in the 7-8 m depth range for P01 and 6-7 m depth range for P02.

In P03, a small variability and continuous increase in SAV height was observed up to a 4 m depth. Between 4 and 6.5 m deep, the SAV heights varied greatly, which extended to almost 2 m. The greatest average and median heights were approximately 1 m and between 2 and 6 m deep.

### 5.1.3 Hyperspectral analysis

The hyperspectral downwelling irradiance ($E_d$) at different depths for the four sampling locations is shown in Figure 23. At each sampling location, readings were acquired just below the water surface (0-), and approximately at 1 m depth interval. Overall, $E_d$ values decreased across wavelengths as depth increased. The near-zero $E_d$ values and the saturation effect was noticed at deeper depths which provided insight to the optical depth of the reservoir. The integration $E_d$ between 400 and 700 nm (Photosynthetic Active Radiation - PAR) was calculated for each reading to obtain *$E_d$ PAR*. *$E_d$ PAR* exhibited the exponential decay of $E_d$ as described by Lambert-Beer's Law (Figure 24).

Figure 23 – Hyperspectral Ed vertical profile measurements at (a) P01, (b) P02, (c) P03, and (d) P04 after normalization.

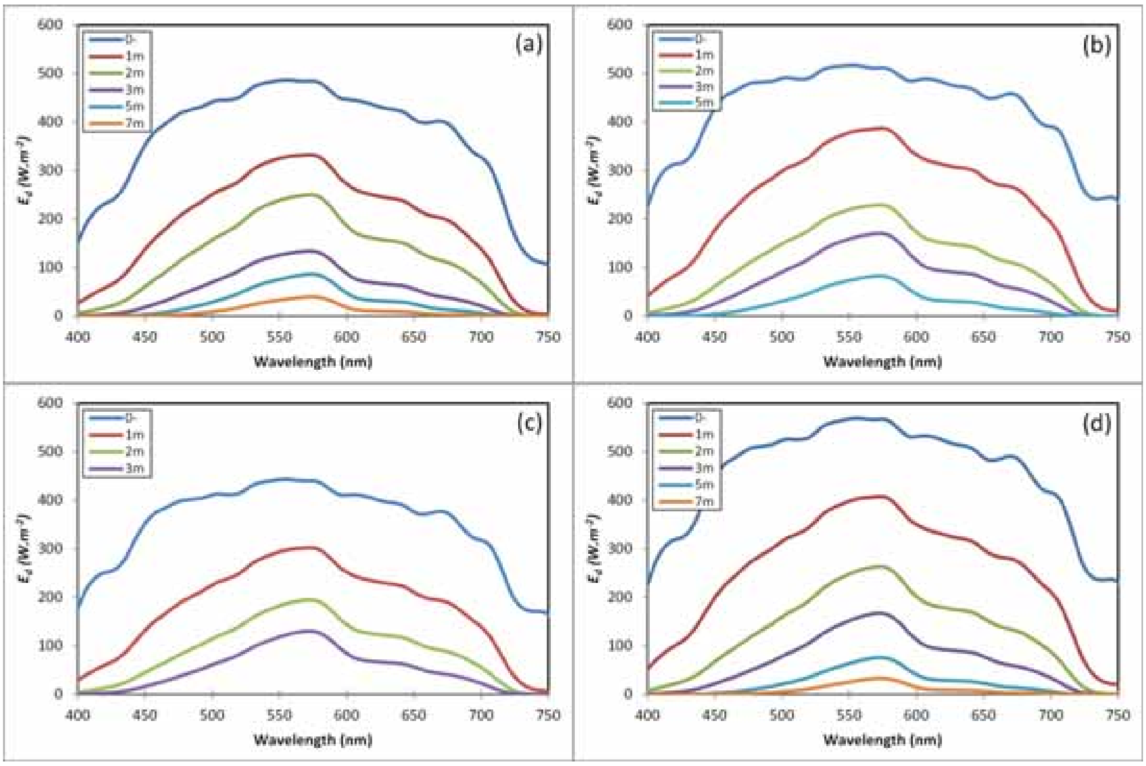

Figure 24 – Vertical attenuation of $E_d$ PAR as a function of depth at (a) P01, (b) P02, (c) P03, and (d) P04.

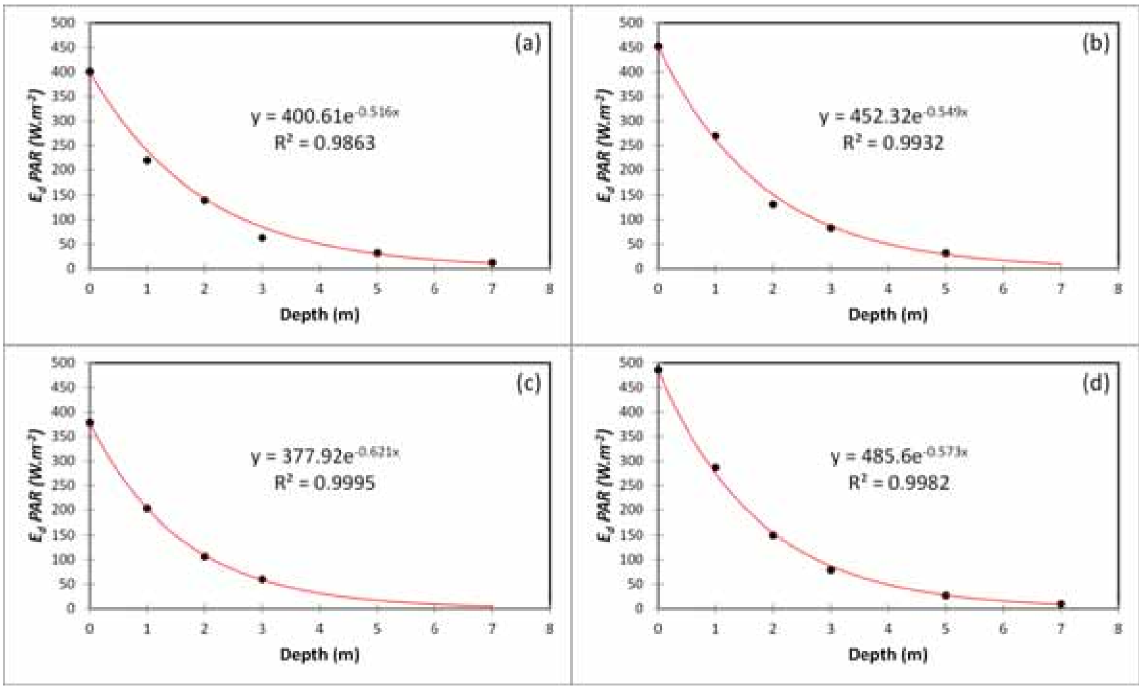


Equation (37) to Equation (40) represent vertical attenuation of $E_d$ *PAR* as a function of depth at sampling stations P01, P02, P03, and P04, respectively. The exponential relationships showed the determination coefficients ($R^2$) more than 0.98 for all stations. It was extracted the $K_d$ *PAR* from those equations.

$$E_d PAR(z) = 400.61e^{-\mathbf{0.516} \cdot Z} \tag{37}$$

$$E_d PAR(z) = 452.32e^{-\mathbf{0.549} \cdot Z} \tag{38}$$

$$E_d PAR(z) = 377.92e^{-\mathbf{0.621} \cdot Z} \tag{39}$$

$$E_d PAR(z) = 485.60e^{-\mathbf{0.573} \cdot Z} \tag{40}$$

The $K_d$ *PAR* values were used to calculate the euphotic zone depth by Equation (16). The $K_d$ *PAR* and euphotic zone depths ($Z_{EZ}$) are shown in Table 8.

Table 8 – Diffuse attenuation coefficient ($K_d$) of Photosynthetically Active Radiation (PAR) and the euphotic zone depth ($Z_{EZ}$) for each point.

| | $K_d$ **PAR** ($m^{-1}$) | $Z_{EZ}$ **(m)** |
|---|---|---|
| **P01** | 0.516 | 8.914729 |
| **P02** | 0.549 | 8.378871 |
| **P03** | 0.621 | 7.407407 |
| **P04** | 0.573 | 8.027923 |

The lowest diffuse attenuation coefficient was *Kd PAR* = 0.516 $m^{-1}$ at P01. This value indicates more transparent water in this region, which is consistent with its SAV behaviour (i.e., the vegetation developed better in this region).

SAV height against Percentage Light through Water (PLW) is plotted in Figure 25 and against Percentage Light at the Leaf (PLL) is the plotted in Figure 26. The Figure 27 shows the difference between PLW and PLL against SAV height. PLL and PLW are the optical parameters that act as a proxy to light attenuation in the water column and play an important role in SAV growth.

Figure 25 – SAV height distribution as function of Percentage Light through the Water (PLW).

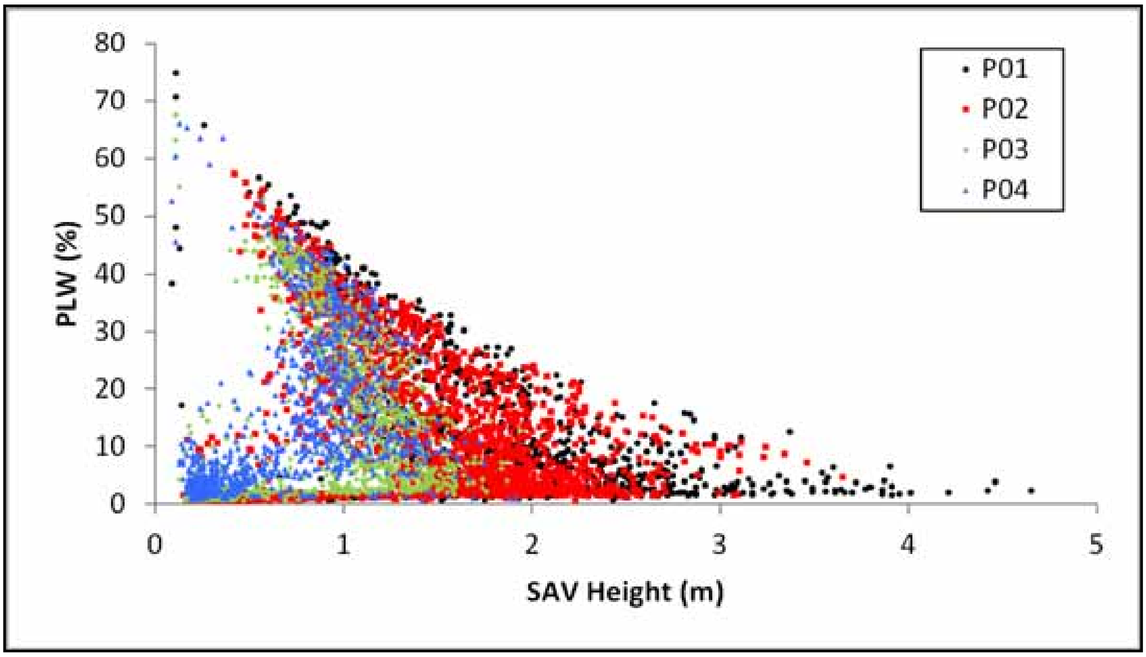

For sampling stations P01 and P02, where TSS is very low, a clear inverse relationship was observed between SAV height and PLW. At those stations SAV height increased as PLW decreased. That relationship was less prominent at stations P03 and P04 where TSS values were higher. It means that if increases PLW, light availability in the water column increases, so the SAV do not have to grow upward to receive as much light as possible. In the other hand, if decreases PLW, the submerged vegetation grows tall to get light required to their development. However, it is important to know that growing tall doesn't mean growing biomass, since plants grow more biomass when they have light enough. The same analysis can be done for PLL.

Figure 26 – SAV height distribution as function of Percentage Light at the Leaf (PLL).

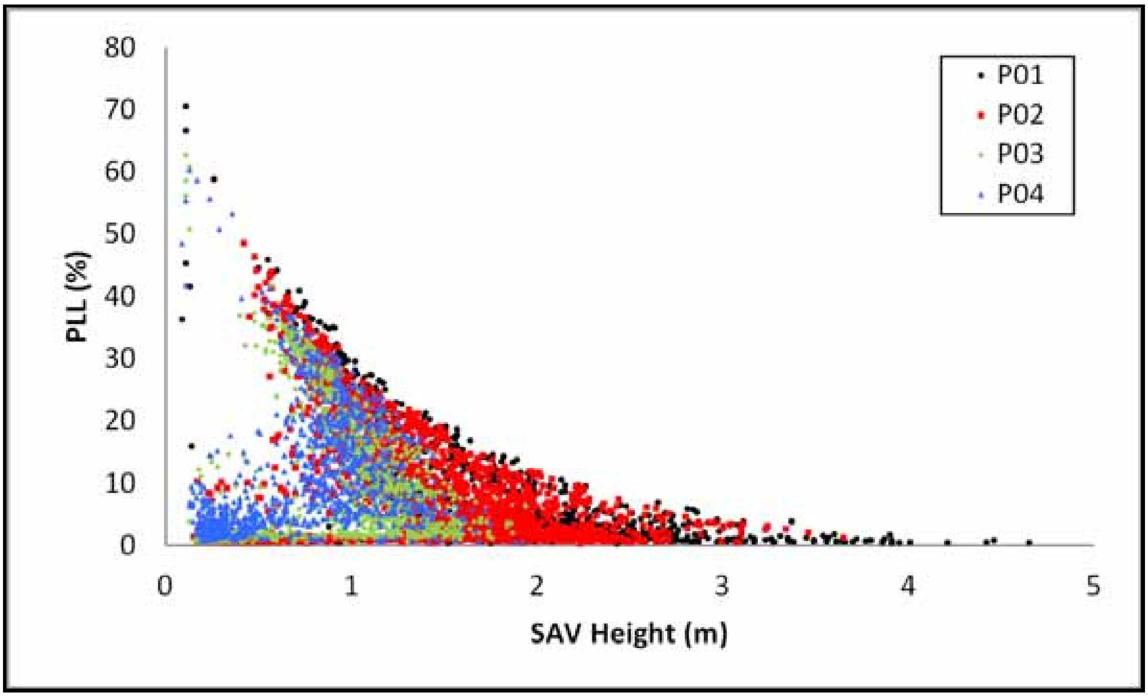


PLW subtracting PLL was done to obtain percentage values of radiation do not available for SAV, i.e. percentage of radiation attenuated by epiphytes. PLW-PLL against depth is shown in Figure 27 and against SAV height in Figure 28.

There is an exponential decrease of PLW-PLL with depth increasing. It means that in shallow regions the radiation is more attenuated by epiphytes than in deeper water. The maximum difference between PLW and PLL is 14% at very shallow depth. Regions deeper to 6 m, the difference (PLW – PLL) is not significant.

Figure 27 – Water body depth as function of the difference between Percent Light through the Water (PLW) and Percent Light at the Leaf (PLL).

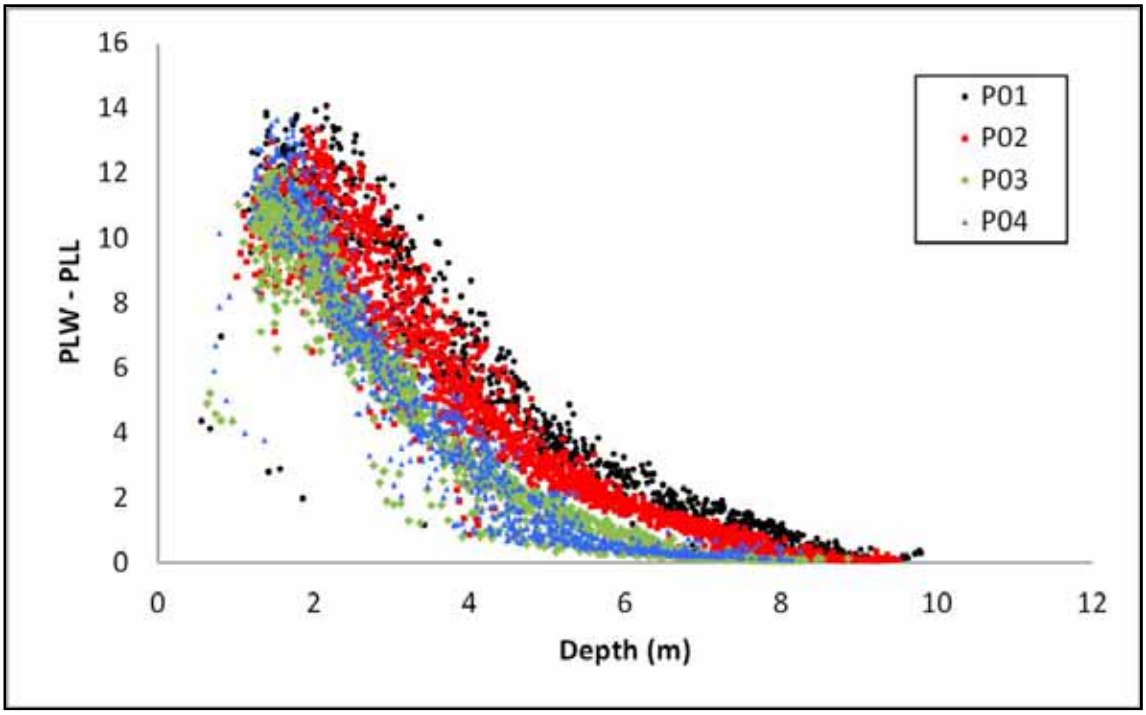


Figure 28 – SAV height as function of the difference between Percent Light through the Water (PLW) and Percent Light at the Leaf (PLL).

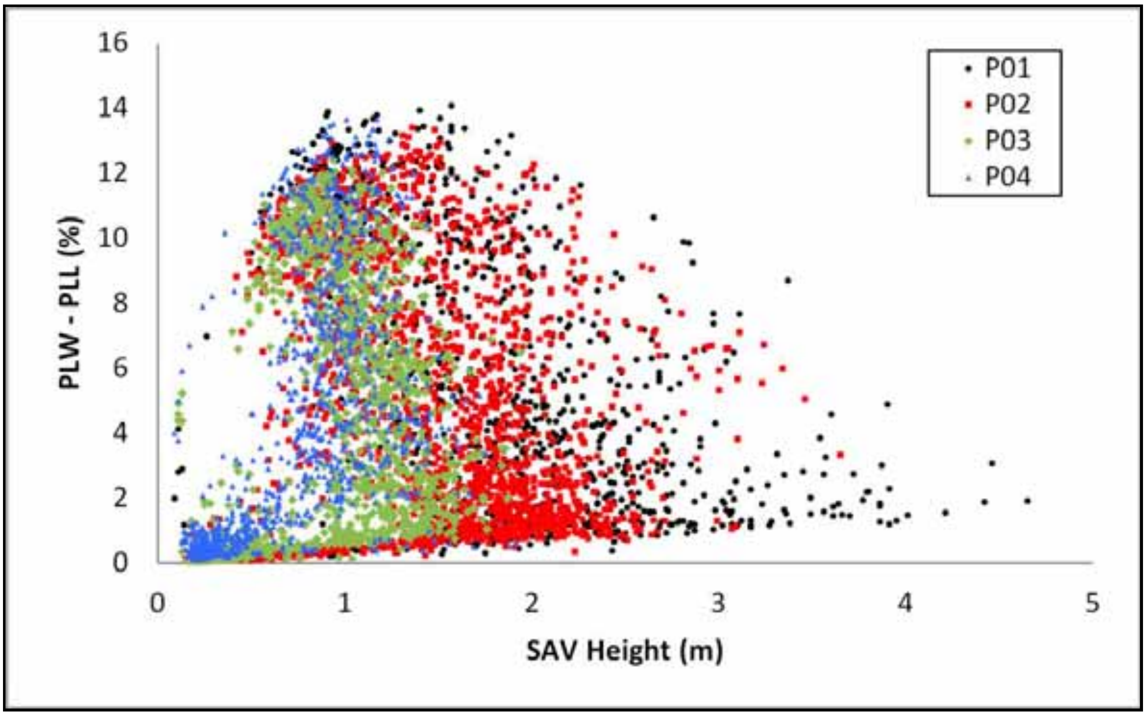

It is observed that the PLW-PLL relationship does not show a strong correlation with the SAV height, i.e., the percentage of radiation attenuated by epiphytes, apparently, does not make strong influence on the SAV development.

The Figure 29 shows a scatter plot of the SAV height distribution as function of depth for the four regions (represented by circles in Figure 7). Moreover, the dashed line illustrates the depth where $E_d$ reduces to 1% of the subsurface value (i.e., the euphotic zone limit).

Figure 29 – SAV height distribution as a function of depth. The dashed lines represent the euphotic zone limits (ZEZ) at each point.

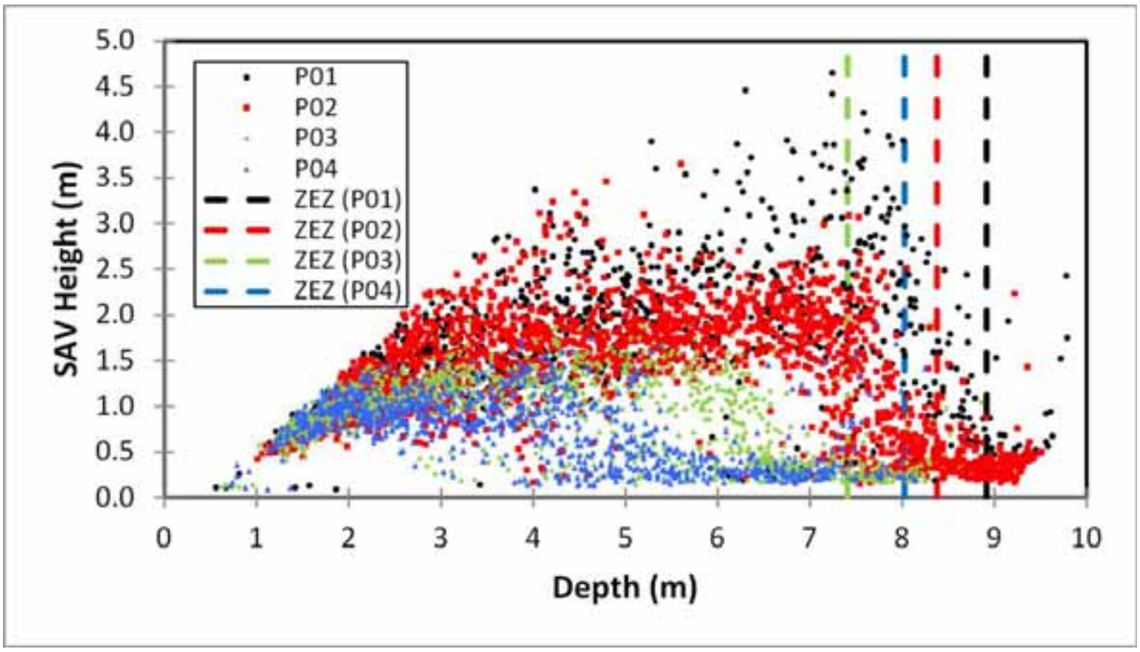


Analysing the submerged vegetation distribution in the P01 region it is showed a gradual increase in SAV maximum height as depth increased. This pattern was maintained through ~8 m deep, where the SAV height is rapidly decreased after the euphotic zone limit (i.e., where the downwelling irradiance corresponds to 1% of the subsurface downwelling irradiance). The same behaviour is seen for P02, where the euphotic zone's limit was 8.4 m and the SAV is dramatically reduced after that. A homogeneous SAV pattern with 2.5 m heights was observed at depths between 3 and 7 m for P02. Similar result was found for P01, but with some higher SAV in this range. This behaviour was also observed from the third quartile values for the aforementioned depths.

At P03, the greatest SAV heights were observed between 3 and 6 m deep. After 6.5 m deep, the mean SAV height rapidly decreased to values near 0.3 m and remains so until just after euphotic zone limit, 7.4 m.

At P04, the average SAV height remained at approximately 1 m for depths between 2 and 5 m; however, the SAV heights varied greatly between 4 and 5 m deep. For depths between 5 and 8 m, the average of SAV heights decreased to approximately 0.5 m. The occurrence of SAV in P04 was entirely interrupted after the euphotic zone limit (8 m).

It was observed that SAV height tends to increase with depth up to a certain limit depending on the region in the river. After that limit, the SAV height levels off for several meters of depth. When it reaches a critical depth in terms of radiation availability and water pressure, the SAV height rapidly decreases until it disappears. The euphotic zone limit was observed to be the boundary for significant SAV loss in each region. Greater SAV heights were observed at the Bonito River downstream (~ 4.7 m) at 7.6m deep. The maximum SAV height decreased from the downstream to the upstream river. High SAV observed at such deep areas indicate that the vegetation has a strong capacity to expand upward in the deeper areas to access sufficient light conditions required for photosynthesis. Figure 30 shows a picture of a 3 m long *Egeria sp.* pulled from the bottom. These high SAV at deeper areas are characterized by low biomass because of reduced photosynthesis rate caused by insufficient light conditions.

Figure 30 – Three meter long *Egeria sp*. acquired from the Nova Avanhandava Reservoir (SP, Brazil) in October 2012.

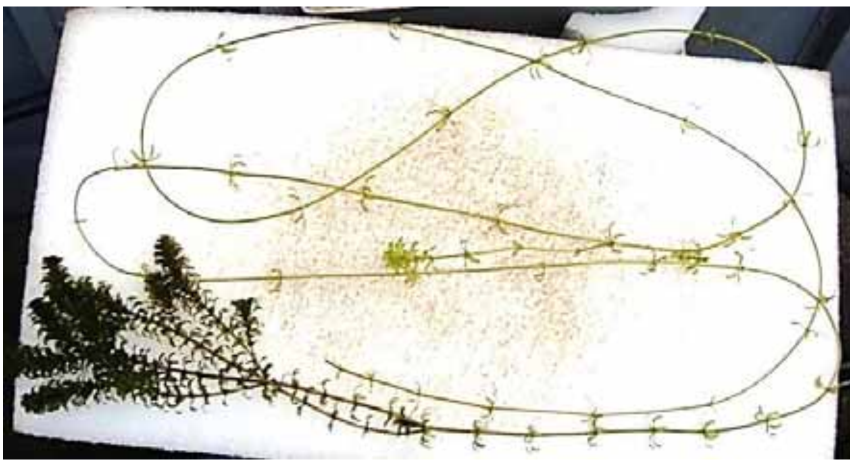

The SAV height distribution for the four regions is show in Figure 31. These maps were generated using geostatistical interpolation (Ordinary Krigging) of the SAV height data collected from numerous transects using the echosounder (Figure 7 – dotted red line).

Figure 31 – SAV height map for each region (P01, P02, P03 and P04).

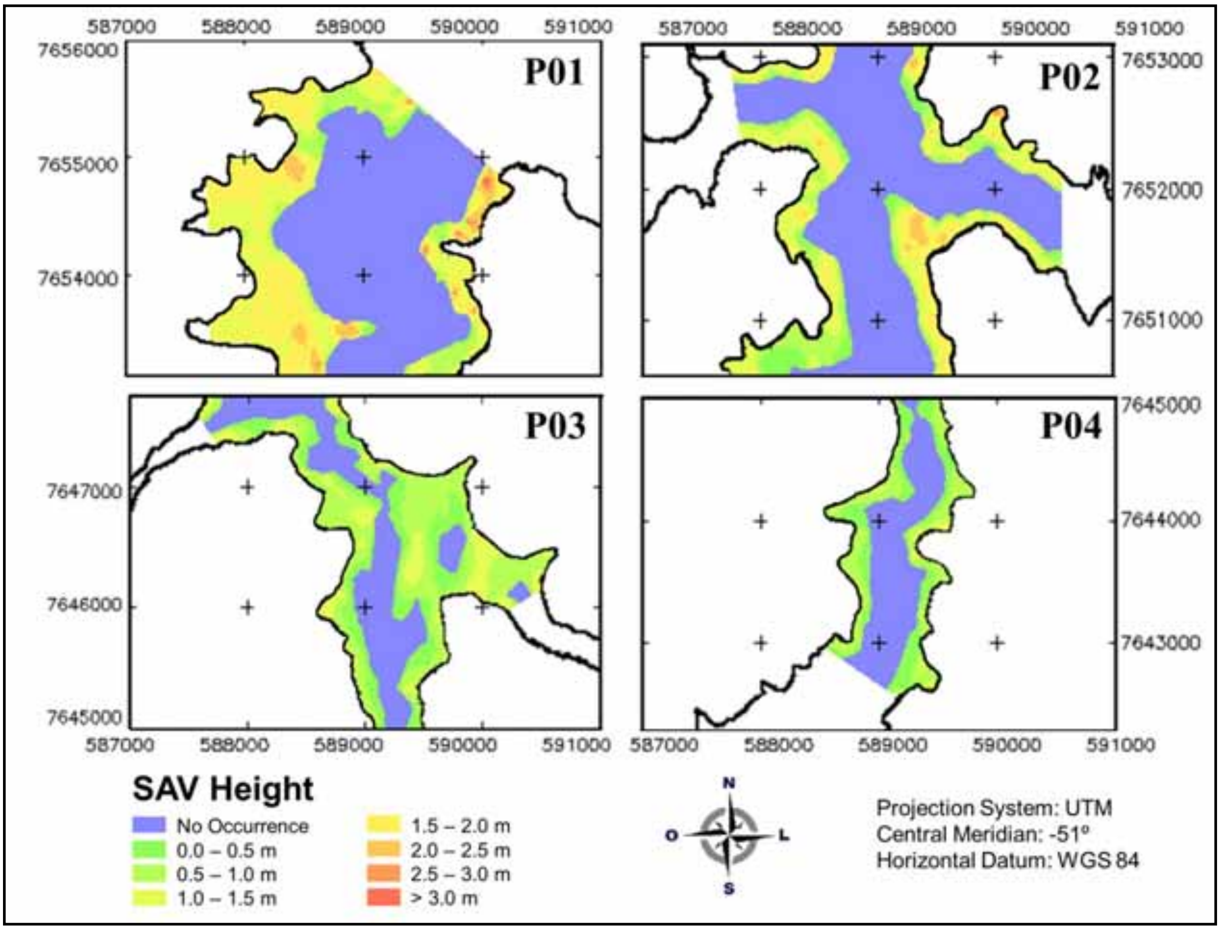


High SAV height values are seen at P01 with some areas where the height exceeded 3m. High SAV heights were also observed at P02, however, they were lower than P01. Most of the values at P03 and P04 were close 1 m on average with the maximum below 2 meter as previously observed. The mean SAV height shows a decreasing trend with upstream direction.

### 5.2 Bio-optical models for estimation of SAV height

This section is related to the following objective: To retrieve the bottom response and generate bio-optical models to estimate the height and the position of submerged aquatic vegetation in the Nova Avanhandava reservoir. The results in this section are based on the second field campaign data.

#### 5.2.1 Diffuse attenuation coefficients

Figure 32 shows the $K_d$ and $K_{Lu}$ derived from downwelling irradiance ($E_d$) and upwelling radiance ($L_u$), respectively. The wavelengths used in methodology were green band (~550 nm) and red band (~650 nm). So, the significant difference among the attenuation coefficients ($K_d$ and $K_{Lu}$) results, observed in the blue region (~450 nm), does not matter for the procedure. A greater discrepancy in the P09 was observed for $K_{Lu}$, however, this difference was corrected using the average.

Figure 32 – The $K_d$ (a) and $K_{Lu}$ (b) derived from downwelling irradiance ($E_d$) and upwelling radiance ($L_u$), respectively. Dashed line represents the average value.

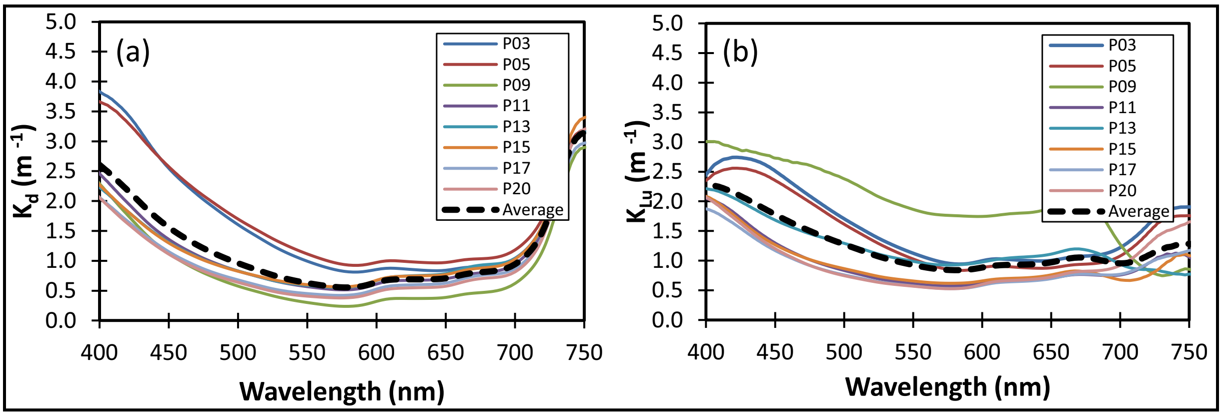


The $K_d$ was also calculated using the methodology proposed by Palandro et al. (2008). This $K_d$ was named as $K_d{}^P$. The $K_d{}^P$ was derived as the slope of linear regression between depth and *ln* $R_{rs}$ (Figure 33).

Figure 33 – Regression to obtain $K_d$ (Green) and $K_d$ (Red) based in green and red bandwidth according to Palandro et al. (2008).

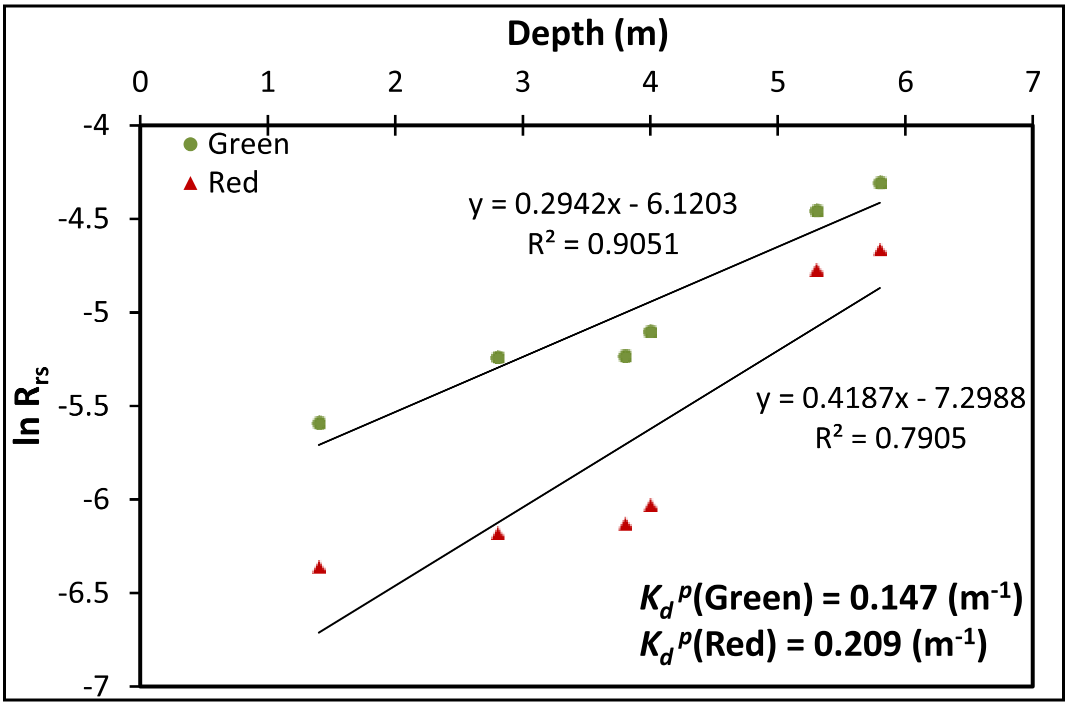


The diffuse attenuation coefficient based on Palandro et al. (2008) ($K_d{}^p$) obtained lower values than $K_d$ based on field data downwelling irradiance ($E_d$) (Figure 32). However, $K_d{}^p$ was used to test its behavior in the models to retrieve the bottom reflectance.

### 5.2.2 Remote sensing reflectance

Based on upwelling radiance just below the surface ($L_u(0\text{-})$) and the downwelling irradiance on the boat ($E_s$) we calculated the $R_{rs}$ (Remote sensing reflectance) using the Equation (17). The results of $R_{rs}$ for each sample point are shown in Figure 34.

Figure 34 – Remote sensing reflectance in the sample points.

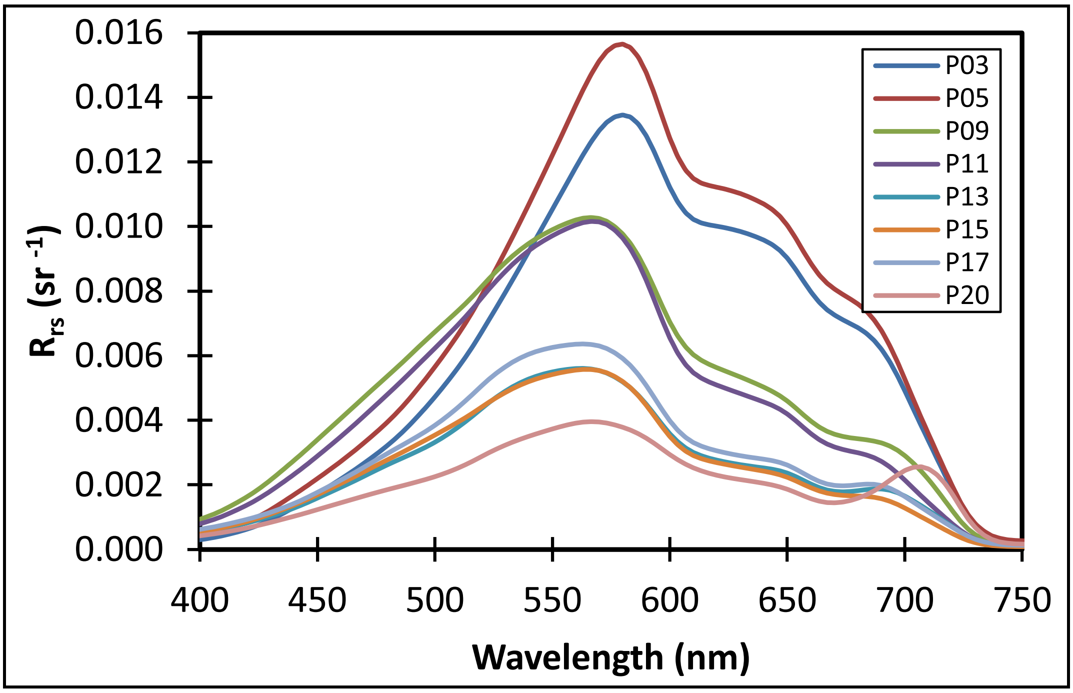


A decrease in the magnitude of the spectral curves is observed from upstream points to downstream points, i.e., to P03 to P20. This behavior is strongly correlated with the TSS concentration, which has the highest values in the upstream region of the river.

Further, in P20 it is observed a reflectance peak at 700 nm. That occurs because it is a point with very shallow water (1.4 m, Table 2) and dense presence of submerged vegetation. Thus, in this spectral region, the radiation is not completely absorbed by water column; it is reflected by the bottom and returns to water surface.

#### 5.2.2.1 Satellite bands simulation

OLI/Landsat 8 (Figure 35 (a)) and SPOT 6 (Figure 35 (b)) bands were simulated based on $R_{rs}$ (Figure 34) and their relative spectral response (Figure 21). We can see both SPOT bands and OLI bands present similar shapes.

Figure 35 – Simulated bands of OLI/Landsat 8 bands in (a) and SPOT 6 in (b) using remote sensing reflectance of in situ data.

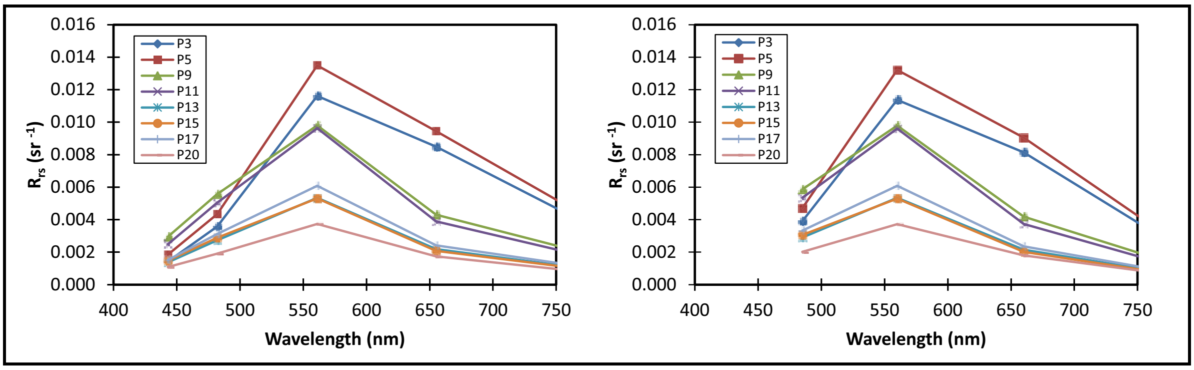


### 5.2.3 Atmospheric correction of satellite data

The Figure 36 is the regression between the remote sensing reflectance ($R_{rs}$) calculated from field data and the Digital Number (DN) collected from satellite image (SPOT-6). The regressions were calculated for green and red bands. Equations (41) and (42) present the linear regressions from Figure 36 for Green band and Red band, respectively.

Figure 36 – Regression between $R_{rs}$ (Field data) and Digital Number (SPOT-6 image) for green and red bands.

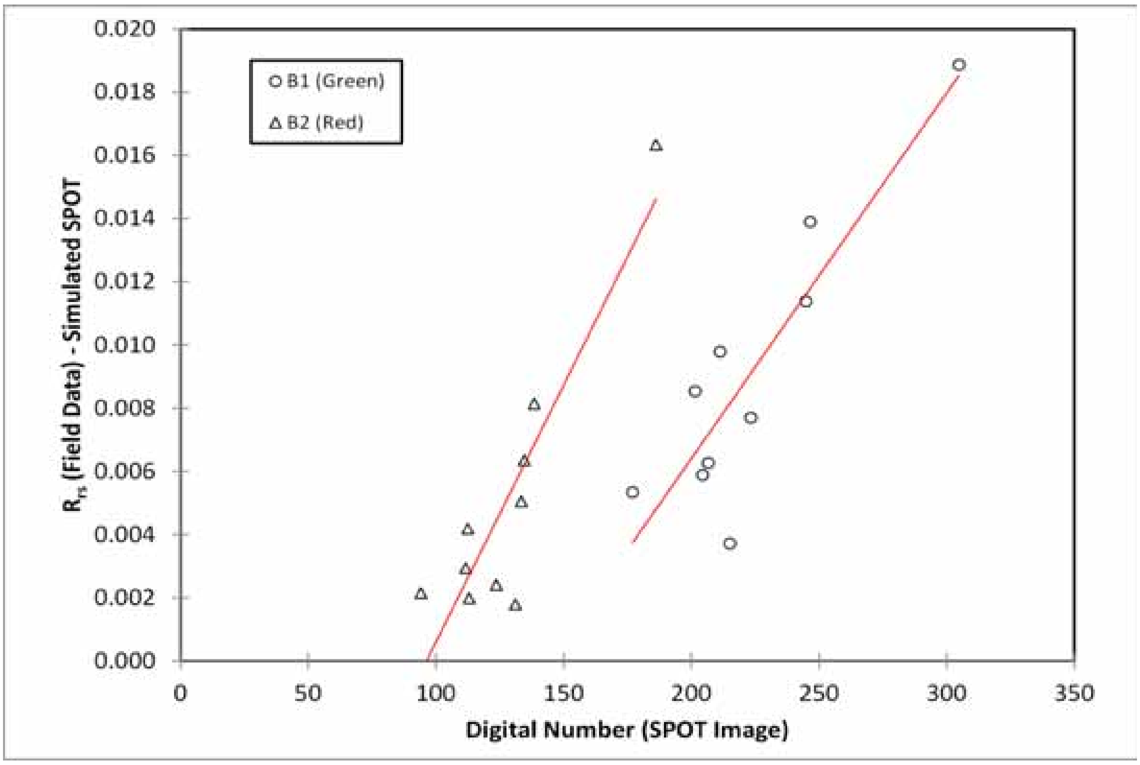

$$B1_{Green}[R_{rs}] = 0.000116 * B1_{Green}[DN] - 0.01672 \quad (41)$$

$$B2_{Red}[R_{rs}] = 0.000163 * B2_{Red}[DN] - 0.01568 \quad (42)$$

The atmospheric correction for SPOT-6 green band and red band was done by *Empirical Line Method* using the Equations (41) and (42), respectively. The coefficient of determination ($R^2$) of Equation (41) is 79.3% and Equation (42) is 81.0%.

### 5.2.4 Retrieved bottom reflectance

The retrieved bottom reflectance represents the reflectance of the benthic habitat after removing the influence of the water column. The bottom reflectance was retrieved using Palandro et al. (2008) model (Equation (25), **PAL08**) and average $K_d$ in Figure 37 (a) and specific $K_d$ in Figure 37 (c) (i.e., it was used a specific $K_d$ for each point). Bottom reflectance was retrieved using Dierssen et al. (2003) model (Equation (26), **DIE03**) and average $K_d$ and $K_{Lu}$ in Figure 37 (b) and specific $K_d$ and $K_{Lu}$ in Figure 37 (d). Bottom reflectance retrieved by **PAL08** model show values close to zero before 400 and after 730 nm. The opposite was observed at bottom reflectance retrieved by **DIE03** model that show very high values for wavelengths before 400 and after 730 nm.

Figure 37 – Remote sensing reflectance of the bottom retrieved by **PAL08** model in (a) and (c) and irradiance reflectance of the bottom retrieved by **DIE03** model in (b) and (d). Average $K_d$ and $K_{Lu}$ derived from in situ data were used in (a) and (b) and a specific $K_d$ and $K_{Lu}$ for each point were used in (c) and (d).

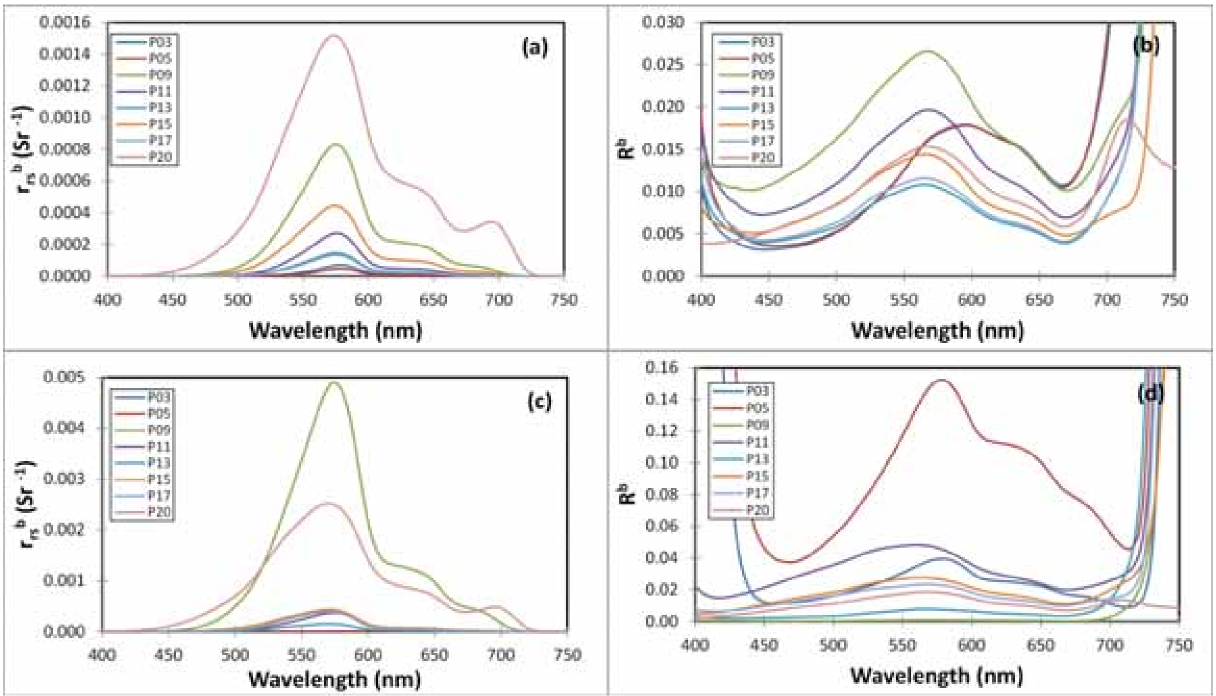


It is possible to see a significant difference between the spectral curves obtained by (i) average $K_d$ and $K_{Lu}$ derived from in situ data (Figure 37 (a) and (b)) and (ii) specific $K_d$ and $K_{Lu}$ for each point (Figure 37 (c) and (d)). This may indicate an expressive change on models for estimation of SAV height, depending the bottom reflectance chosen, i.e. average or specific $K_d$ and $K_{Lu}$

Figure 38 presents the retrieved bottom response using the remote sensing reflectance simulated for the OLI/Landsat sensor in (a) and (b) and for the SPOT-6 sensor in (d) and (e). (a) and (c) shows the retrieved bottom by **PAL08** model and (b) and (d) the retrieved bottom by **DIE03** model. All graphs used the average $K_d$ and $K_{Lu}$ which were collected in the field.

Figure 38 – Remote sensing reflectance of the bottom retrieved by **PAL08** model in (a) and (c) and irradiance reflectance of the bottom retrieved by **DIE03** model in (b) and (d). Average $K_d$ and $K_{Lu}$ derived from in situ data were used on Landsat 8 simulated in (a) and (b) and on SPOT 6 simulated in (c) and (d).

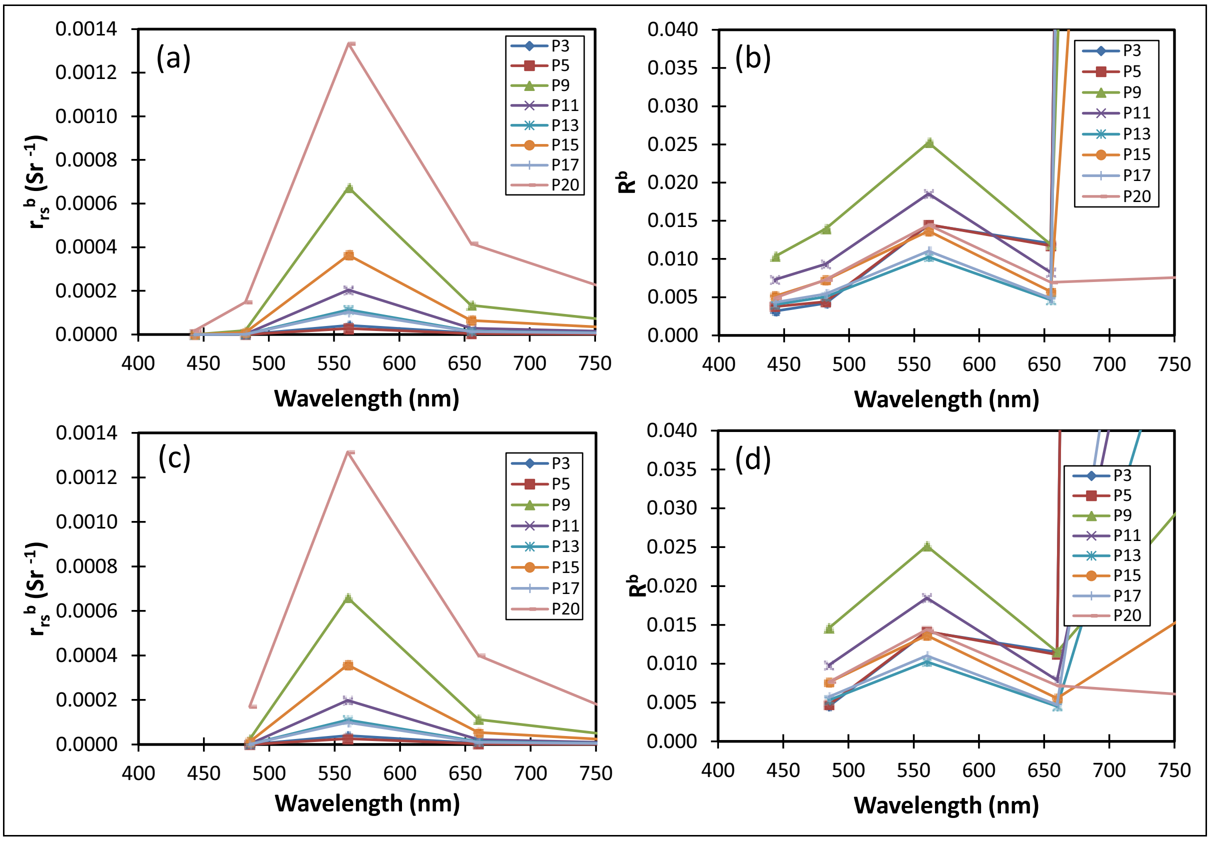


The green and red bands, simulated for the OLI/Landsat and SPOT-6, was also used to retrieve the bottom by **PAL08** and **DIE03** models, using the $K_d{}^{p}$. This bottom retrieval results are presented in Figure 39.

Figure 39 – Remote sensing reflectance of the bottom retrieved by **PAL08** model in (a) and (c) and irradiance reflectance of the bottom retrieved by **DIE03** model in (b) and (d). Average $K_{Lu}$ derived from in situ data and $K_d^p$ were used on Landsat 8 simulated in (a) and (b) and on SPOT 6 simulated in (c) and (d).

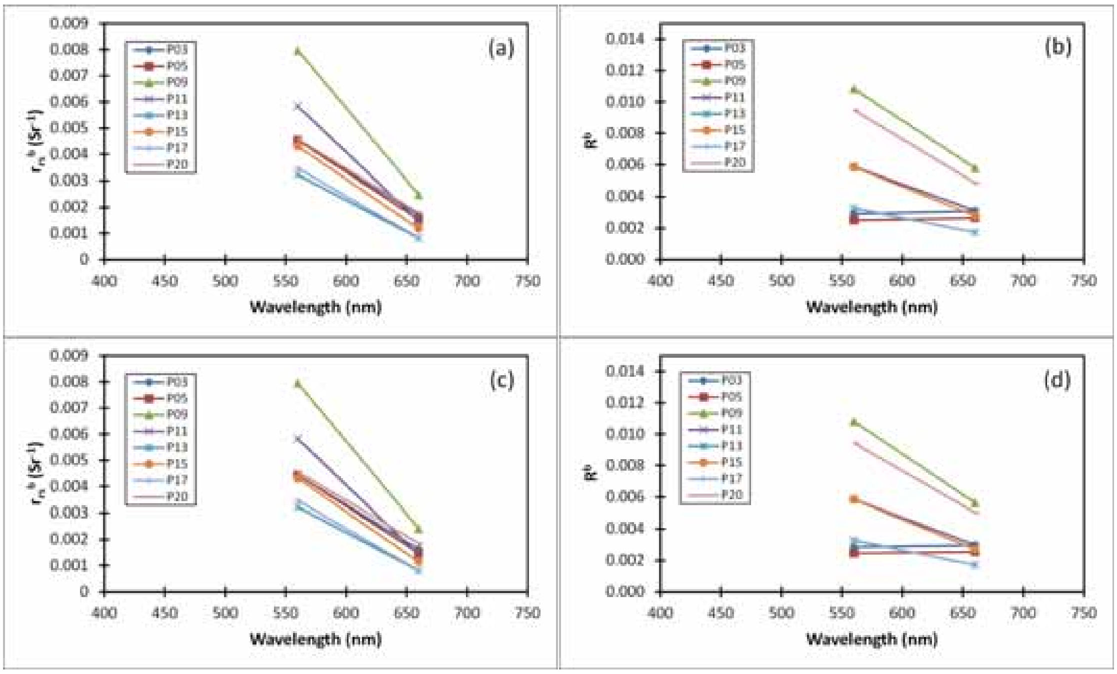


The bottom reflectance based on simulated bands of OLI/Landsat 8 and SPOT-6 exhibited values almost identical. These results happened due to the similarity between the Landsat 8 and SPOT-6 bands in visible and NIR range.

### 5.2.5 SAV models based on in situ data

Reflectance of in situ data were used to retrieve the bottom using **PAL08** and **DIE03** models. Models were calibrated for the estimation of SAV height. Figure 40 shows the calibrated models based on GRVI (Equation (27)) and Figure 41 shows the calibrated models based on Slope (Equation (28)), both using the bottom retrieved by **PAL08**. Figure 42 shows the calibrated models based on GRVI and Figure 43 shows the calibrated models based on Slope, both using the bottom retrieved by **DIE03**.

Due to the limited sampling points for models calibration, the SPOT-6 image was used as an additional data for validation. Therefore, only the models that used the SPOT-6 simulated bands (Figure 40 (e) and (f); Figure 41 (e) and (f); Figure 42

(e) and (f); and Figure 43 (e) and (f)) were validated for regressions based on in situ data.

Figure 40 – Regression between SAV height and GRVI based on remote sensing reflectance of the bottom retrieved by **PAL08**. Hyperspectral data: Average $K_d$ derived from in situ data in (a) and a specific $K_d$ for each point in (b); Landsat 8 simulated: Average $K_d$ derived from in situ data in (c) and using $K_d{}^p$ in (d); SPOT 6 simulated: Average $K_d$ derived from in situ data in (e) and using $K_d{}^p$ in (f). Validation for models (e) and (f) are presented in (g) and (h), respectively.

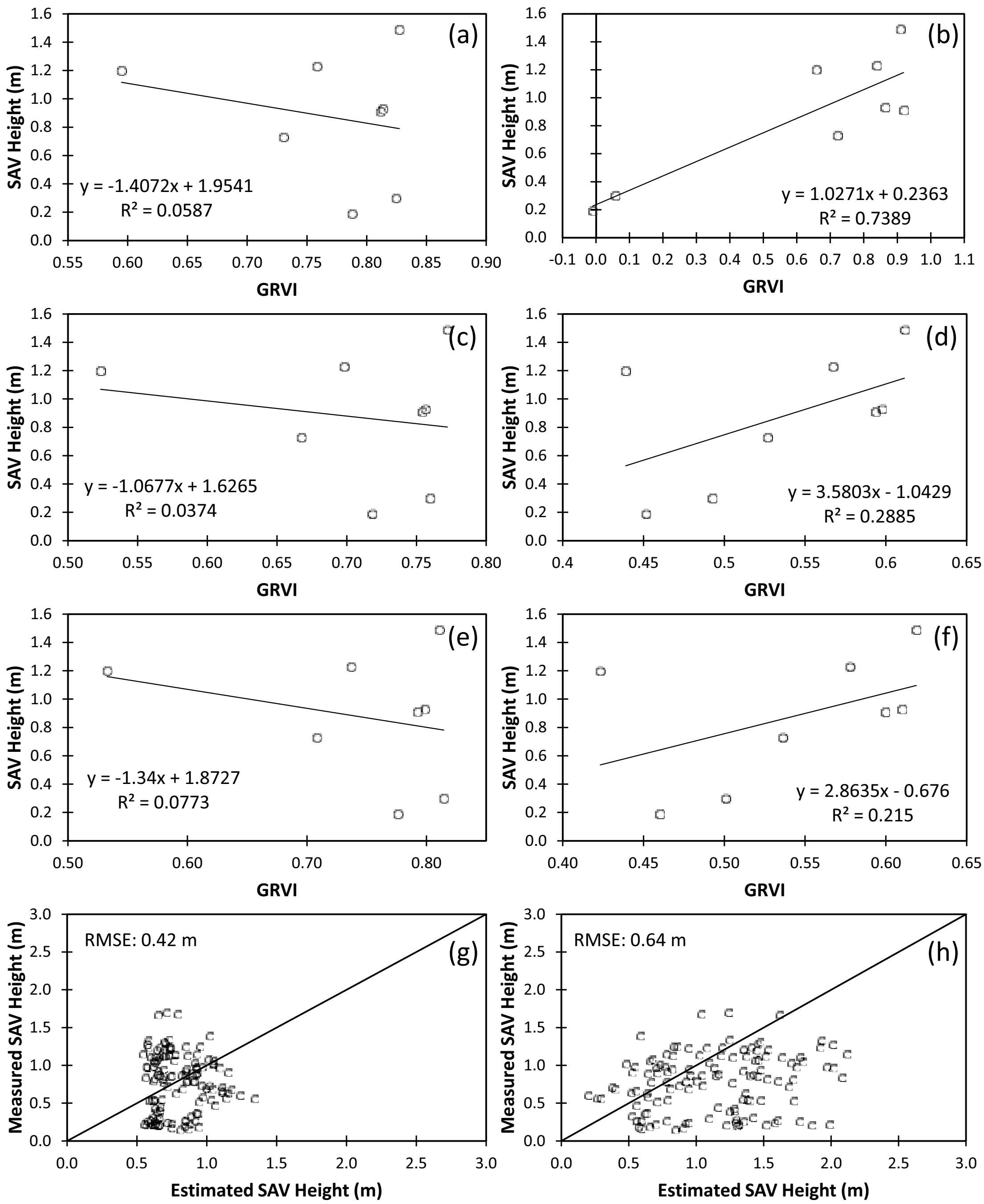

Figure 41 – Regression between SAV height and Slope based on remote sensing reflectance of the bottom retrieved by **PAL08**. Hyperspectral data: Average $K_d$ derived from in situ data in (a) and a specific $K_d$ for each point in (b); Landsat 8 simulated: Average $K_d$ derived from in situ data in (c) and using $K_d{}^p$ in (d); SPOT 6 simulated: Average $K_d$ derived from in situ data in (e) and using $K_d{}^p$ in (f). Validation for models (e) and (f) are presented in (g) and (h), respectively.

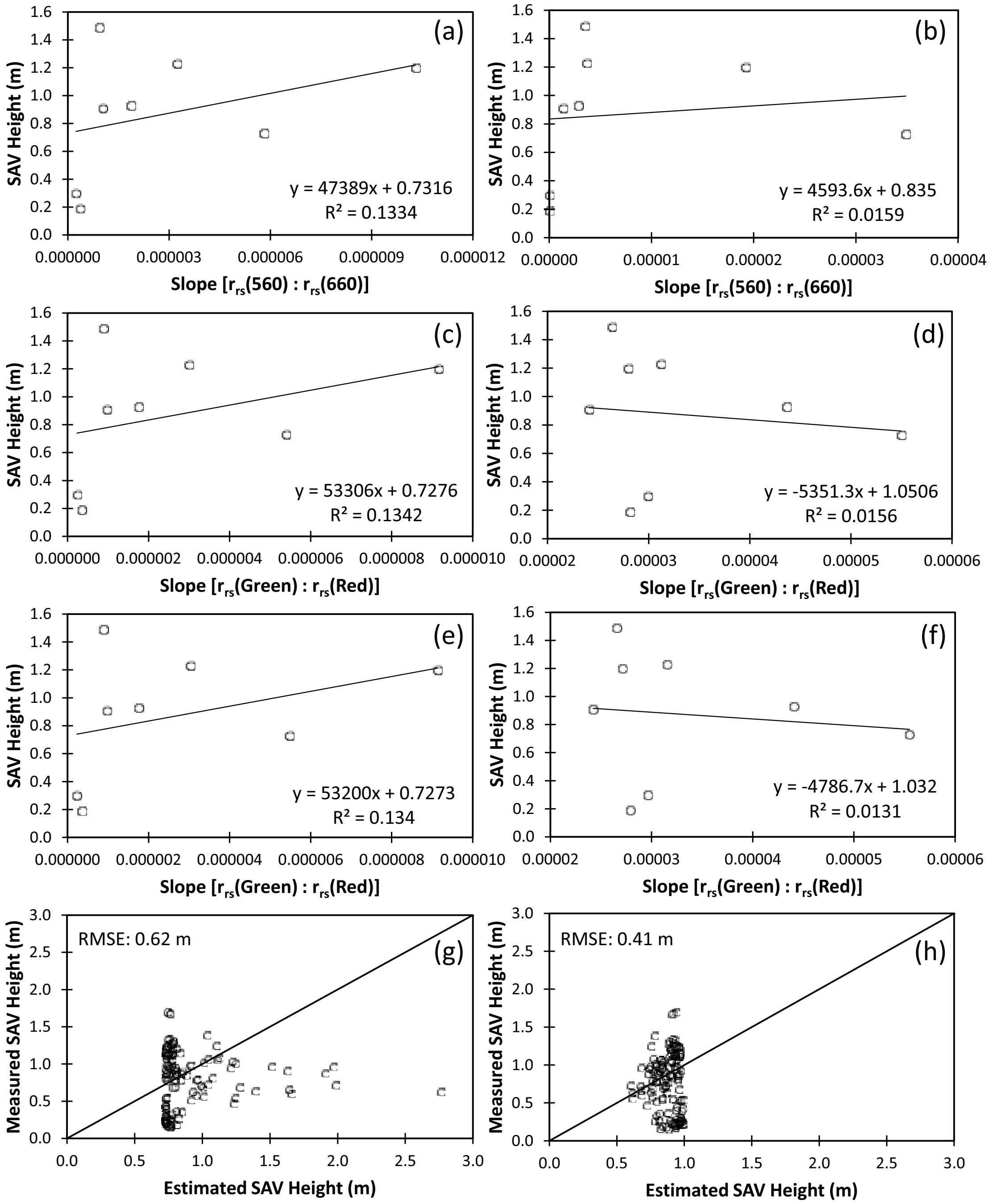

Figure 42 – Regression between SAV height and GRVI based on irradiance reflectance of the bottom by **DIE03**. Hyperspectral data: Average $K_d$ and $K_{Lu}$ derived from in situ data in (a) and specific $K_d$ and $K_{Lu}$ for each point in (b); Landsat 8 simulated: Average $K_d$ and $K_{Lu}$ derived from in situ data in (c) and using $K_d{}^p$ in (d); SPOT 6 simulated: Average $K_d$ and $K_{Lu}$ derived from in situ data in (e) and using $K_d{}^p$ in (f). Validation for models (e) and (f) are presented in (g) and (h), respectively.

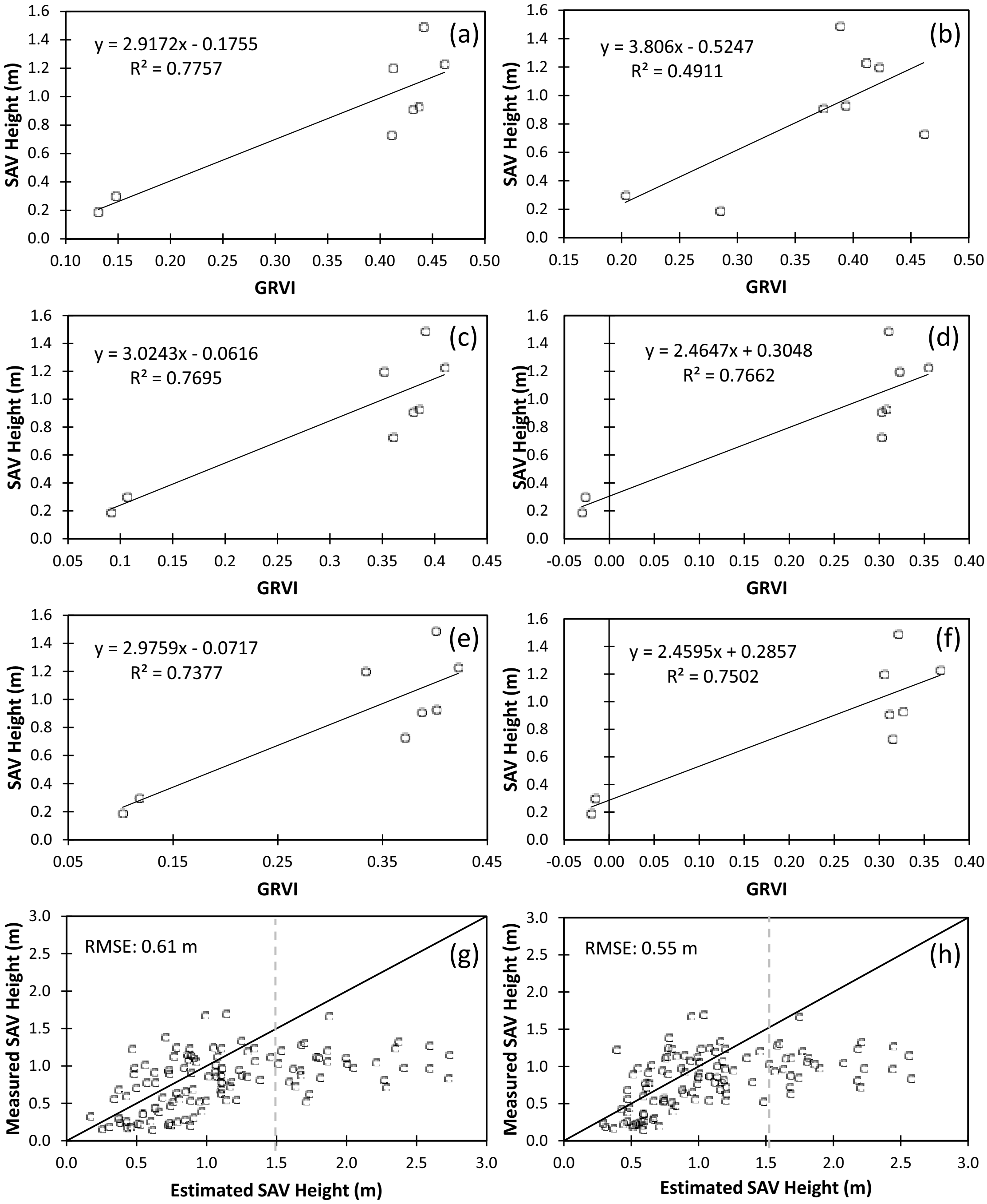

Figure 43 – Regression between SAV height and Slope [$R^b$(Green) : $R^b$(Red)] based on irradiance reflectance of the bottom by **DIE03**. Hyperspectral data: Average $K_d$ and $K_{Lu}$ derived from in situ data in (a) and specific $K_d$ and $K_{Lu}$ for each point in (b); Landsat 8 simulated: Average $K_d$ and $K_{Lu}$ derived from in situ data in (c) and using $K_d{}^p$ in (d); SPOT 6 simulated: Average $K_d$ and $K_{Lu}$ derived from in situ data in (e) and using $K_d{}^p$ in (f). Validation for models (e) and (f) are presented in (g) and (h), respectively.

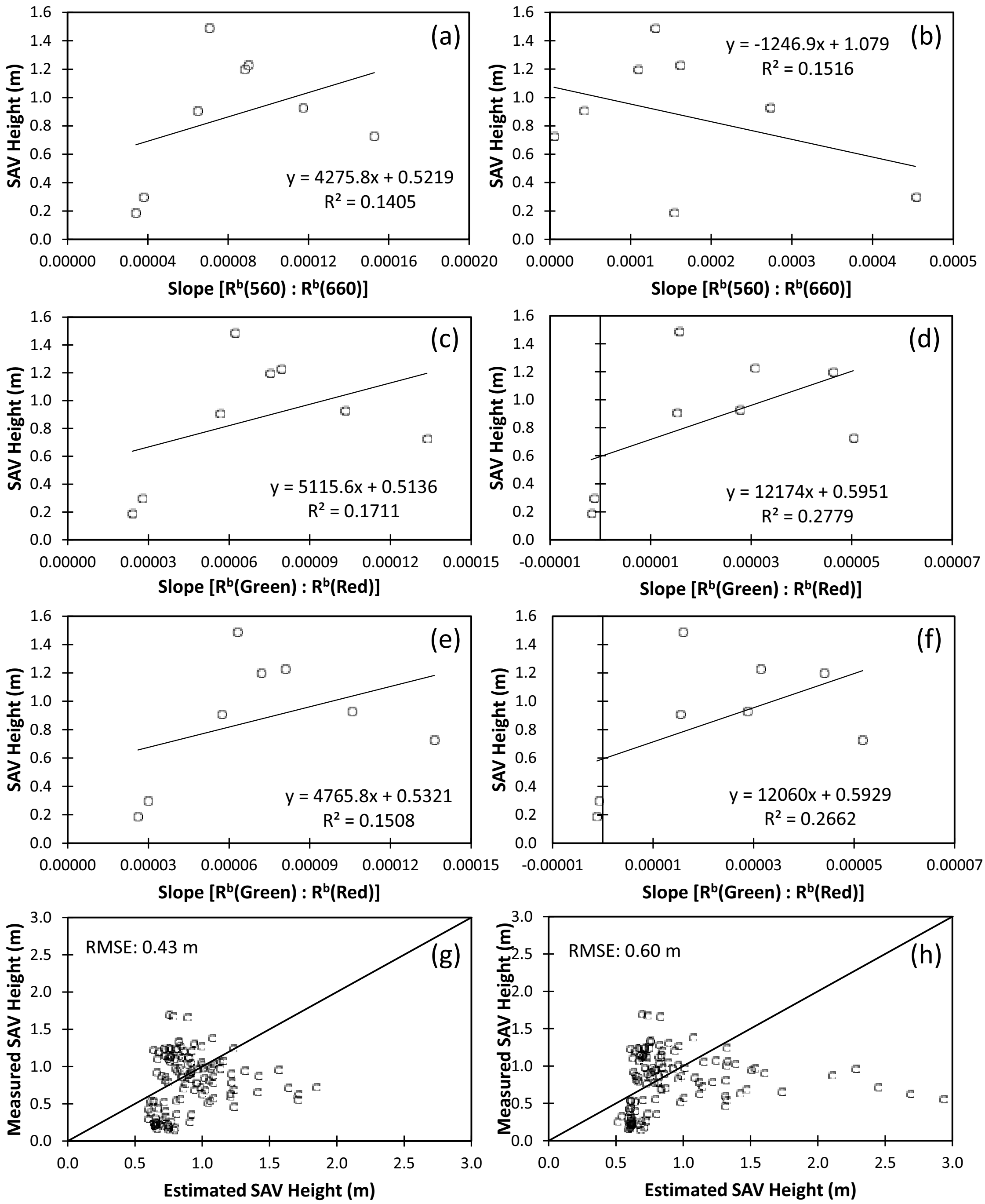

It is observed that the models obtained by the bottom retrieved by Palandro et al (2008) (Figure 40 and Figure 41) did not obtain a good fitting. The only model that showed an acceptable adjustment ($R^2$ = 0.74) was using GRVI (Use of wavelengths 560 nm and 660 nm, width of 1 nm) and attenuation coefficients ($K_d$) specific to each point. All other models had a $R^2$ lower than 0.3. Thus, it can be concluded that the methodology proposed by Palandro et al. (2008) to retrieve the bottom was not satisfactory for the study area when using in situ data.

The models obtained by the bottom, which was retrieved by **DIE03** did not present good fitting when the Slope was used (Figure 43; $R^2$ lower than 0.3). However, the usage of GRVI for the models calibration (Figure 42) presented mainly satisfactory results, with $R^2$ higher than 0.7. The calibrated models validation through the simulated SPOT-6 image presented RMSE = 0.61m for $K_d$ and RMSE = 0.55m for $K_d{}^p$. Furthermore, it is observed that there is an overvaluation of the SAV on values higher than 1.5 m. Thus, it was chosen to calibrate the models (Figure 42 (e)) through the logarithmic fitting to correct the overvaluation. It was not possible to use the *ln* function in the model in (Figure 42 (f)) due to the presence of negative values. The Figure 44 shows a calibration and validation using the *ln* in the model of Figure 42 (e).

Figure 44 – Regression between SAV height and GRVI of SPOT simulated based on irradiance reflectance of the bottom by **DIE03** and average $K_d$ and $K_{Lu}$ derived from in situ data.

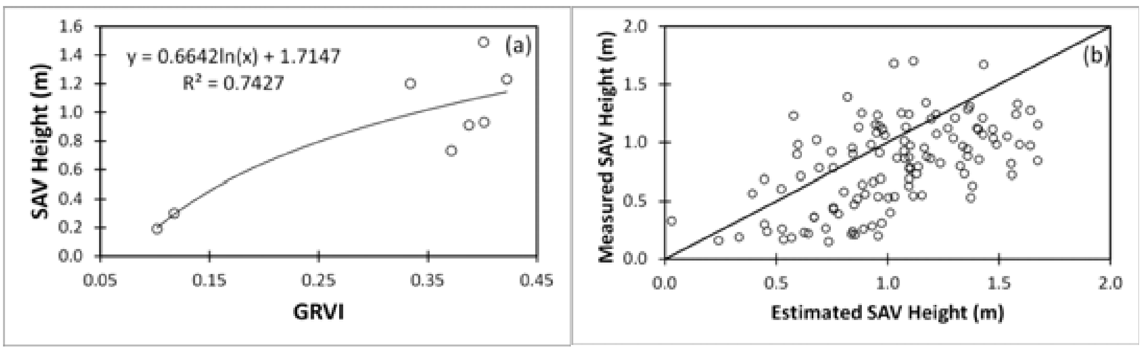


Using this model, there was a reduction of the RMSE from 0.61 to 0.40. Furthermore, the overvaluation of the SAV height values higher than 1.5 m was corrected. Therefore, this model (Figure 44) was considered the best one for estimate the SAV height based on field data.

### 5.2.6 SAV models based on satellite data

The SPOT-6 image was used to retrieve the bottom through **PAL08** and **DIE03**. Twenty points along the study area were chosen. Figure 45 show the calibrated models for SAV height estimation through GRVI (Equation (27)) and Figure 46 using the Slope (Equation (28)).

Figure 45 – Regression between SAV height and GRVI based on remote sensing reflectance of the bottom by **PAL08** in (a) and (b) and based on irradiance reflectance of the bottom by **DIE03** in (e) and (f). Average $K_d$ and $K_{Lu}$ derived from in situ data were used in (a) and (e); $K_d{}^p$ was used in (b) and (f). (j) and (l). The validation for each model is under itself. Validation for models (a), (b), (e) and (f) are presented in (c), (d), (g) and (h), respectively.

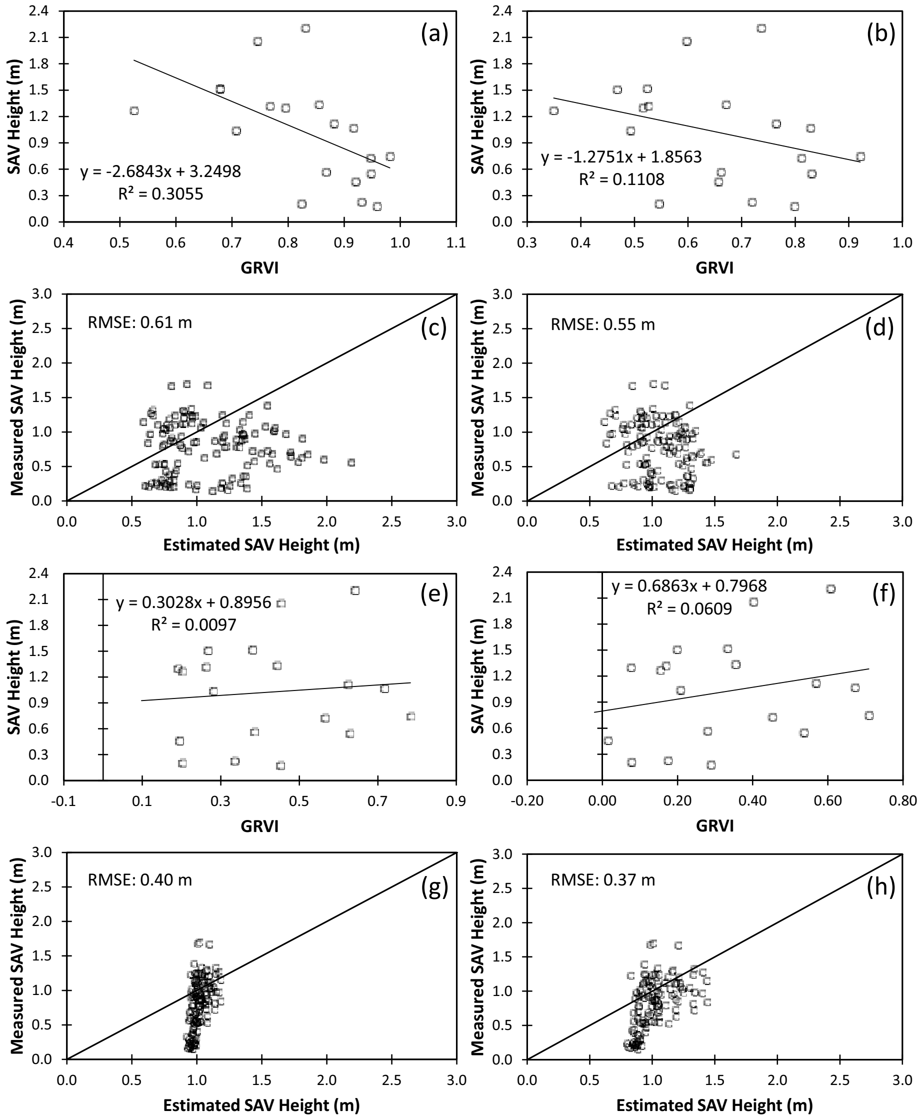

Figure 46 – Regression between SAV height and Slope [(Green):(Red)] based on remote sensing reflectance of the bottom by **PAL08** in (a) and (b) and based on irradiance reflectance of the bottom by **DIE03** in (e) and (f). Average $K_d$ and $K_{Lu}$ derived from in situ data were used in (a) and (e); $K_d{}^p$ was used in (b) and (f). (j) and (l). The validation for each model is under itself. Validation for models (a), (b), (e) and (f) are presented in (c), (d), (g) and (h), respectively.

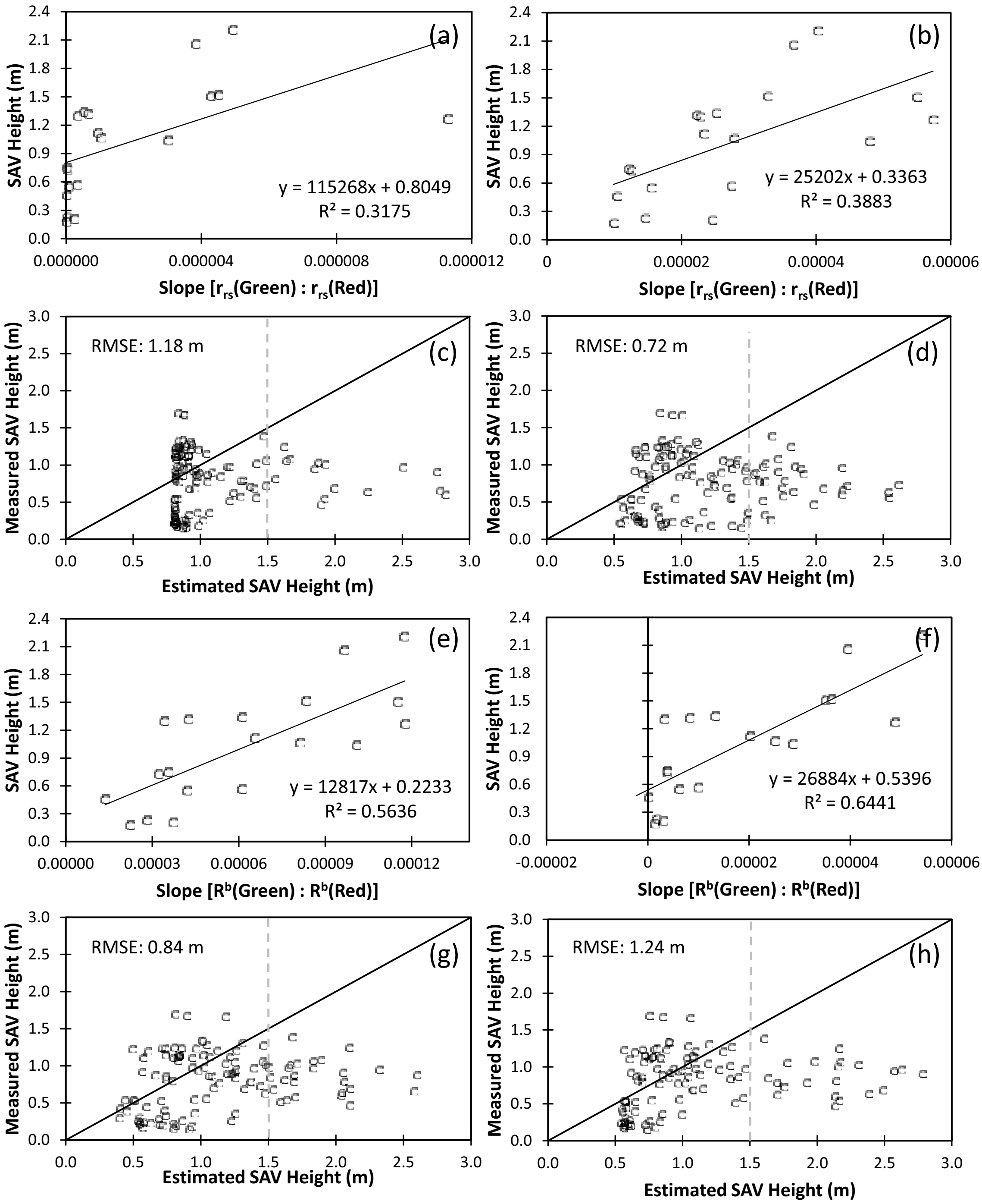

By the satellite data, the models did not fit well when using the GRVI ($R^2 < 0.3$). The models, using the Slope of the bottom retrieved by **PAL08** (Figure 46 (a) and (b)), did not have a meaningful $R^2$ either. The highest $R^2$ were obtained with the model using the Slope of the bottom retrieved by **DIE03** (Figure 46 (e) and (f)). It was noted that there was an overvaluation of the SAV with values higher than 1.5 m. Thus, it was decided to adjust the models, calibrated by the Slope (Figure 46), by the logarithmic functions in an attempt to increase the models accuracy (Figure 47 and Figure 48).

Figure 47 – Logarithmical regression between SAV height and Slope [(Green):(Red)] of SPOT image based on remote sensing reflectance of the bottom by **PAL08** Average $K_d$ derived from in situ data were used in (a) and $K_d{}^p$ was used in (b). Validation for models (a) and (b) are shown in (c) and (d), respectively.

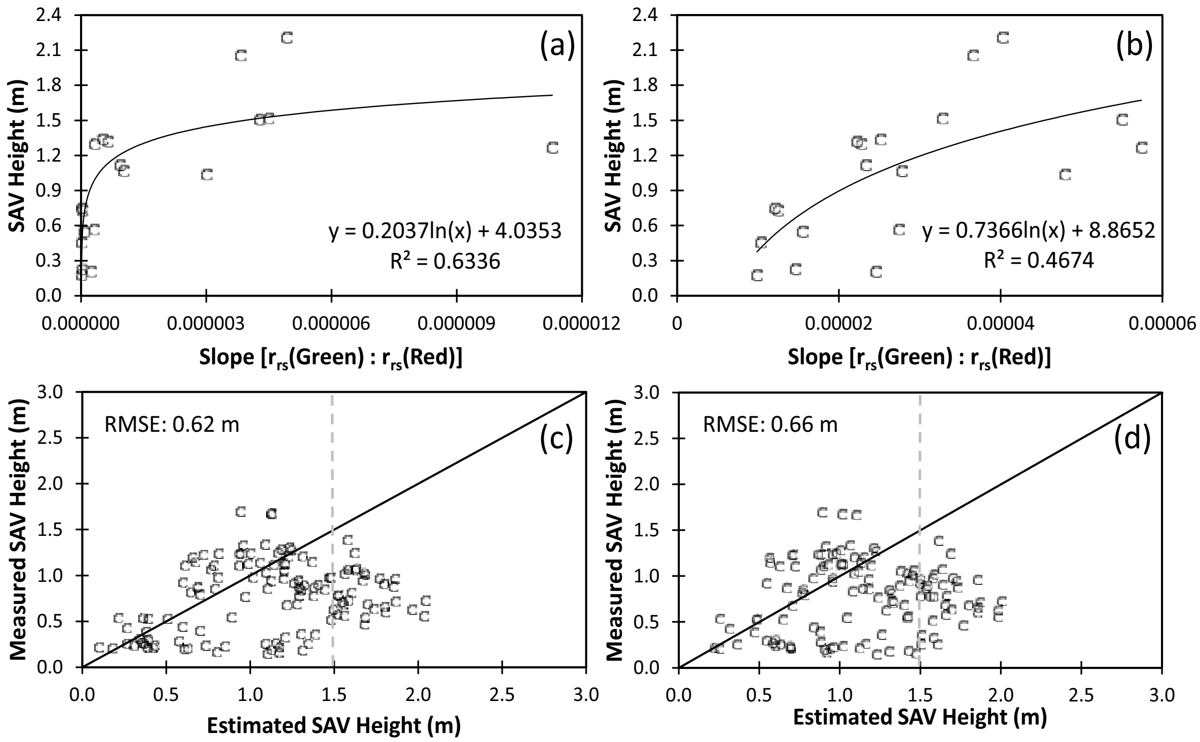

Figure 48 – Logarithmical regression between SAV height and Slope [(Green):(Red)] of SPOT image based on remote sensing reflectance of the bottom by **DIE03**. Average $K_d$ and $K_{Lu}$ derived from in situ data were used in (a) and $K_d^{\,p}$ was used in (b). Validation for models (a) and (b) are shown in (c) and (d), respectively.

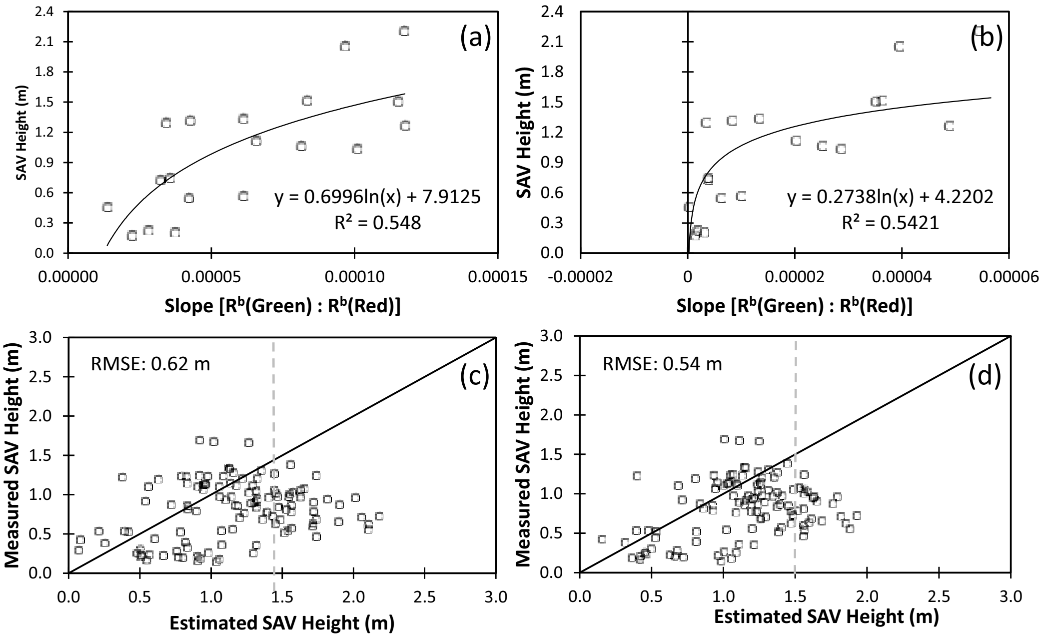


A significant improvement was noted in the models with the retrieved bottom by PAL08 (Figure 47) – the $R^2$ increased from 0.32 to 0.63 and from 0.39 to 0.47; and the RMSE decreased from 1.18 to 0.62 and from 0.72 to 0.66. About the models that use the bottom retrieved by DIE03 (Figure 48), there was a significant improvement in the RMSE decreasing from 0.84 to 0.62 and from 1.24 to 0.54. It is important to mention that even though an overvaluation of the SAV height values higher than 1.5 m keeps happening, there was a significant reduction in these values. Furthermore, there was improvement in the distribution points (Measured/Estimated) for all the models.

### 5.3 Submerged aquatic vegetation height mapping using spot-6 satellite image

This section is related to the following objective: To use and evaluate the performance of bio-optical models of the generation of maps of the distribution and SAV height through multispectral image – SPOT-6. The results in this section are based on the second field campaign data.

### 5.3.1 River Depth

The numerical grid generated from the interpolation by kriging of the depth data of the echosounder was divided into eleven theme classes. The theme map with depth classes is shown on Figure 3.

Figure 49 – Bathimetry of Bonito River – Nova Avanhandava Reservoir.

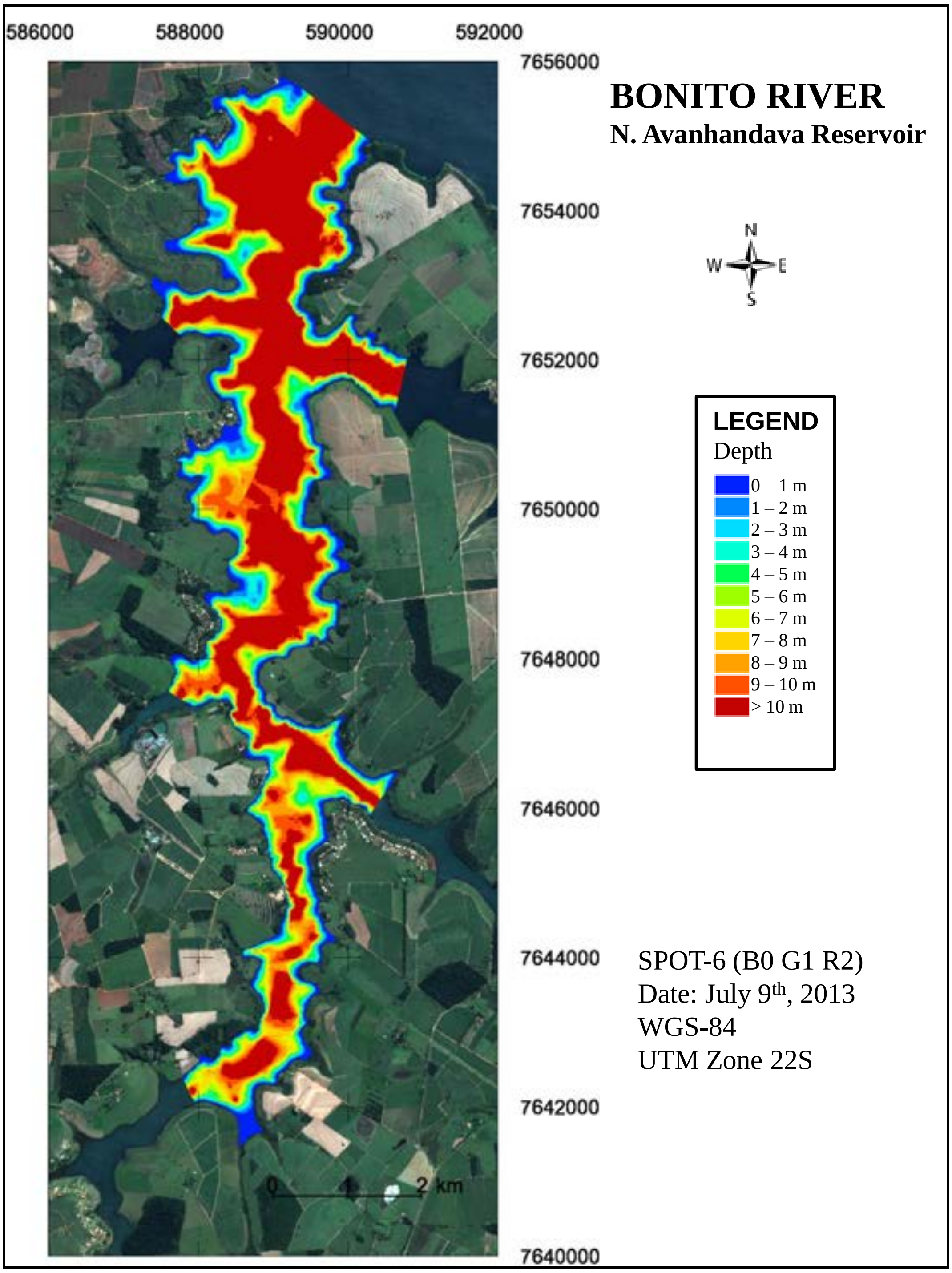

### 5.3.2 Submerged Aquatic Vegetation Height and Distribution

Through the Slope (Equation (28)) of the bottom retrieved by **DIE03** using average $K_d$ and $K_{Lu}$ derivative from the field data $E_d$ and $L_u$, it was possible to infer the places with SAV and the ones without SAV (Figure 50). This product was used as a mask for the maps of the SAV height estimative by SAV Model 1 (Equation (30)), SAV Model 2 (Equation (31)), SAV Model 3 (Equation (32)), SAV Model 4 (Equation (33)) and SAV Model 5 (Equation (34)).

Visually it was possible to check the effectiveness of the procedure used to define regions with SAV and regions without SAV. The red and yellow lines show the path taken by the echosounder and indicate regions with and without SAV, respectively. It was observed a strong correlation between the regions in green (Estimate of occurrence of SAV) with red lines in (Observation in field that indicates the presence of SAV) and also the regions in blue (Estimate of non-occurrence of SAV) with the yellow lines (Observation in field that indicates the absence of SAV).

Figure 50 – Map of the occurrence of Submerse Aquatic Vegetation.

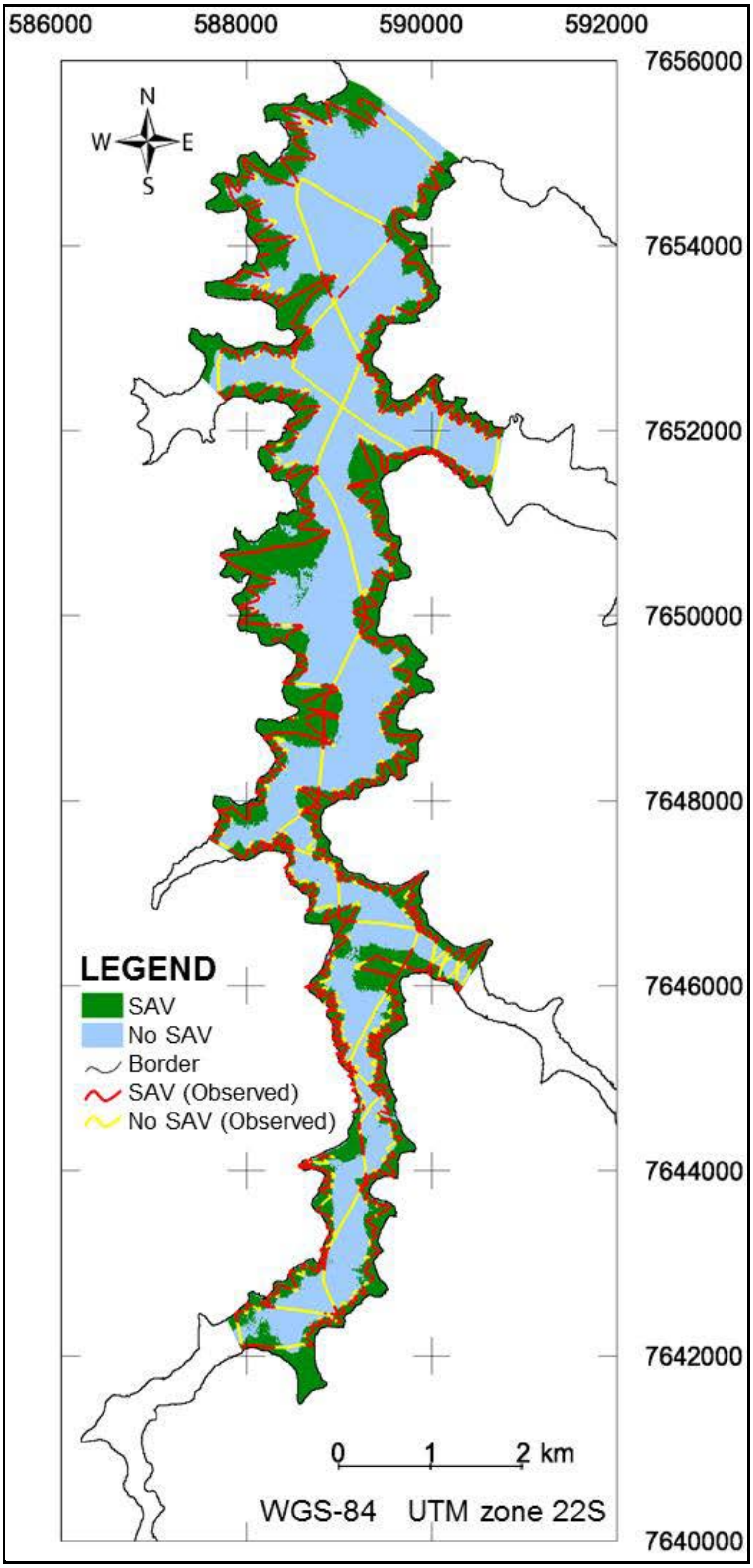


Figure 51 shows the estimation map of the SAV height using SAV Model 1 (Equation (30)). The GRVI of bottom reflectance retrieved by **DIE03** and the average $K_d$ and $K_{Lu}$ based on field data of $E_d$ and $L_u$ were was used.

Figure 51 – SAV height estimation using SAV Model 1 (Equation (30)). Bottom retrieved by **DIE03**.

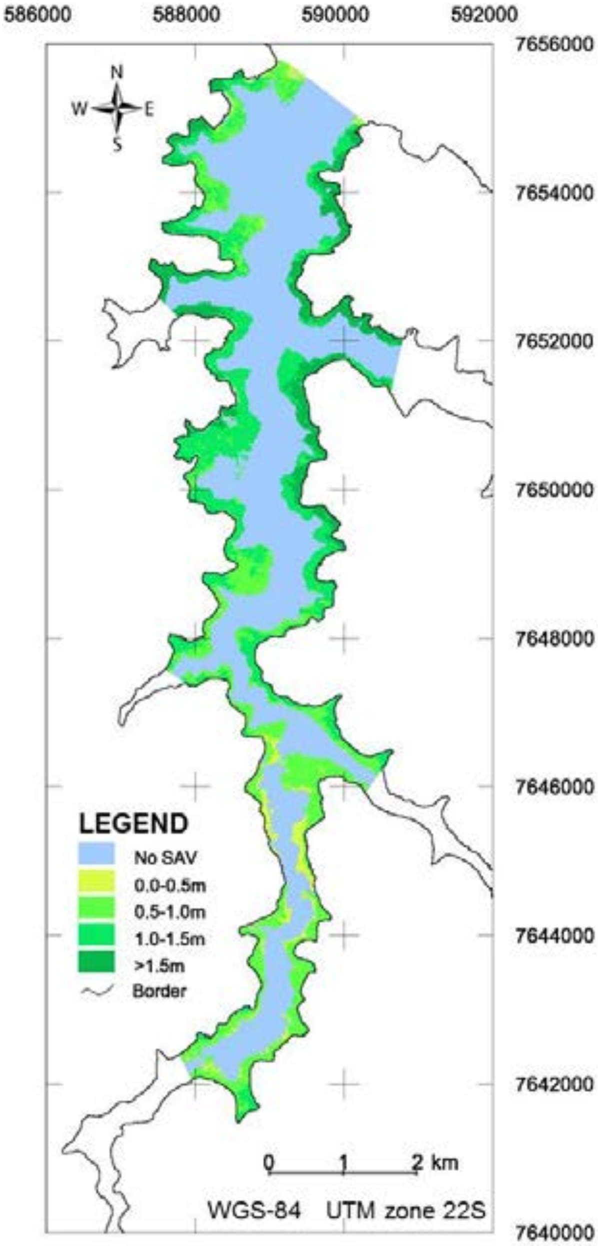


We can see the SAV taller in region close to Tietê River (downstream) than in regions upstream. This behavior matches with the echosounder data (observed information). SAV Model 1, used to estimate the SAV height, was based in field data for calibration.

Figure 52 shows the SAV height estimation map using SAV Model 2 (Equation (31)) in (a) and SAV Model 3 (Equation (32)) in (b). The Slope between the Green and Red bands of bottom reflectance retrieved by **PAL08** was used. $K_d$ based on the field data of $E_d$ was used in (a) and $K_d{}^P$ based on remote sensing reflectance proposed by Palandro et al. (2008), in (b).

Figure 52 – SAV height estimation using SAV Model 2 (Equation (31)) in (a) and SAV Model 3 (Equation (32)) in (b). Bottom retrieved by **PAL08**.

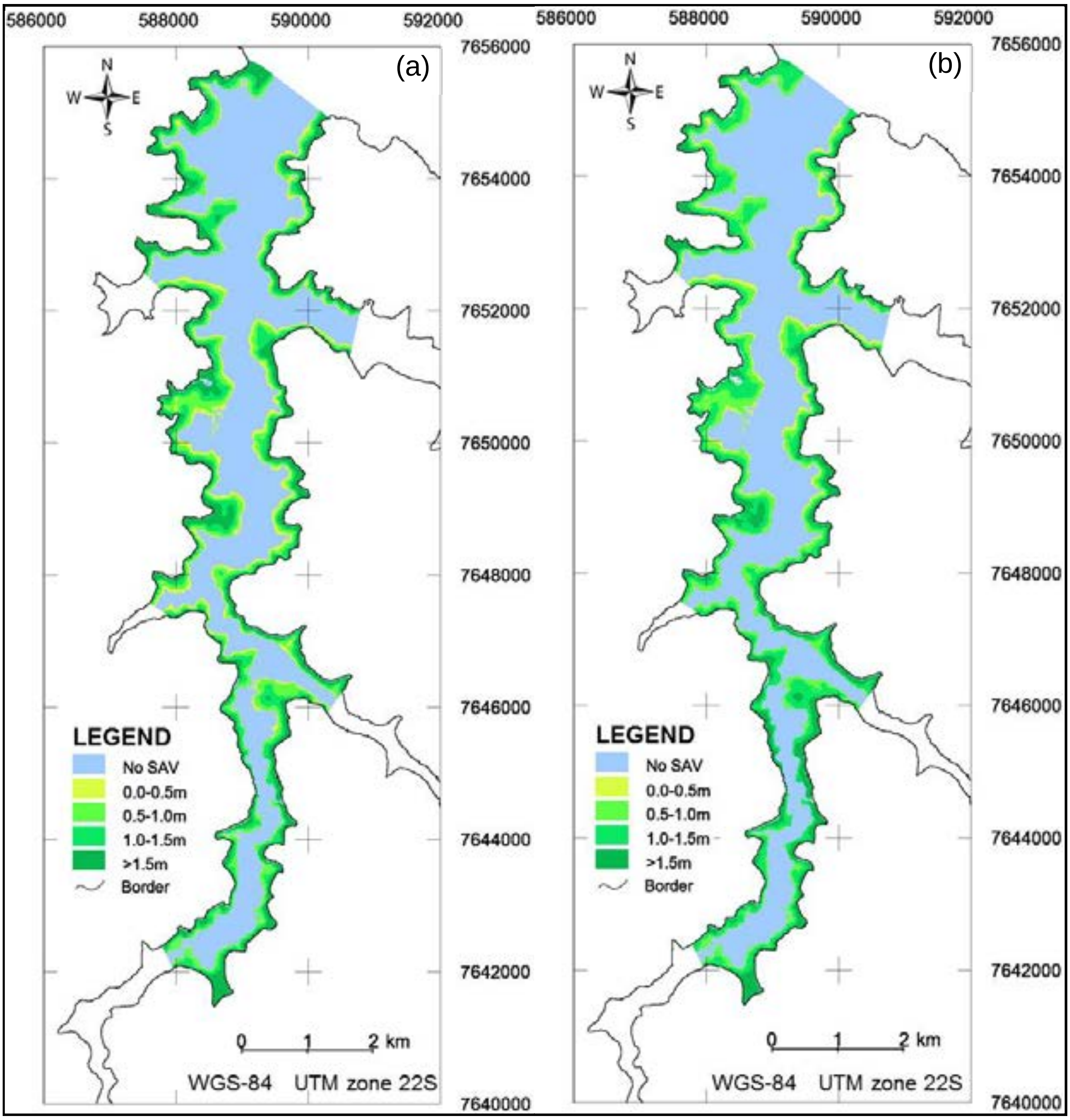


Figure 53 shows the SAV height estimative using Model 4 (Equation (33)) in (a) and Model 5 (Equation (34)) in (b). Slope between the Green and Red bands of reflectance of the bottom retrieved by **DIE03** was used. $K_d$ based on field data of $E_d$ was used in (a) and $K_d{}^P$ based on reflectance data of remote sensing, as proposed by Palandro et al. (2008), in (b). $K_{Lu}$ was calculated through field data of $L_u$.

Figure 53 – S SAV height estimation using SAV Model 4 (Equation (33)) in (a) and SAV Model 5 (Equation (34)) in (b). Bottom retrieved by **DIE03**.

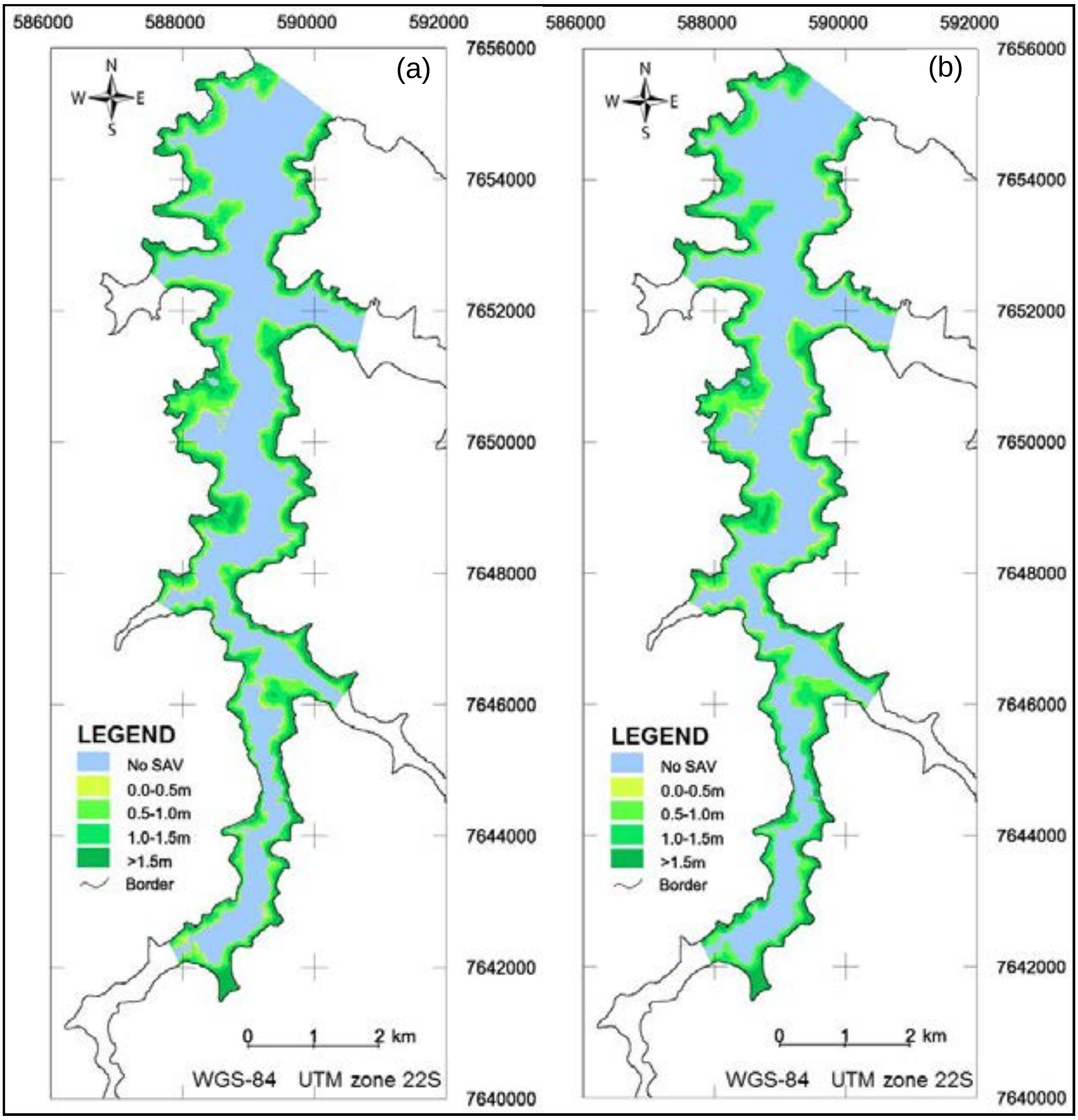


The SAV height map based on SPOT image (Figure 52 and Figure 53) presented similar results. Taller SAV is found in shallower water.

### 5.3.3 SAV Map Validation

For validation of SAV height estimation maps, confusion matrixes were used among the values calculated from the models applied on image SPOT-6 and the values observed in field by the echosounder. 160 pixels were collected for each defined class, in a total of 800 pixels.

Besides overall accuracy and Kappa, it was calculated the producer's accuracy – probability that a certain class (Observed) of an area on the ground is classified as such, and user's accuracy – probability that a pixel classified as a certain class (Calculated) in the map is really this class.

Table 9 – Confusion matrix of the SAV height estimation map using SAV Model 1 based on Reflectance retrieved by **DIE03**.

| | | **SAV Calculated (SAV Model 1)** | | | | | | |
|---|---|---|---|---|---|---|---|---|
| | | **No SAV** | **0.0-0.5m** | **0.5-1.0m** | **1.0-1.5m** | **>1.5m** | **Raw total** | **Producer's accuracy** |
| **SAV Observed** | **No SAV** | 136 | 3 | 20 | 1 | 0 | 160 | 0.85 |
| | **0.0-0.5m** | 34 | 16 | 69 | 28 | 13 | 160 | 0.10 |
| | **0.5-1.0m** | 17 | 14 | 54 | 60 | 15 | 160 | 0.34 |
| | **1.0-1.5m** | 6 | 1 | 50 | 73 | 30 | 160 | 0.46 |
| | **>1.5m** | 2 | 3 | 43 | 59 | 53 | 160 | 0.33 |
| | **Column total** | 195 | 37 | 236 | 221 | 111 | 800 | |
| | **User's accuracy** | 0.70 | 0.43 | 0.23 | 0.33 | 0.48 | | |
| | **Overall accuracy = 0.42** | | | | | | | |
| | **Kappa = 0.27** | | | | | | | |

Table 10 – Confusion matrix of the SAV height estimation map using SAV Model 2 based on Reflectance retrieved by **PAL08**.

| | | **SAV Calculated (SAV Model 2)** | | | | | | |
|---|---|---|---|---|---|---|---|---|
| | | **No SAV** | **0.0-0.5m** | **0.5-1.0m** | **1.0-1.5m** | **>1.5m** | **Raw total** | **Producer's Accuracy** |
| **SAV Observed** | **No SAV** | 136 | 6 | 18 | 0 | 0 | 160 | 0.85 |
| | **0.0-0.5m** | 36 | 25 | 39 | 44 | 16 | 160 | 0.16 |
| | **0.5-1.0m** | 17 | 10 | 31 | 53 | 49 | 160 | 0.19 |
| | **1.0-1.5m** | 3 | 16 | 69 | 56 | 16 | 160 | 0.35 |
| | **>1.5m** | 3 | 16 | 48 | 72 | 21 | 160 | 0.13 |
| | **Column total** | 195 | 73 | 205 | 225 | 102 | 800 | |
| | **User's accuracy** | 0.70 | 0.34 | 0.15 | 0.25 | 0.21 | | |
| | **Overall accuracy = 0.34** | | | | | | | |
| | **Kappa = 0.17** | | | | | | | |

Table 11 – Confusion matrix of the SAV height estimation map using SAV Model 3 based on Reflectance retrieved by **PAL08**.

| | | **SAV Calculated (SAV Model 3)** | | | | | | |
|---|---|---|---|---|---|---|---|---|
| | | **No SAV** | **0.0-0.5m** | **0.5-1.0m** | **1.0-1.5m** | **>1.5m** | **Raw total** | **Producer's Accuracy** |
| **SAV Observed** | **No SAV** | 136 | 1 | 12 | 11 | 0 | 160 | 0.85 |
| | **0.0-0.5m** | 36 | 13 | 38 | 50 | 23 | 160 | 0.08 |
| | **0.5-1.0m** | 15 | 7 | 31 | 64 | 43 | 160 | 0.19 |
| | **1.0-1.5m** | 3 | 11 | 75 | 59 | 12 | 160 | 0.37 |
| | **>1.5m** | 5 | 16 | 50 | 79 | 10 | 160 | 0.06 |
| | **Column total** | 195 | 48 | 206 | 263 | 88 | 800 | |
| | **User's accuracy** | 0.70 | 0.27 | 0.15 | 0.22 | 0.11 | | |
| | **Overall accuracy = 0.31** | | | | | | | |
| | **Kappa = 0.14** | | | | | | | |

Table 12 – Confusion matrix of the SAV height estimation map using SAV Model 4 based on Reflectance retrieved by **DIE03**.

| | | **SAV Calculated (SAV Model 4)** | | | | | | |
|---|---|---|---|---|---|---|---|---|
| | | **No SAV** | **0.0-0.5m** | **0.5-1.0m** | **1.0-1.5m** | **>1.5m** | **Raw total** | **Producer's Accuracy** |
| **SAV Observed** | **No SAV** | 136 | 8 | 16 | 0 | 0 | 160 | 0.85 |
| | **0.0-0.5m** | 32 | 28 | 61 | 25 | 14 | 160 | 0.18 |
| | **0.5-1.0m** | 17 | 6 | 31 | 61 | 45 | 160 | 0.19 |
| | **1.0-1.5m** | 7 | 9 | 65 | 67 | 12 | 160 | 0.42 |
| | **>1.5m** | 3 | 6 | 60 | 82 | 9 | 160 | 0.06 |
| | **Column total** | 195 | 57 | 233 | 235 | 80 | 800 | |
| | **User's accuracy** | 0.70 | 0.49 | 0.13 | 0.29 | 0.11 | | |
| | **Overall accuracy = 0.34** | | | | | | | |
| | **Kappa = 0.17** | | | | | | | |

Table 13 – Confusion matrix of the SAV height estimation map using SAV Model 5 based on Reflectance retrieved by **DIE03**.

| | | SAV Calculated (SAV Model 5) | | | | | | |
|---|---|---|---|---|---|---|---|---|
| | | **No SAV** | **0.0-0.5m** | **0.5-1.0m** | **1.0-1.5m** | **>1.5m** | **Raw total** | **Producer's Accuracy** |
| **SAV Observed** | **No SAV** | 136 | 6 | 18 | 0 | 0 | 160 | 0.85 |
| | **0.0-0.5m** | 33 | 31 | 36 | 49 | 11 | 160 | 0.19 |
| | **0.5-1.0m** | 17 | 7 | 31 | 72 | 33 | 160 | 0.19 |
| | **1.0-1.5m** | 7 | 7 | 66 | 74 | 6 | 160 | 0.46 |
| | **>1.5m** | 2 | 7 | 65 | 85 | 1 | 160 | 0.01 |
| | **Column total** | 195 | 58 | 216 | 280 | 51 | 800 | |
| | **User's accuracy** | 0.70 | 0.53 | 0.14 | 0.26 | 0.02 | | |
| | **Overall accuracy = 0.34** | | | | | | | |
| | **Kappa = 0.18** | | | | | | | |

The SAV height map estimated by SAV Model 1 presented better results based on the confusion matrix (Table 9). An overall accuracy of 42% was obtained and the Kappa of 0.27, considered as having *Fair Agreement*. The confusion matrix related to the maps of estimation of SAV height using SAV Models 2, 3, 4 and 5 presented similar values to the ones of the overall accuracy varying between 31% and 34% and Kappa varying between 0.14 and 0.18. Based on the Kappa value, the estimation can be considered as having *Slight agreement*.

“No SAV” class presented the best results both for producer’s accuracy as for user’s accuracy. It shows the success in obtaining the occurrence of SAV by using the mask (Figure 50). After “No SAV” class, producer’s accuracy presented the best results for “1.0-1.5m” class, with numbers varying from 35% to 46%, i.e., in region with SAV height between 1.0 and 1.5 m the models were capable of estimating correctly from 35 to 46% of this class. For User’s accuracy, the best results were observed for “0.0-0.5m” class, with numbers varying from 27% and 53%. Therefore, the estimated classes for 0.0-0.5m presented an accuracy that varied from 27% (SAV Model 3) to 53% (SAV Model 5).

Low numbers, both of producer’s accuracy as for user’s accuracy, were found for “>1.5m” class. Thus, the descriptive statistics was calculated from SAV height data to analyze the possibility of changing the estimated classes. With the more than 15 thousand points with SAV height values obtained by the echosounder, a histogram was generated and the mean was calculated, median, standard deviation, first quartile (Q1) and third quartile (Q3) (Figure 54).

Figure 54 – Histogram and descriptive statistic of SAV height in Bonito River.

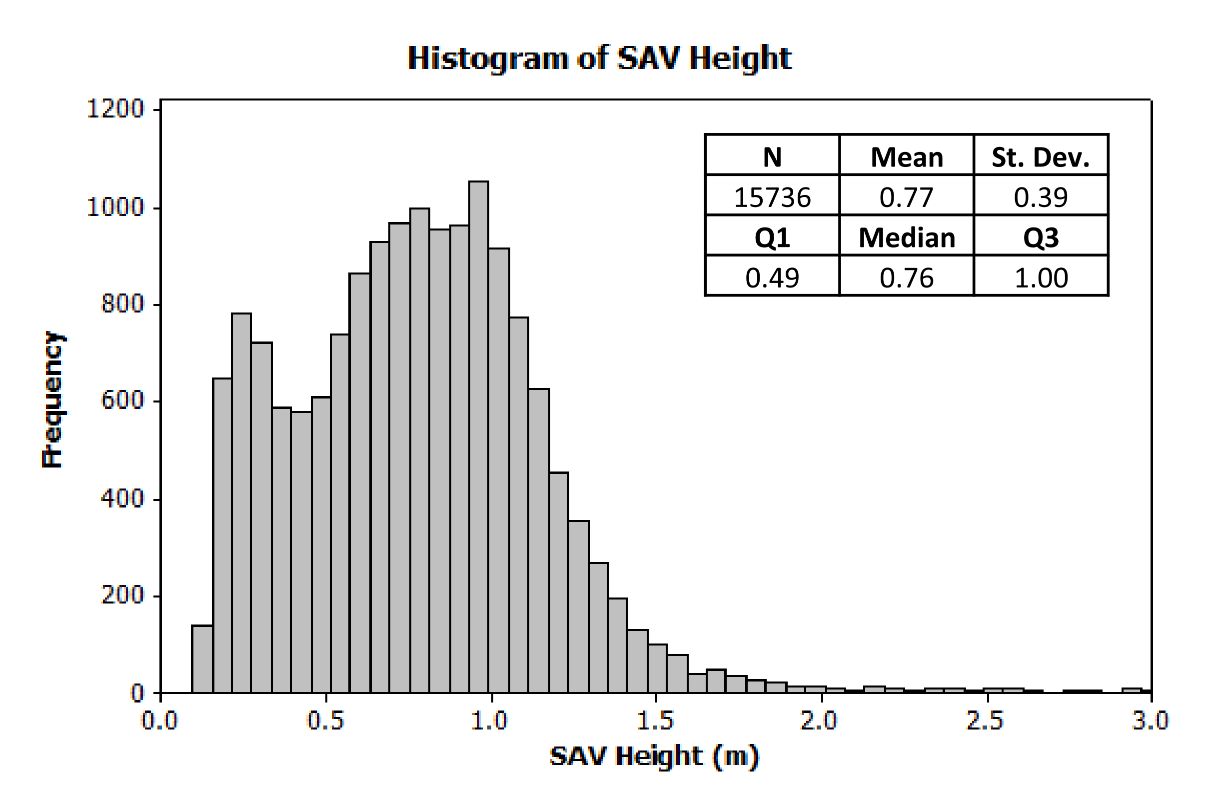


We can observe that there is low presence of SAV values higher than 1.5 m. 97% of the SAV measured in the study site present values lower than 1.5 m height. Therefore, the confusion matrix of the SAV height maps was calculated disregarding "*>1.5m*" class. The new confusion matrix were calculated considering "1.0-1.5" and ">1.5" classes as just one, that is, belonging to the new ">1.0m" class. Thus, each SAV height class in the study area would have significant quantity of samples.

Table 14 – Confusion matrix of the SAV height estimation map using SAV Model 1 based on Reflectance retrieved by **DIE03**.

| | | **SAV Calculated (Model 1)** | | | | | |
|---|---|---|---|---|---|---|---|
| | | **No SAV** | **0.0-0.5m** | **0.5-1.0m** | **>1.0m** | **Raw total** | **Producer's accuracy** |
| **SAV Observed** | **No SAV** | 136 | 3 | 20 | 1 | 160 | 0.85 |
| | **0.0-0.5m** | 34 | 16 | 69 | 41 | 160 | 0.10 |
| | **0.5-1.0m** | 17 | 14 | 54 | 75 | 160 | 0.34 |
| | **>1.0m** | 8 | 4 | 93 | 215 | 320 | 0.67 |
| | **Column total** | 195 | 37 | 236 | 332 | 800 | |
| | **User's accuracy** | 0.70 | 0.43 | 0.23 | 0.65 | | |
| | **Overall accuracy = 0.53** | | | | | | |
| | **Kappa = 0.34** | | | | | | |

Table 15 – Confusion matrix of the SAV height estimation map using SAV Model 2 based on Reflectance retrieved by **PAL08**.

| | | **SAV Calculated (Model 2)** | | | | | |
|---|---|---|---|---|---|---|---|
| | | **No SAV** | **0.0-0.5m** | **0.5-1.0m** | **>1.0m** | **Raw total** | **Producer's accuracy** |
| **SAV Observed** | **No SAV** | 136 | 6 | 18 | 0 | 160 | 0.85 |
| | **0.0-0.5m** | 36 | 25 | 39 | 60 | 160 | 0.16 |
| | **0.5-1.0m** | 17 | 10 | 31 | 102 | 160 | 0.19 |
| | **>1.0m** | 6 | 32 | 117 | 165 | 320 | 0.52 |
| | **Column total** | 195 | 73 | 205 | 327 | 800 | |
| | **User's accuracy** | 0.70 | 0.34 | 0.15 | 0.50 | | |
| | **Overall accuracy = 0.45** | | | | | | |
| | **Kappa = 0.23** | | | | | | |

Table 16 – Confusion matrix of the SAV height estimation map using SAV Model 3 based on Reflectance retrieved by **PAL08**.

| | | SAV Calculated (Model 3) | | | | | |
|---|---|---|---|---|---|---|---|
| | | **No SAV** | **0.0-0.5m** | **0.5-1.0m** | **>1.0m** | **Raw total** | **Producer's accuracy** |
| **SAV Observed** | **No SAV** | 136 | 1 | 12 | 11 | 160 | 0.85 |
| | **0.0-0.5m** | 36 | 13 | 38 | 73 | 160 | 0.08 |
| | **0.5-1.0m** | 15 | 7 | 31 | 107 | 160 | 0.19 |
| | **>1.0m** | 8 | 27 | 125 | 160 | 320 | 0.50 |
| | **Column total** | 195 | 48 | 206 | 351 | 800 | |
| | **User's accuracy** | 0.70 | 0.27 | 0.15 | 0.46 | | |
| | **Overall accuracy = 0.43** | | | | | | |
| | **Kappa = 0.19** | | | | | | |

Table 17 – Confusion matrix of the SAV height estimation map using SAV Model 4 based on Reflectance retrieved by **DIE03**.

| | | SAV Calculated (Model 4) | | | | | |
|---|---|---|---|---|---|---|---|
| | | **No SAV** | **0.0-0.5m** | **0.5-1.0m** | **>1.0m** | **Raw total** | **Producer's accuracy** |
| **SAV Observed** | **No SAV** | 136 | 8 | 16 | 0 | 160 | 0.85 |
| | **0.0-0.5m** | 32 | 28 | 61 | 39 | 160 | 0.18 |
| | **0.5-1.0m** | 17 | 6 | 31 | 106 | 160 | 0.19 |
| | **>1.0m** | 10 | 15 | 125 | 170 | 320 | 0.53 |
| | **Column total** | 195 | 57 | 233 | 315 | 800 | |
| | **User's accuracy** | 0.70 | 0.49 | 0.13 | 0.54 | | |
| | **Overall accuracy = 0.46** | | | | | | |
| | **Kappa = 0.25** | | | | | | |

Table 18 – Confusion matrix of the SAV height estimation map using SAV Model 5 based on Reflectance retrieved by **DIE03**.

| | | **SAV Calculated (Model 5)** | | | | | |
|---|---|---|---|---|---|---|---|
| | | **No SAV** | **0.0-0.5m** | **0.5-1.0m** | **>1.0m** | **Raw total** | **Producer's accuracy** |
| **SAV Observed** | **No SAV** | 136 | 6 | 18 | 0 | 160 | 0.85 |
| | **0.0-0.5m** | 33 | 31 | 36 | 60 | 160 | 0.19 |
| | **0.5-1.0m** | 17 | 7 | 31 | 105 | 160 | 0.19 |
| | **>1.0m** | 9 | 14 | 131 | 166 | 320 | 0.52 |
| | **Column total** | 195 | 58 | 216 | 331 | 800 | |
| | **User's accuracy** | 0.70 | 0.53 | 0.14 | 0.50 | | |
| | **Overall accuracy = 0.46** | | | | | | |
| | **Kappa = 0.24** | | | | | | |

There was an improvement both on overall accuracy as on Kappa in all models after the combination of “1.0-1.5m” and “>1.5m” classes. The estimation of SAV height by SAV Model 1 presented improvement on overall accuracy from 42% to 53% and on Kappa from 0.27 to 0.34. Although the value of Kappa is still on *Fair agreement* level, great improvement could be observed specially in “>1.0m” class, which showed numbers of producer’s accuracy and user’s accuracy of 67% and 65%, respectively. In other words, in regions with SAV higher than 1 m, SAV Model 1 can estimate correctly 67% of those regions. Besides, based on user’s accuracy, the model estimated correctly 65% of the regions with SAV higher than 1.5 m.  In the estimation of SAV height using SAV Models 2, 3 4 and 5, there was also significant improvement of “>1.0” class in user’s accuracy, with values between 46% and 54%, and on producer’s accuracy, with values between 50% and 53%.

For “0.0-0.5m” and “0.5-1.0m” classes, producer’s accuracy presented results lower than 34% for estimation of SAV height in all models. That indicates the difficulty of the models in estimating SAV height for those values. SAV height up to 1m may have not sufficient signal to be detected by the sensors.

Models that used **PAL08** to retrieve the bottom (SAV Models 2 and 3) presented the lowest values for “0.0-0.5m” and “0.5-1.0m” classes, both for producer’s accuracy and user’s accuracy. But SAV Model 1, 4 and 5, that used bottom retrieved by **DIR03**, presented acceptable values for user’s accuracy (between 43% and 53%), and however presented low values for “0.5-1.0m” class.

In general, the estimation of SAV height by SAV Model 1 (Equation (30)) presented better results, in comparison to other models. We have to remind that this model is the only one calibrated based on remote sensing reflectance ($R_{rs}$) collected in the field. This model also differs from others by having used the GRVI of bottom retrieved by **DIE03**. The Figure 55 shows the map of the estimation of SAV height using SAV Model 1 with the following classes: No SAV, 0.0-0.5m, 0.5-1.0m and >1.0m.

The distribution of SAV height is compatible with the attenuation coefficient of water. In areas with higher radiation attenuation values, a predominance of classes 0.0-0.5m and 0.5-1.0m (upstream) was observed and in regions with lower values of the attenuation coefficient was observed a predominance of class > 1.0m (middle and downstream).

To evaluate the effectiveness of the procedure adopted to identify the occurrence of SAV (Figure 50) the classes described in the confusion matrix were divided into just two classes ("No SAV" and "SAV"). The confusion matrix considering these two classes is shown in Table 19.

Figure 55 – SAV height estimation using SAV Model 1. Bottom retrieved by **DIE03**.

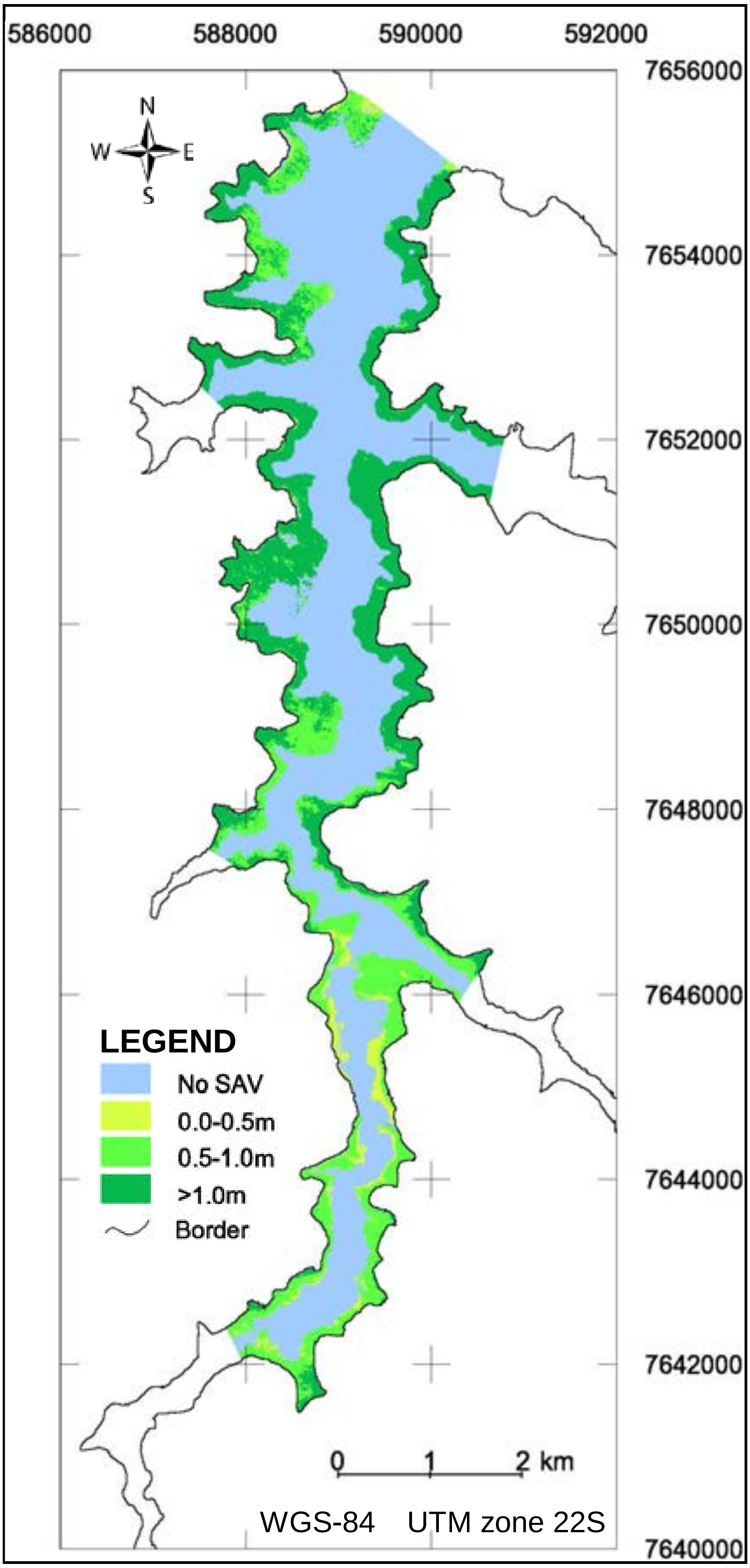

Table 19 – Confusion matrix of SAV distribution map. Reflectance of the bottom was retrieved by **DIE03**.

| | | **SAV Calculated** | | | |
|---|---|---|---|---|---|
| | | **No SAV** | **SAV** | **Raw total** | **Producer's accuracy** |
| **SAV Observed** | **No SAV** | 136 | 24 | 160 | 0.85 |
| | **SAV** | 59 | 581 | 640 | 0.91 |
| | **Column total** | 195 | 605 | 800 | |
| | **User's accuracy** | 0.70 | 0.96 | | |
| | **Overall accuracy = 0.90** | | | | |
| | **Kappa = 0.70** | | | | |

The proposed procedure for estimating the SAV distribution in the study area was highly effective, with an overall accuracy of 90% and Kappa 0.7. According to the Kappa value an estimated SAV position would have a Substantial agreement. According to the user's accuracy, 70% of the areas estimated as no SAV were correct, and 96% of the estimated area with SAV were correct. It was also found that 91% of regions with SAV (Observed) had their areas estimated correctly, i.e. belonging to the class "SAV"; and 85% of the regions without SAV (Observed) were estimated correctly, i.e. belonging to the "No SAV" class.

## 6. CONCLUSION

Considering the depth range up to 1 m and despite high radiation availability, SAV is not observed throughout the entire water column. Such observations may be due to the excess available radiation for the incidence and development of aquatic vegetation species therein (*E. densa* and *E. najas*), which require little radiation and can be hindered by its excess (RODRIGUES and THOMAZ, 2010; TAVECHIO and THOMAZ, 2003) and strong wind action (waves) near the banks (THOMAZ, 2006).

In the P01 region (Field 1) with a greater euphotic zone limit, the SAV reached great heights at depths up to 8 m. The maximum SAV height decreased with upstream direction. P01 had the smallest $K_d$ *PAR* (0.516 $m^{-1}$), which is consistent with the SAV behaviour in this region, wherein the SAV grown better.

Despite decreasing at greater depths, the radiation remained sufficient for regional species' growth because they require low radiation levels. Therefore, in addition to sufficient radiation availability, the submerged vegetation also had area for growth. According to Rodrigues and Thomaz (2010), larger SAV heights are typically observed at greater depths likely due to the macrophyte species trait wherein it extends to find sufficient radiation for development.

In the final colonisation region near the euphotic zone's depth (where $E_d(z)/E_d(0^-)$ is approximately 1%), the SAV heights decreased. At depths greater than the euphotic zone, SAV growth was not significant in the four zones.

The PLW and PLL was an important optical parameter to analyze the behaviour of SAV along the river. It was seen that in regions with low TSS, like in P01 and P02, as PLW increases SAV height decreases. It means that with the PLW increases, SAV do not have to grow upward to receive light enough to grow.

Studies in the Rosana (Paranapanema River) and Itaipu (Paraná River) reservoirs have shown that subaquatic radiation can explain the different distribution patterns for *E. densa* and *E. najas* within the same reservoir. The probability for *Egeria najas* growth is greater for less transparent water compared with *Egeria densa* (BINI and THOMAZ, 2005; THOMAS, 2006). Therefore, because both SAV species has been predominant in the area investigated herein, the different in traits for *E. najas* and *E. dens*a also to aid in explaining the varied SAV distributions along the Bonito River.

We prove that studies on subaquatic radiation availability measured by the vertical attenuation of downwelling irradiance in the water column can aid in understanding SAV behaviour in tropical reservoirs and, therefore, contribute to its management. In addition, knowing the solids in suspension concentration can provide additional information on distribution and development for the vegetation studied. Beside the radiation availability, other limiting factors, not studied here, may influence such behaviour, including nutrients, stream velocity and bottom declivity.

Models to estimate the SAV height based on bottom reflectance retrieved by **PAL08** (PALANDRO et al., 2008) and **DIE03** (DIERSSEN et al., 2003) were calculated. Our results showed that the remote sensing reflectance collected on field survey presented the most accurate estimative of SAV height when using the Dierssen's model, GRVI, average attenuation coefficients ($K_d$ and $K_{Lu}$) and logarithmical function to fit the regression.

The models that used the Slope of bottom reflectance did not have significant adjustments with the reflectance data collected in the field, with $R^2$ lower than 0.3. The reason for that can be explained by the limited number of samplings (eight) used to calibrate the model. Thus, it is recommended to use a greater number of sampling elements, collected in the field, to better adjust and analyze the generated models.

The models based on bottom reflectance retrieved by **PAL08** and **DIE03** using multispectral SPOT-6 image achieved the best results (RMSE between 0.54 and 0.66) when the Slope [(Green):(Red)] and *ln* function to fit the regression were used to calibrate SAV height estimative. It was noted similar results when using the bottom retrieved by **PAL08** or by **DIE03**. No significant difference was detected when using the attenuation coefficient $K_d$ or $K_d{}^p$ either. Thus, assuming that the depth of water body is known, the model that used **PAL08** and $K_d{}^p$ is an alternative when the field data is not available because the $K_d{}^p$ can be obtained directly from the image. Even though the $K_d{}^p$ underestimates the diffuse attenuation coefficient values, its usage also provided significant results for generate models of estimation of SAV, when SPOT-6 image was used. Thus, in a lack of field data, the $K_d{}^p$ may be an alternative.

It was noted that the logarithmical function provided a significant improvement on models adjustment, both on the model based on in situ data and based on satellite images. The *ln* provided an improvement on the $R^2$ and/or on the RMSE of the analyzed models.

As proved by Ma et al. (2008), vegetation index can present a good correlation with the submerged vegetation biomass. However, the vegetation biomass cannot be directly related with the submerged vegetation height (SILVEIRA et al., 2009). Thus, models to estimate the submerged vegetation height is still a challenge for researchers. The presented results (with RMSE between 0.40 and 0.66) can be considered encouraging.

Because only the wavelengths, corresponding to the center of Green and Red bands of multispectral images (560 and 660 nm) and the bands themselves, were tested, it is recommended to test other wavelengths in order to analyze the electromagnetic spectrum regions that most contribute to estimate the SAV height in inland waters. It is also recommended to test the models presented in others inland waters.

Based on satellite image (SPOT-6), the estimative of SAV height through SAV Model 1 showed better results on the mapping, with an overall accuracy of 53% and Kappa 0.34, being considered with fair agreement. This model was the only one based on the GRVI of the bottom retrieved by **DIE03**. Another difference is that the SAV Model 1 was calibrated with data collected from radiometers on the field. The better result may be due to the fact that, to calibrate models involving submerged targets, the collected data on the field can provide information with greater reliability than data acquired by satellite images, mainly by the influence of atmosphere. Despite that, it is recommended the calibration with field data with the highest number of samples so that the models are more robust.

Analyzing classes obtained using SAV Model 1 individually, good accuracy is observed only to “No SAV” and “>1.0m” classes. That means that in regions with SAV up to 1m high did not show difference in the spectral response capable of distinguishing the adopted classes. But spectral response in regions with SAV height higher than 1m it can differ from regions with lower heights. Therefore, it is recommended to use the same methodology for create a map of SAV height with just three classes: (i) No SAV; (ii) 0.0 – 1.0 m; and (iii) > 1.0 m.

The difficulty in studying targets submersed in freshwater due to high concentration of materials dissolved and suspended in the water is known. Thus, the estimation of SAV height in the study area is complex. Despite that, the bottom retrieval using models based on theory of radiative transference in the water column was capable to provide spectral response enough to distinguish regions with SAV from regions without SAV with high accuracy (Overall accuracy = 90%).

The models that used the bottom retrieved by **DIE03** achieved higher efficacy in the estimation of SAV height in comparison to the models that used the bottom retrieved by **PAL08**. The main difference among the models is the use of the diffuse attenuation coefficient of $L_u$, that is, $K_{Lu}$.

Many authors have obtained success mapping submerged targets using hyperspectral data (RIPLEY et al., 2009; SANTOS et al., 2009; MISHRA et al., 2006) or multispectral images in oceanic or coastal waters (MISHRA et al., 2005b; GULLSTRÖM et al., 2006). However, the estimative of the SAV height and position in freshwaters with multispectral data is still little studied. Therefore, the results presented on this study brought relevant contributions.

**REFERENCES**


ADLER-GOLDEN, S. M.; MATTHEW, M. W.; BERNSTEIN, L. S.; LEVINE, R. Y.; BERK, A.; RICHTSMEIER, S. C.; ACHARYA, P. K.; ANDERSON, G. P.; FELDE, G.; GARDNER, J.; HIKE, M.; JEONG, L. S.; PUKALL, B.; MELLO, J.; RATKOWSKI, A.; BURKE, H. -H. Atmospheric correction for shortwave spectral imagery based on MODTRAN4. **SPIE Proc. Imaging Spectrometry**, v. 3753, p. 61-69, 1999.

AES Tietê. Web site. Available: <http://www.aestiete.com.br/>. Access: November 9th, 2013.

ALBERT, A.; MOBLEY, C. D. An analytical model for subsurface irradiance and remote sensing reflectance in deep and shallow case-2 waters. **Optics Express**, v. 11, n. 22, p. 2873-2890, 2003.

ALBRIGHT, T. P.; ODE, D. J. Monitoring the dynamics of an invasive emergent macrophyte community using operational remote sensing data. **Hydrobiologia**, v. 661, n. 1, p. 469-474, 2011.

ARAÚJO-LIMA, C. A. R. M.; AGOSTINHO, A. A.; FABRÉ, N. N. Trophic aspects of fish communities in Brazilian rivers and reservoirs. In: TUNDISI, J. G.; BICUDO, C. E. M.; MATSUMURA-TUNDISI, T. (Ed.). **Limnology in Brazil**. Rio de Janeiro: ABC/SBL, 1995. p. 105-136.

ARMSTRONG, R. A. Remote sensing of submerged vegetation canopies for biomass estimation. **International Journal of Remote Sensing**, v. 14, n. 3, p. 621–627, 1993.

ASHRAF, S.; BRABYN, L.; HICKS, B. J.; COLLIER, K. Satellite remote sensing for mapping vegetation in New Zealand freshwater environments: A review. **New Zealand Geographer**, v. 66, p. 33-43, 2010.

ASTRIUM. **SPOT 6 & SPOT 7 Imagery – User guide**. SI/DC/13034-v1.0, 2013.

BAILEY, T. C.; GATRELL, A. C. **Interactive spatial data analysis.** Harlow: Longman Higher Education, 1995.

BARSI, J. A.; LEE, K.; KVARAN, G.; MARKHAM, B. L. PEDELTY, J. A. The Spectral Response of the Landsat-8 Operational Land Imager. **Remote Sensing**, v. 6, p. 10232-10251, 2014.

BINI, L. M.; THOMAZ, S. M.;. Prediction of *Egeria najas and Egeria densa* occurrence in a large subtropical reservoir (Itaipu Reservoir, Brazil-Paraguay). **Aquatic Botany**, v. 83, p. 227–238, 2005.

BIOSONICS. **User Guide: EcoSAVTM 1**. BioSonics Inc: Seattle, 2008. 48 p.

BIOSONICS. **User Guide: Visual AcquisitionTM 5.0**. Biosonics Inc: Seattle, 2004. 60 p.

BIUDES, J. F. V.; CAMARGO, A. F. M. Estudos dos fatores limitantes à produção primária por macrófitas aquáticas no Brasil. **Oecologia Brasiliensis**, v. 12, n. 1, 2008.

BOSCHI, L. S. Espacialização do biovolume de plantas aquáticas submersas a partir da integração de dados obtidos por sensores remotos. 2011. 162 f. **Tese (Doutorado em Ciências Cartográficas)** – Faculdade de Ciências e Tecnologia, Universidade Estadual Paulista, Presidente Prudente.

BRANDO, V. E.; ANSTEE, J. M.; WETTLE, M.; DEKKER, A. G.; PHINN, S. R.; ROELFSEMA, C. A physics based retrieval and quality assessment of bathymetry from suboptimal hyperspectral data. **Remote Sensing of Environment,** v. 113, p. 755-770, 2009.

BRANDO, V. E.; DEKKER, A. G. Satellite hyperspectral remote sensing for estimating estuarine and coastal water quality. **IEEE Transaction on Geoscience and Remote Sensing,** v. 41, p. 1378–1387, 2003.

CAFFREY A. J.; HOYER, M.V.; CANFIELD JR., D. E. Factors affecting the maximum depth of colonization by submersed macrophytes in Florida lakes. **Lake Reserv. Manage.**, v.23, p. 287-297, 2007.

CAMARGO, A. F. M.; PEZZATO, M. M. AND HENRY-SILVA, G. G. Fatores limitantes à produção primária de macrófitas aquáticas In: THOMAZ, S. M. AND BINI, L. M. **Ecologia e manejo de macrófitas aquáticas**. Maringá: EDUEM. p. 59-83, 2003.

CARPENTER, S. R.; LODGE, D. M. Effects of submersed macrophytes on ecosystem processes. Aquatic Botany, p. 341-370, 1986.

CAVENAGHI, A. L.; VELINI, E. D.; GALO, M. L. B. T.; CARVALHO, F. T.; NEGRISOLI, E.; TRINDADE, M. L. B.; SIMIONATO, J. L. A. Caracterização da qualidade da água e sedimentos relacionados com a ocorrência de plantas aquáticas em cinco reservatórios da bacia do rio Tietê. **Planta Daninha**, Edição Especial, v. 21, p. 43-52, 2003.

CBH-BT/CETEC: Comitê da Bacia Hidrográfica do Baixo Tietê. Centro Tecnológico da Fundação Paulista de Tecnologia e Educação. Situação dos Recursos Hídricos do Baixo Tietê – Minuta preliminar do relatório técnico final, Lins, CBH-BT, 1999. Available: <http://www.sigrh.sp.gov.br/sigrh/ARQS/RELATORIO/CRH/CBH-BT/232/relbtseg.pdf>. Access: May 8th, 2013.

CBH-BT: Comitê da Bacia Hidrográfica do Baixo Tietê: Fundamentos para a implantação da cobrança pelo uso dos recursos hídricos, 2009. Available: <http://www.sigrh.sp.gov.br/sigrh/cobranca/pdf/fundamentacao_cobranca_05.pdf>. Access: May 8th, 2013.

CHO, H. J.; MISHRA, D.; CLARKE, C. KAMEROSKY, A. Hyperspectral signal bands to HICO image data bands for seagrass mapping. In: **IEEE Workshop on**

**Hyperspectral Image and Signal Processing: Evolution in Remote Sensing** (Whispers 2013), IEEE, Gainesville, Florida, USA, 2013.

CLESCERI, L. S.; GREENBERG, A. E.; EATON, A. D. **Standard methods for the examination of water and wastewater**. 20th ed. Washington: American Public Health Association, 1998.

COHEN, J. A coefficient of agreement for nominal scales. **Educ. Psychol. Meas**., v. 20, p. 37-46, 1960.

CONGALTON, R. G. A review of assessing the accuracy of classifications of remotely sensed data. **Remote Sensing of Environment**, v. 37, p. 35-46, 1991.

DALL'OLMO, G.; GITELSON, A. A. Effect of bio-optical parameter variability on the remote estimation of chlorophyll-a concentration in turbid productive waters: experimental results. **Applied Optics**, v. 44, n. 3, 2005.

DASH, P.; WALKER, N. D.; MISHRA, D. R.; HU, C.; PINCKNEY, J. L.; D'SA, E. J. Estimation of cyanobacterial pigments in a freshwater lake using OCM satellite data. **Remote Sensing of Environment,** v. 115, p. 3409-3423, 2011.

DEKKER, A. G.; BRANDO, V. E.; ANSTEE, J. M.; PINNEL, N.; KUTSER, T.; HOOGEBOOM, E. J.; PETERS, S.; PASTERKAMP, R.; VOS, R.; OLBERT, C.; MALTHUS, T. J. M. Imaging spectrometry of water. In: VAN DER MEER, F. D.; DE JONG, S. M. **Imaging spectrometry: basic principles and prospective applications**. Kluwer Academic Publishers: Dordrecht, 2001.

DIERSSEN, H. M.; ZIMMERMAN, R. C.; LEATHERS, R. A.; DOWNES, T. V.; DAVIS, C. O. Ocean color remote sensing of seagrass and bathymetry in the Bahamas Banks by high-resolution airborne imagery. **Limnol. Oceanogr**., v. 48, n. 1 part 2, p. 444-455, 2003.

DOGAN, O. K.; AKYUREK, Z.; BEKLIOGLU, M. Identification and mapping of submerged plants in a shallow lake using quickbird satellite data. **Journal of Environmental Management**, v. 90, p. 2138–2143, 2009.

ESTEVES, F. A. **Fundamentos de Limnologia**. 3° Edição. Rio de Janeiro, RJ: Interciência, 2011.

FALKOWSKI, M. J.; GESSLER, P. E.; MORGAN, P.; HUDAK, A. T.; SMITH, A. M. S. Characterizing and mapping forest fire fuels using ASTER imagery and gradient modeling. **Forest Ecology and Management**, v. 217, p. 129–146, 2005.

FERREIRA, M. S.; GALO, M. L. B. T.; ROTTA, L. H. S.; ARAÚJO, R. R.; IMAI, N. N.; SAMIZAVA, T. M. Um estudo da distribuição espacial de pigmentos totais na planície de inundação do Alto Rio Paraná a partir de imagens multiespectrais. **Anais do XIV Simpósio Brasileiro de Sensoriamento Remoto,** INPE, abril 2009, p. 5211-5218.

FITZGERALD, R. W.; LEES, B. G. Assessing the Classification Accuracy of Multisource Remote Sensing Data. **Remote sensing of environment**, v. 47, p. 362-368, 1994.

GIARDINO, C.; ANDIANI A, G.; BRESCIANI A, M.; LEE, Z.; GAGLIANO, S.; PEPE, M. BOMBER: a tool for estimating water quality and bottom properties from remote sensing images. **Computeres and Geosciences**, v. 45, p. 313-318, 2012.

GITELSON, A. A; DALL'OLMO, G.; MOSES, W.; RUNDQUIST, D. C.; BARROW, T.; FISHER, T. R.; GURLIN, D.; HOLZ, J. A simple semi-analytical model for remote estimation of chlorophyll-a in turbid waters: Validation. **Remote Sensing of Environment,** v. 112, p. 3582–3593, 2008

GOOVAERTS, P. **Geostatistics for Natural Resources Evaluation**. New York: Oxford University Press, 1997.

GSFC - Goddard Space Flight Center. NASA. Web site. Available: <http://landsat.gsfc.nasa.gov/?p=5779>. Access: November 12th, 2014.

GULLSTRÖM, M.; LUNDÉN, B.; BODIN, M.; KANGWE, J.; ÖHMAN, M. C.; MTOLERA, M. S. P.; BJÖRK, M. Assessment of changes in the seagrass-dominated submerged vegetation of tropical Chwaka Bay (Zanzibar) using satellite remote sensing. **Estuarine, Coastal and Shelf Science**, v. 67, p. 399-408, 2006.

GUO, Y.; ZENG, F. Atmospheric correction comparison of spot-5 image based on model FLAASH and model QUAC. **International Archives of the Photogrammetry, Remote Sensing and Spatial Information Sciences**, v. XXXIX-B7, 2012.

HAVENS, K. E. Submerged aquatic vegetation correlations with depth and light attenuating materials in a shallow subtropical lake. **Hydrobiologia,** v. 493, p. 173-186, 2003.

HEBLINSKI J., SCHMIEDER K., HEEGE T., AGYEMANG T. K., SAYADYAN H., VARDANYAN L. High-resolution satellite remote sensing of littoral vegetation of Lake Sevan (Armenia) as a basis for monitoring and assessment. **Hydrobiologia**, v. 661, p. 97-111, 2011.

HESTIR, E. L.; KHANNA, S.; ANDREW, M. E.; SANTOS, M. J.; VIERS, J. H.; GREENBERG, J. A.; RAJAPAKSE, S. S.; USTIN, S. L. Identification of invasive vegetation using hyperspectral remote sensing in the California Delta ecosystem. **Remote Sensing of Environment**, v. 112, p. 4034–4047, 2008.

HOBI Labs - Hydro-Optics, Biology & Instrumentation Laboratories. HydroScat-6P – Spectral Backscattering Sensor & Fluorometer. **User's Manual**. HOBI Labs, 2010, 63p. Available: <http://www.hobilabs.com/cmsitems/attachments/3/HS6ManualRevJ-2010-8a.pdf>. Access: 11/01/2013.

IRONS, J. R.; DWYER, J. L.; BARSI, J. A. The next Landsat satellite: The Landsat Data Continuity Mission. **Remote Sensing of Environment**, v. 122, p. 11–21, 2012.

KARPOUZLI, E.; MALTHUS, T. The empirical line method for the atmospheric correction of IKONOS imagery. Int. J. **Remote Sensing**, v. 24, n. 5, p. 1143-1150. 2003.

KEMP, M.; BARTLESON, R.; MURRAY, L. Epiphyte Contributions to Light Attenuation at the Leaf Surface. In: **Chesapeake Bay Submerged Aquatic Vegetation Water Quality and Habitat-Based Requirements and Restoration Targets: A Second Technical Synthesis**. Chesapeake Bay Program, 2000.

KEMP, W. M.; BATIUK, R.; BARTLESON, R.; BERGSTROM, P.; CARTER, V.; GALLEGOS, C. L.; HUNLEY, W.; KARRH, L.; KOCH, E. W.; LANDWEHR, J.; MOORE, K. A.; MURRAY, L.; NAYLOR, M.; RYBICKI, N. B.; STEVENSON, J. C.; WILCOX, D. J. Habitat Requirements for Submerged Aquatic Vegetation in Chesapeake Bay: Water Quality, Light Regime, and Physical-Chemical Factors. **Estuaries**, v. 27, n. 3, p. 363–377, 2004.

KIRK, J. T. O. **Light and photosynthesis in aquatic ecosystems**. 3rd ed. New York: Cambridge University Press, 2011.

LANDIM, P. M. B. **Análise estatística de dados geológicos.** São Paulo: Ed. Unesp, 1998.

LANDIS J. R.; KOCH G. G. The measurement of observer agreement for categorical data**. Biometrics**, v. 33, p. 159-174, 1977.

LEE, Z. P.; CARDER, K. L. Effect of spectral band numbers on the retrieval of water column and bottom properties from ocean color data. **Applied Optics**, v. 41, n. 12, 2002.

LEE, Z. P.; CARDER, K. L.; CHEN, R. F.; PEACOCK, T. G. Properties of the water column and bottom derived from AVIRIS data. **Journal of geophysical research**, v. 106, n. c6, p. 11.639-11.651, 2001.

LEE, Z. P.; CARDER, K. L.; HAWES, S. K.; STEWARD, R. G.; PEACOCK, T. G.; DAVIS, C. O. Model for the interpretation of hyperspectral remote-sensing reflectance. **Applied Optics**, v. 33, n. 24, 1994.

LEE, Z. P.; CARDER, K. L.; MOBLEY, C. D.; STEWARD, R. G.; PATCH, J. S. Hyperspectral remote sensing for shallow waters: 1. A semianalytical model. **Applied Optics**, v. 37, n. 27, p. 6329-6338, 1998.

LEE, Z. P.; CARDER, K. L.; MOBLEY, C. D.; STEWARD, R. G.; PATCH, J. S. Hyperspectral remote sensing for shallow waters: 2. Deriving bottom depths and water properties by optimization. **Applied Optics**, v. 38, n. 18, p. 3831-3843, 1999.

LEE, Z. P.; CASEY, B.; ARNONE, R.; WEIDEMANN, A.; PARSONS, R.; MONTES, M. J.; GAO, B.; GOODE, W.; DAVIS, C. O.; DYE, J. Water and bottom properties of a coastal environment derived from Hyperion data measured from the EO-1 spacecraft platform. **Journal of Applied Remote Sensing**, v. 1, 011502, 2007.

LEE, Z. P.; DARECKI, M.; CARDER, K. L.; DAVIS C. O.; STRAMSKI, D.; RHEA, W. J. Diffuse attenuation coefficient of downwelling irradiance: An evaluation of remote sensing methods. **Journal of geophysical research**, v. 110, 2005.

MARCONDES, D. A. S.; MUSTAFÁ, A. L.; TANAKA, R. H. Estudos para manejo integrado de plantas aquáticas no reservatório de Jupiá. In: Thomaz, S. M.; Bini, L. M. (Editores). **Ecologia e manejo de macrófitas aquáticas**. Maringá: EDUEM, 2003.

MARITORENA, S.; MOREL, A.; GENTILI, B. Diffuse reflectance of oceanic shallow waters: Influence of water depth and bottom albedo**. Limnol. Oceanogr**., v. 39, n. 7, p. 1689–1703, 1994.

MARTINS, D.; CARDOSO, L.R.; MORI, E.S.; TANAKA R.H. Caracterização genética de acessos de egéria (Egeria spp.) coletados no estado de São Paulo utilizando RAPD. **Planta Daninha**, Viçosa-MG, v.21, p.1-6, 2003.

MISHRA, D. R.; NARUMALANI, S.; RUNDQUIST, D.; LAWSON, M. Charactering the vertical diffuse attenuation coefficient for downwelling irradiance in coastal waters: Implications for water penetration by high resolution satellite data. **ISPRS Journal of Photogrammetry & Remote sensing**, v. 60, p. 48–64, 2005.

MISHRA, D. R.; NARUMALANI, S.; RUNDQUIST, D.; LAWSON, M. High-Resolution Ocean Color Remote Sensing of Benthic Habitats: A Case Study at the Roatan Island, Honduras. **IEEE transactions on geoscience and remote sensing**, v. 43, n. 7, 2005b.

MISHRA, D.; NARUMALANI, S.; RUNDQUIST, D.; LAWSON, M. Benthic habitat mapping in tropical marine environments using Quickbird multispectral data. **Photogrammetric Engineering & Remote Sensing**, v. 72, n. 9, p. 1037–1048, 2006.

MOBLEY, C. D. **Light and Water: Radiative Transfer in Natural Waters**. San Diego: Academic Press, 1994.

MOSES, W. J.; GITELSON, A. A.; PERK, R. L.; GURLIN, D.; RUNDQUIST, D. C.; LEAVITT, B. C.; BARROW, T. M.; BRAKHAGE, P. Estimation of chlorophyll-a concentration in turbid productive waters using airborne hyperspectral data. **Water Research**, v. 46, p. 993-1004, 2012.

MOTOHKA, T.; NASAHARA, K. N.; OGUMA, H.; TSUCHIDA, S. Applicability of Green-Red Vegetation Index for Remote Sensing of Vegetation Phenology. **Remote Sensing**, v. 2, p. 2369-2387, 2010.

MUELLER, J. L. In-Water Radiometric Profile Measurements and Data Analysis Protocols. In: Mueller J.L.; Fargion G. S. and McClain C. R. (Editors), **Ocean Optics Protocols For Satellite Ocean Color Sensor Validation**. NASA, Goddard Space Flight Space Center, Greenbelt, Maryland 20771, Revision 4, Volume III, 2003.

MUMBY, P. J.; SKIRVING, W.; STRONG, A. E.; HARDY, J. T.; LEDREW, E. F.; HOCHBERG, E. J.; STUMPF, R. P.; DAVID, L. T. Remote sensing of coral reefs and their physical environment (Review). **Marine Pollution Bulletin**, v. 48, p. 219–228, 2004.

PAHLEVAN, N.; LEE, ZP.; WEI, J.; SCHAAF, C. B.; SCHOTT, J. R.; BERK, A. On-orbit radiometric characterization of OLI (Landsat-8) for applications in aquatic remote sensing. **Remote Sensing of Environment**, v. 154, p. 272–284, 2014.

PALANDRO, D. A.; ANDRÉFOUËT, S.; HU, C.; HALLOCK P.; MÜLLER-KARGER, F.; DUSTAN, P.; CALLAHAN, M. K.; KRANENBURG, C.; BEAVER, C. R. Quantification of two decades of shallow-water coral reef habitat decline in the Florida Keys National Marine Sanctuary using Landsat data (1984-2002). **Remote Sensing of Environment**, v. 112, p. 3388-3399, 2008.

PITELLI, L. R. C. M. Abordagens multivariadas no estudo da dinâmica de comunidades de macrófitas aquáticas. 2006, 59 p. **Tese** (Doutorado em Agronomia). Universidade Estadual Paulista, Botucatu - SP, 2006.

POMPÊO, M. L. M.; MOSCHINI-CARLOS, V. **Macrófitas aquáticas e perifíton: aspectos ecológicos e metodológicos**. São Carlos: Rima, 2003.

RIPLEY, H. T.; DOBBERFUHL, D.; HART, C. Mapping submerged aquatic vegetation with hyperspectral techniques. In: **OCEANS 2009**, MTS/IEEE Biloxi - Marine Technology for Our Future: Global and Local Challenges, IEEE, Biloxi - MS, USA, oct. 2009.

RODRIGUES, R. B.; THOMAZ, S. M. Photosynthetic and growth responses of *Egeria densa* to photosynthetic active radiation. **Aquatic Botany**, v. 92, p. 281-284, 2010.

RONGHUA MA, R.; DUAN, H.; GU, X.; ZHANG, S. Detecting aquatic vegetation changes in Taihu Lake, China using multi-temporal satellite imagery. **Sensors**, v. 8, p. 3988-4005, 2008.

ROTTA, L. H. S.; IMAI, N. N.; BATISTA, L. F. A.; BOSCHI, L. S.; GALO, M. L. B. T.; VELINI, E. D. Hydro-Acoustic Remote Sensing in Submerged Aquatic Macrophyte Mapping. **Planta Daninha**, Viçosa-MG, v. 30, n. 2, p. 229-239, 2012.

ROTTA, L. H. S.; IMAI, N. N.; BOSCHI, L. S. Imagem de alta resolução espacial na detecção de macrófitas submersas – estudo de caso. **Revista Brasileira de Cartografia**, v. 65, n. 2, no prelo 2013.

ROTTA, L. H. S.; IMAI, N. N.; FERREIRA, M. S.; SAMIZAVA, T. M.; ROCHA, P. C.; NOVO, E. M. L. M. Modelo de regressão na estimativa de sólidos em suspensão por meio de imagens multiespectrais TM-Landsat 5 e CCD-CBERS 2B - Estudo de caso: Planície de inundação do Alto Rio Paraná. **Anais do XIV Simpósio Brasileiro de Sensoriamento Remoto,** INPE, abril 2009, p. 5413-5420.

ROY, D. P. ET AL. Landsat-8: Science and product vision for terrestrial global change research. **Remote Sensing of Environment**, v. 145, p. 154–172, 2014.

RUDORFF, F. M.; KAMPEL, M.; GAETA, S. A.; POMPEU, M.; LORENZZETTI, J. A. Comparação de algoritmos empíricos na estimativa da concentração de clorofila-a na região costeira de Ubatuba, litoral norte de São Paulo. Anais XIII Simpósio Brasileiro de Sensoriamento Remoto, INPE, 2007, p. 4675-4682.

SABOL, B. M.; MELTON, R. E.; CHAMBERLAN, R.; DOERING, P.; HAUNERT, K.. Evaluation of a digital echo sounder system for detection of submersed aquatic vegetation. **Estuaries**, v. 25, p. 133-141, 2002.

SANTOS, M. J.; KHANNA, S.; HESTIR, E. L.; ANDREW, M. E.; RAJAPAKSE, S. S. GREENBERG, J. A.; ANDERSON, L. W.; USTIN, S. L. Use of Hyperspectral Remote Sensing to Evaluate Efficacy of Aquatic Plant Management. **Invasive Plant Science and Management**, v. 2, n. 3, p. 216-229, 2009.

SATHYENDRANATH, S., PLATT, T.; CAVERHILL, C. M.; WARNOCK, R. E.; LEWIS, M. R. Remote sensing of oceanic primary production: Computations using a spectral model. **Deep Sea Res**., v. 36, p. 431 – 453, 1989.

SCHWEIZER, D.; ARMSTRONG, R. A.; POSADA, J. Remote sensing characterization of benthic habitats and submerged vegetation biomass in Los Roques Archipelago National Park, Venezuela. **International Journal of Remote Sensing**, v. 26, n. 12, p. 2657–2667, 2005.

SILVEIRA, M. J.; THOMAZ, S. M.; MORMUL, R. P.; CAMACHO, F. P. Effects of Desiccation and Sediment Type on Early Regeneration of Plant Fragments of Three Species of Aquatic Macrophytes. **Internat. Rev. Hydrobiol**., v. 94, n. 2, p. 169–178, 2009.

SMITH G. M.; WILTON, E. J. The use of the empirical line method to calibrate remotely sensed data to reflectance. **Int. J. Remote Sensing**, v. 20, n. 13, p. 2653-2662, 1999.

SSRH/CRHi – Secretaria de Saneamento e Recursos Hídricos; Coordenadoria de Recursos Hídricos. Relatório de Situação dos Recursos Hídricos do Estado de São Paulo: Ano base 2009. 208 p. 2011.

STEHMAN. S. V. Selecting and Interpreting Measures of Thematic Classification Accuracy. **Remote sensing of environment**. v. 62, p. 77-89, 1997.

TAVECHIO, W. L. G.; THOMAZ, S. M. Effects of Light on the Growth and Photosynthesis of *Egeria najas* Planchon. **Brazilian Archives of Biology and Technology**, v.46, n. 2, p. 203-209, 2003.

THOMAZ, S. M. Fatores que afetam a distribuição e o desenvolvimento de macrófitas aquáticas em reservatórios: uma análise em diferentes escalas. In: **Ecologia de reservatórios: impactos potenciais, ações de manejo e sistemas em cascata**. 2ª Edição. Org.: NOGUEIRA, M. G.; HENRY, R.; JORCIN, A. São Carlos – SP: Editora RiMa, 2006.

THOMAZ, S. M.; BINI, L. M. Ecologia e manejo de macrófitas aquáticas em reservatórios. **Acta Limnologica Brasiliensia**, v. 10, n. 1, p. 103-116, 1998.

THOMAZ, S. M.; ESTEVES, F. A.; MURPHY, K. J.; DOS SANTOS, A. M.; CALIMAN, A.; GUARIENTO. R. D. Aquatic macrophytes in the tropics: ecology of populations and communities, impacts of invasions and use by man. **Tropical Biology and Conservation Management**, v. 4, p. 1-28, 2008.

TUNDISI, J. G.; TUNDISI, T. M. **Limnologia**. São Paulo: Oficina de Textos, 2008.

TWILLEY, R. R.; KEMPL, W. M.; STAVERL, K. W.; STEVENSONL, J. C.; BOYNTON, W. R. Nutrient enrichment of estuarine submersed vascular plant communities. 1. Algal growth and effects on production of plants and associated communities. **Marine Ecology – Progress Series**. v. 23, p. 179-191, 1985.

VAHTMÄE, E.; KUTSER, T. Classifying the Baltic Sea Shallow Water Habitats Using Image-Based and Spectral Library Methods. **Remote Sensing**, v. 5, p. 2451-2474, 2013.

VALLEY, R. D.; DRAKE, M. T. **Accuracy and precision of hydroacoustic estimates of aquatic vegetation and the repeatability of whole-lake surveys: field tests with a commercial echosounder**. St. Paul, MN, December 2005.

WACKERNAGEL, H. **Multivariate Geostatistics: An Introduction with Applications**. 3rd Ed. Third, completely revised edition. SPRINGER, 2003.

WATANABE, F. S. Y.; IMAI, N. N.; ALCÂNTARA, E. H.; ROTTA, L. H. S.; UTSUMI, A. G. Signal Classification of Submerged Aquatic Vegetation Based on the Hemispherical–Conical Reflectance Factor Spectrum Shape in the Yellow and Red Regions. **Remote Sensing**, v. 5, p. 1856-1874, 2013.

WEBSTER, R. AND OLIVER, M. A.: **Geostatistics for environmental scientists**. England: John Wiley & Sons, 2007.

WET Labs. Spectral Absorption and Attenuation meter (AC-S). **User's Guide**. WET Labs, 2009, 34p. Disponível em: http://www.wetlabs.com/. Acesso em 07/01/2013.

WETCH, P. S. Limnology. 2$^{nd}$ Ed. New York: Mc Graw Hill Book Co., 1952.

Wetzel, R. G.: **Limnology: Lake and River Ecosystems**. 3$^{rd}$ Ed., San Diego: Academic press, 1006 p., 2001.

WILLIAMS, D. J.; RYBICKI, N. B.; LOMBANA, A. V.; O'BRIEN, T. M.; GOMEZ, R. B. Preliminary investigation of submerged aquatic vegetation mapping using hyperspectral remote sensing. **Environmental Monitoring and Assessment**, v. 81, p. 383–392, 2003.